INFORMATION TO USERS

This manuscript has been reproduced from the microfilm master. UMI films the text directly from the original or copy submitted. Thus, some thesis and dissertation copies are in typewriter face, while others may be from any type of computer printer.

The quality of this reproduction is dependent upon the quality of the copy submitted. Broken or indistinct print, colored or poor quality illustrations and photographs, print bleedthrough, substandard margins, and improper alignment can adversely affect reproduction.

In the unlikely event that the author did not send UMI a complete manuscript and there are missing pages, these will be noted. Also, if unauthorized copyright material had to be removed, a note will indicate the deletion.

Oversize materials (e.g., maps, drawings, charts) are reproduced by sectioning the original, beginning at the upper left-hand corner and continuing from left to right in equal sections with small overlaps.

ProQuest Information and Learning
300 North Zeeb Road, Ann Arbor, MI 48106-1346 USA
800-521-0600

DISSERTATION

NONLINEAR MAGNETOSTATIC SPIN WAVES: INDUCED MODULATIONAL INSTABILITY AND ENVELOPE SOLITONS

Submitted by
Mark M. Scott
Department of Physics

In partial fulfillment of the requirements
For the Degree of Doctor of Philosophy
Colorado State University
Fort Collins, Colorado, USA
Summer 2002

ProQuest Information and Learning Company
300 North Zeeb Road
P.O. Box 1346
Ann Arbor, MI 48106-1346

COLORADO STATE UNIVERSITY

MAY 24, 2002

WE HEREBY RECOMMEND THAT THE DISSERTATION PREPARED UNDER OUR SUPERVISION BY MARK M. SCOTT ENTITLED NONLINEAR MAGNETOSTATIC SPIN WAVES: INDUCED MODULATIONAL INSTATBILITY AND ENVELOPE SOLITONS BE ACCEPTED AS FULFILLING IN PART REQUIREMENTS FOR THE DEGREE OF DOCTOR OF PHILOSOPHY.

Committee on Graduate Work

Stuart Field (Member)

Martin P. Gelfand (Member)

Carmen S. Menoni (Outside)

Carl E. Patton (Adviser)

David A. Krueger (Department Head)

ABSTRACT OF DISSERTATION

NONLINEAR MAGNETOSTATIC SPIN WAVES: INDUCED MODULATIONAL INSTABILITY AND ENVELOPE SOLITONS

An experimental investigation of nonlinear magnetostatic spin wave (MSW) excitations in low loss yttrium iron garnet (YIG) films has been made. In particular, the induced modulational instability of MSW excitations and the formation of spin wave envelope (SWE) solitons were observed. For this investigation, a frequency filtered active resonant ring (ARR) and an inductive magnetodynamic probe (IMP) system were developed. The experiments utilized GHz MSW excitations with wave numbers of approximately 100 rad/cm.

A frequency filtered ARR structure consists of a YIG film delay line with a specially tailored frequency characteristic connected in a feedback loop with a microwave amplifier. At high ring gains a comb of frequencies is self generated. The proper choice of filtering, combined with the nonlinear dispersive properties of the ring, allowed for the self generation of stable trains of SWE solitons. The primary nonlinear mechanism responsible for such soliton formation was the induced modulational instability of the self generated MSW excitations. In the experiments, this technique allowed for the observation of SWE bright and dark soliton trains for volume and surface MSW excitations, respectively. The amplitude, phase and frequency characteristics were used to confirm the soliton nature of the output pulses. This observation agrees with the predictions of the nonlinear Schrödinger (NLS) equation model.

The newly developed IMP system consists of a high resolution scanning inductive probe used in conjunction with a YIG film delay line. The IMP system allowed for a time and space resolved investigation of linear and nonlinear MSW excitations. In the experiments, SWE solitons formed due to the induced modulational instability of co-propagating MSW excitations were investigated. Bright and dark SWE solitons were observed for volume and surface MSW excitations, respectively. In addition, bright nonlinear pulses were observed for surface MSW excitations and dark nonlinear pulses were observed for volume MSW excitations. The NLS equation model forbids such formation. The amplitude, phase, and frequency characteristics for these nonlinear pulses were observed. Furthermore, a spatial recurrence phenomenon was observed for bright soliton trains formed from volume MSW excitations. Simulations based on the NLS equation model agreed well with the spatial recurrence experiments.

Mark M. Scott
Department of Physics
Colorado State University
Fort Collins, CO 80523
Summer 2002

ACKNOWLEDGEMENTS

I would like to thank my advisor, Professor Carl E. Patton, for his support and his assistance throughout the course of my graduate study at Colorado State University. My sincere appreciation is also due to Professor Boris A. Kalinikos of St. Petersburg Electrotechnical University in St. Petersburg, Russia. Both Professor Kalinikos and Professor Patton spent countless hours working with me on experiments, archival publications, and my thesis. In addition they spent many hours answering questions related to my graduate study. Their support and encouragement has been invaluable.

I would like to thank Greg Boll of Picoprobe® in Naples, Florida. His assistance in the fabrication of the probe used in the experiments is greatly appreciated. I would also like to thank Dr. Pavel Kabos, Richard Cox and Alex Nazarov for their participation in many insightful discussions related to this thesis. The samples used in the experiments were graciously provided by Dr. J. Douglas Adam of Northrop Grumman, Baltimore, Maryland and Professor Kalinikos.

Lastly, but certainly not least, I would like to thank my wife, Kathleen, and my immediate family. Their constant support throughout the course of my graduate studies and my life was invaluable and is gratefully acknowledged. I believe that my wife and family will take nearly as much joy in the completion of my graduate degree as I will.

This work was supported in part by the U. S. Army Research Office, Grant DAAG55-98-1-0430, and the National Science Foundation, Grant DMR-9801649.

TABLE OF CONTENTS

1 INTRODUCTION 1

1.1 Subject and Motivation 1
1.2 Investigation Overview 2

2 THEORY OF MAGNETOSTATIC SPIN WAVES 6

2.1 The Magnetization Vector 7
2.2 Spin Waves 10
2.3 Magnetostatic Spin Waves 17

3 THEORY OF ENVELOPE SOLITONS AND MODULATIONAL INSTABILITY 26

3.1 The Nonlinear Schrödinger Equation 27
3.2 Bright and Dark Envelope Solitons 30
3.3 Modulational Instability and Envelope Solitons 33
3.4 Group Velocity, Dispersion Coefficient, and Nonlinearity for Magnetostatic Spin Waves 39

4 MEASUREMENT SYSTEMS AND TECHNIQUES 43

4.1 The YIG Film Delay Line 44
4.2 Microwave Generation and Detection Instrumentation 52
4.3 The Frequency Fltered Active Resonant Ring System 56
4.4 The Inductive Magnetodynamic Probe System 60

5 LINEAR RESPONSE OF YIG FILM WAVEGUIDES: IMP SYSTEM MEASUREMENTS 68

5.1 The Linear Response of a Single MSW Excitation 70
5.2 Linear Standing Wave Response of MSW Excitations 73
5.3 Linear Mode Beating Response of MSW Excitations 78
5.4 Linear Loss and Dispersion of a 6.9 Micron Thick YIG Film Waveguide 83

6 THE SELF GENERATION OF SWE SOLITONS IN FREQUENCY FILTERED ACTIVE RESONANT RINGS 91

6.1 Dark Soliton Self Generation in a Frequency Filtered Active Resonant Ring 93
6.2 Bright Soliton Self Generation in a Frequency Filtered Active Resonant Ring 102

7 THE GENERATION OF SWE SOLITONS THROUGH NONLINEAR MODE BEATING 110

7.1 Magnetostatic Backward Volume Spin Wave Solitons Formed due to Nonlinear Mode Beating 112
7.2 Magnetostatic Surface Spin Wave Solitons Formed due to Nonlinear Mode Beating 130

8 CONCLUSION 142

8.1 Summaryof Results 142
8.2 Future Work 144

REFERENCES 146

CHAPTER 1

INTRODUCTION

1.1 Subject and Motivation

The nonlinear dynamics of waves are still rich in possibilities and unknowns. The recent increase in the volume of archival literature related to nonlinear wave dynamics is an indication of this richness. An experimental investigation of the nonlinear dynamics of magnetostatic spin wave (MSW) excitations propagated in single crystal yttrium iron garnet (YIG) films will be presented in this thesis. In particular, spin wave envelope (SWE) solitons and the induced modulational instability of MSW excitations have been investigated.

From the point of view of experimental science, MSW excitations in YIG films are well suited for this investigation. This is due largely to three factors. First, the strength of the nonlinearity for MSW excitations in YIG films is large compared to the losses and dispersion. The second factor is the low power thresholds of nonlinearity for these excitations. As a result of these factors, many power and distance dependent nonlinear phenomena are observable. Third, the type of nonlinearity and dispersion exhibited by MSW excitations in YIG films can be varied through experimentally accessible parameters. This allows for the observation of a wide variety of nonlinear wave

phenomena.

Aside from the advancement of nonlinear science, there are two main motivations for the investigation presented in this thesis. The first is related to the potential for YIG film device application [1]. The primary competition for YIG film devices is from surface acoustic wave (SAW) devices. However, YIG film devices have some advantages over SAW devices. At 9 GHz, SAW devices have losses on the order of 100 dB, whereas surface spin waves in YIG films may experience losses less than 3 dB. In addition, YIG film devices have the advantage of tunability through the variation of an externally applied magnetic field. These facts make MSW excitations in YIG films promising as a possible replacement for some SAW devices presently used in microwave systems.

The second motivation for this investigation is related to the fact that the *linear* characteristics of materials used in devices may be drastically effected by nonlinear phenomena. As a result, the use of linear material characteristics for device application may require knowledge of the nonlinear material characteristics and their thresholds. Furthermore, though this investigation deals with MSW excitations in YIG films, many of the results herein are applicable to waves in any nonlinear dispersive media. It is, therefore, clear that this investigation has ramifications for both linear and nonlinear devices which utilize nonlinear dispersive media.

1.2 Investigation Overview

A significant amount of work in the area of envelope solitons and the induced

modulational instability of waves has already been published [2–5, and Refs. therein]. Reference 2, by Remoissenet, gives a general theoretical and experimental review, as well as a historical development, of solitons and modulational instability. Reference 3, by Taylor, deals with the theory of and experiments on solitons and modulational instability for excitations in optical media. Reference 4, by Patton, deals specifically with solitons and modulational instability for excitations in magnetic media, specifically YIG films. These three references provide an overview of the background work which pertains to this thesis. From these references it can be determined that YIG films provide many unique possibilities for the investigation of envelope solitons and modulational instability which are inaccessible with other media. Some of these possibilities have already been investigated [4].

The discovery of spin wave envelope solitons by Kalinikos [5] in 1980 was a major advancement in the area of solitons and modulational instability for magnetic excitations. Another significant discovery by Kalinikos, addressed in Reference 4, is related to the self generation of spin wave envelope soliton trains due to the phenomena of induced modulational instability through the use of active resonant rings [6, 7]. The experiments in References 6 and 7 utilized a technique known as synchronized time gating. This time gating utilized modulation elements in the ring which were necessary to generate time stable trains of envelope solitons in the ring. Due to phase constraints introduced by the modulation elements in the ring, the self generation of single black solitons was not possible [8].

A part of this thesis is related to an improvement on such a self generation process through the use of a modified active resonant ring. This modification utilizes a frequency

filtering technique which requires no modulation elements to self generate time stable trains of bright and dark envelope solitons. It should be noted that, through the use of this frequency filtering technique, the self generation of single stable black solitons was realized for the first time in ferrite films.

The other significant work to be presented herein is related to the development of a high resolution inductive magnetodynamic probe (IMP) system. The IMP system is a marked improvement over the delay line transducers widely used in the investigation of nonlinear MSW excitations in YIG films [4 – 7]. The implementation of this system allowed for a time and space resolved investigation of linear and nonlinear MSW excitations. Aside from linear MSW excitations, an investigation of SWE solitons formed due to the induced modulational instability of co-propagating MSW excitations was performed. As in the self generation case mentioned above, previous experiments on the nonlinear mode beating of MSW excitations have shown the formation of SWE bright and dark solitons for volume and surface MSW excitations, respectively [9, 10]. The formation observed in these experiments agrees with the predictions of the single nonlinear Schrödinger (NLS) equation model. However, up to now, a detailed investigation of these solitons had not been performed.

Aside from the solitons observed in References 9 and 10, bright solitons were observed for surface MSW excitations and dark solitons were observed for volume MSW excitations. The single NLS equation model forbids such formation. The amplitude, phase, and frequency dependencies of these nonlinear pulse trains were observed together for the first time. Furthermore, a spatial recurrence phenomenon [2] was observed for bright soliton trains formed from volume MSW excitations. Modeling based on the

single NLS equation agrees well with the spatial recurrence results. The results of this investigation sheds some light on the physics of coupled waves, the formation processes at work in soliton self generation, and the nonlinear mode beating experiments of References 9 and 10.

Chapters 2 and 3 will present the linear and nonlinear theories which pertain to the results presented in this thesis. In Chapter 2 an emphasis will be given to the dispersion relations which describe MSW excitations in YIG films. In Chapter 3 an emphasis will be given to the NLS equation model of envelope solitons and modulational instability. At the end of Chapter 3, the parameters of the NLS equation will be evaluated from the relations for MSW excitations obtained in Chapter 2. Chapter 4 will detail the experimental setups and techniques implemented in this thesis. Chapter 5 will focus on the linear behavior of MSW excitations in YIG film waveguides as measured by the IMP system. These chapters will provide the basis for the results presented in Chapters 6 and 7. Chapter 6 will give the results obtained for SWE soliton self generation in active resonant rings with frequency filtering. Chapter 7 will present the investigation of solitons formed by the induced modulational instability of co-propagating MSW excitations. Where relevant, the experimental results will be compared with the predictions of the single NLS equation model. Chapter 8 will give a summary of, and a conclusion to, this thesis and present ideas on possible future work.

CHAPTER 2

THEORY OF MAGNETOSTATIC SPIN WAVES

The goal of this chapter is to make clear the origin, and develop the mathematical description, of magnetostatic spin wave (MSW) excitations. Specifically, the dispersion relations for two specific types of MSW excitations which propagate in tangentially magnetized ferrite films will be obtained in the absence of anisotropy and quantum mechanical exchange. The development in this chapter relies heavily on the text by Stancil [11].

Section 2.1 will describe the dynamics of a single magnetization vector in an unbounded magnetic sample. In particular, the precession of the magnetization and the ferromagnetic resonance (FMR) response will be addressed. Section 2.2 will introduce spin waves in an unbounded magnetic sample which consists of a collection of coupled magnetization vectors. In addition, the dispersion relation for these waves will be given and explained. Some comments on losses will conclude this section. Section 2.3 will discuss two specific types of MSW excitations in tangentially magnetized ferrite films. The dispersion relations for these excitations will be considered in detail.

2.1 The Magnetization Vector

The magnetization vector and its dynamics are key to the origin of spin waves and thus magnetostatic spin waves. The magnetization vector can be described macroscopically using the magnetic moment and magnetic spin of a collection of atoms which make up an unbounded magnetic material. The magnetic moment of an atom and the associated angular momentum turn out to be closely related to the magnetization vector. Therefore, an explanation of the relationship between the magnetic moment, the angular momentum, and the magnetization is necessary.

Consider a small volume element ΔV of an unbounded magnetic material which is composed of magnetic atoms. The total angular momentum for these atoms is the vector sum of the orbital and spin angular momenta. For many magnetic materials, including YIG, the total angular momentum is dominated by the spin angular momentum [11]. The magnetic moment $\boldsymbol{\mu}$ of each atom in the material is directly related to the associated spin angular momentum $\mathbf{S}$ by the relation

$$\boldsymbol{\mu} = -|\gamma|\mathbf{S}. \tag{2.1}$$

In Equation (2.1), γ is the gyromagnetic ratio for an electron. The value of γ, which is the ratio of the magnetic moment and the spin angular momentum, is well known and given by $\gamma = e/mc = -1.76\times10^{7}$ rad/s·Oe in Gaussian units [11]. The magnetic moment given by Equation (2.1) is directly related to the magnetization vector by the relation $\mathbf{M} = (1/\Delta V)\sum_{\Delta V}\boldsymbol{\mu}$.

The precessional dynamics of a magnetic moment and, therefore, the magnetization

vector will now be addressed. Spin waves, which will be presented in the next section, are a direct consequence of the precession of a collection of coupled moments. For now, only the precession of a single moment in an unbounded magnetic sample will be considered. In order to illuminate the precession of the magnetization vector, consider the schematic pictured in Figure 2.1. Figure 2.1 shows the magnetization vector **M** in the presence of a static magnetic field **H**. In the absence of any perturbations, **M** will line up with **H**. However, if **M** is perturbed from **H**, a torque $\boldsymbol{\tau}$ will be exerted on the magnetization. The torque on each magnetic moment is given by

$$\boldsymbol{\tau} = \boldsymbol{\mu} \times \mathbf{H} . \tag{2.2}$$

Since this torque is simultaneously equal to the time rate of change of the angular momentum associated with the magnetic moment $\boldsymbol{\tau} = \partial \mathbf{S}/\partial t$ one may write $\partial \boldsymbol{\mu}/\partial t = -|\gamma| \boldsymbol{\mu} \times \mathbf{H}$. The connection between **M** and $\boldsymbol{\mu}$ allows one to write,

$$\frac{\partial \mathbf{M}}{\partial t} = -|\gamma| \mathbf{M} \times \mathbf{H} . \tag{2.3}$$

Equation (2.3) is the equation of motion of the magnetization **M**. It is clear from Equation (2.3) that the torque is perpendicular to **M** and, as a result, $\boldsymbol{\tau}$ causes the precessional motion of **M** shown schematically in Figure 2.1. Note that the precessional motion of the magnetization is counter clockwise around the magnetic field when viewed from the top.

In Figure 2.1 the magnetization **M** has been decomposed into its static and dynamic components $\mathbf{M}_0$ and **m**, respectively. It will be useful in Chapter 3 to note that the magnitude of the static component of the magnetization may be written as $M_0 = \sqrt{M^2 - m^2}$. Furthermore, for small values of m, M_0 may be expanded in series as

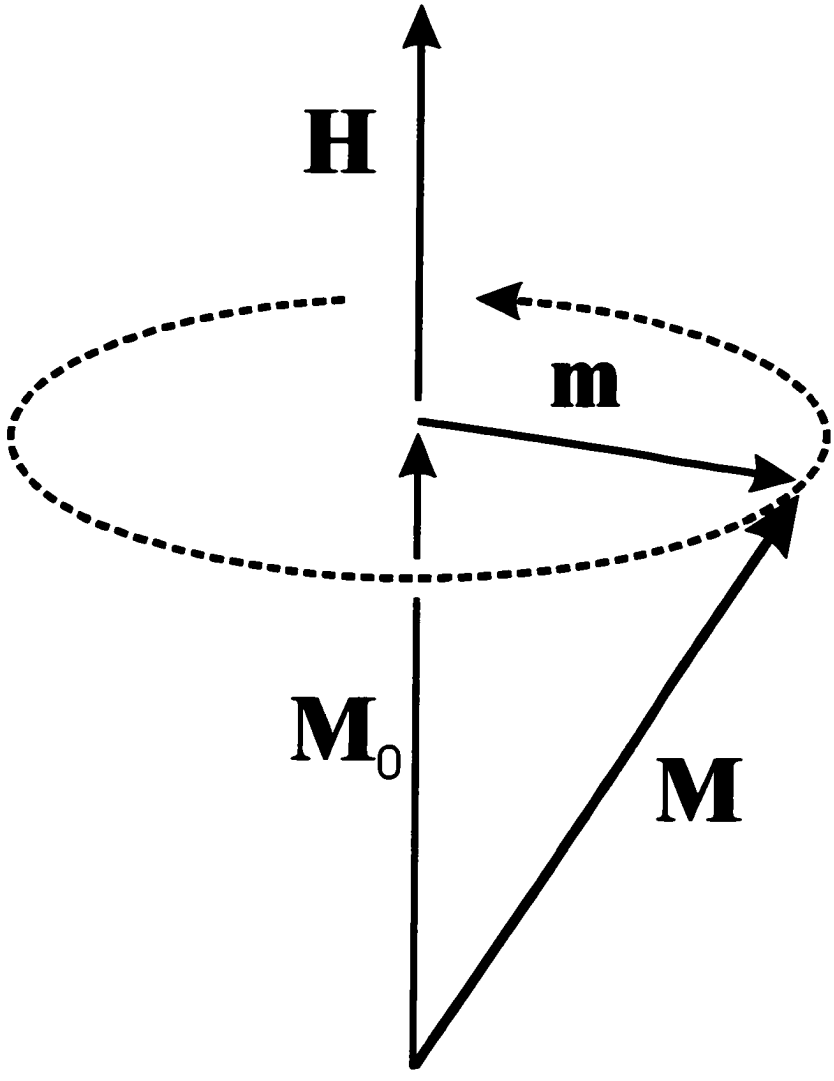

Figure 2.1. Schematic representation of the precession of a magnetization vector in a uniform static magnetic field. The magnetization and magnetic field vectors are illustrated by the arrows labeled **M** and **H**, respectively. The magnetization vector has been decomposed into its static and dynamic components. The counter clockwise circle maps the tip of the magnetization vector as it precesses about the magnetic field.

$$M_0 = M\left(1 - \frac{m^2}{2M^2} + \ldots\right) = M\left(1 - |u|^2 + \ldots\right). \tag{2.4}$$

Therefore, when the value of $|u|^2$ is small $M_0 \to M$, but for larger values of $|u|^2$ this approximation becomes invalid. The parameter $|u|^2$ will be used in some of the results to be presented later. It should be noted that Equation (2.4) assumes a circular precession of the magnetization. While experimentally this may not be true, the precession may always be modeled as circular by assuming some m_{eff} in Equation (2.4). Furthermore, the assumption of circular or elliptical precession only influences the connection between m_{eff} and u. This connection will not be addressed in this thesis.

One of the direct consequences of Equation (2.3) is ferromagnetic resonance. If one assumes a harmonic time dependence of **M** and solves the equation of motion in the linear signal response limit one finds

$$\omega_H = |\gamma| H . \tag{2.5}$$

This is the resonant precessional frequency of the magnetization vector in the presence of **H**. Remember that this is the resonance frequency for a single magnetization vector in an unbounded magnetic sample where there are no static or dynamic demagnetization effects. With the above dynamics of a single magnetization vector outlined, it is possible to introduce spin waves.

2.2 Spin Waves

Thus far, only the uniform precession of a single magnetization vector in an

unbounded magnetic sample has been considered. However, one may also consider the existence of a collection of magnetization vectors in an unbounded magnetic solid. Such a consideration creates the possibility for collective excitations characterized by some wavenumber $k = 2\pi/\lambda$, where λ is the wavelength of the excitation. Uniform precession may be characterized by $k \to 0$. This means that all of the magnetization vectors precess nearly in phase and $\lambda \to \infty$.

A spin wave with $k \neq 0$ occurs when adjacent moments do not precess in phase. A schematic representation of such an excitation is shown in Figure 2.2 for two limiting cases. The schematics in (a) and (b) are related to spin waves with their propagation directions **k** perpendicular and parallel to the magnetic field **H**, respectively. The schematics in (a-i) and (b-i) show perspective views of the respective spin wave. The schematics in (a-ii) and (a-iii) show a pair of the spins in (a-i) from the top. The schematic in (b-ii) shows a pair of the spins in (b-i) from the front.

The reason that both circular and elliptical precession cones are shown in Figure 2.2 is related to volume dipolar energies. In the case of (a), where the wave propagation direction is perpendicular to the magnetic field, volume dipolar magnetic fields are generated. The existence of volume dipole fields gives rise to two effects. First, the precession cone of the spin wave is modified from circular to elliptical. This elliptical precession cone is shown schematically in (a-iii). Circular precession is shown in (a-ii) for the case when the dipolar energies are neglected. The second effect is related to the frequency of the spin wave excitation. For the case of propagation perpendicular to the magnetic field, shown in (a), the elliptical precession would occur at a lower frequency than the circular precession. The ellipticity effectively "relaxes" the frequency of the

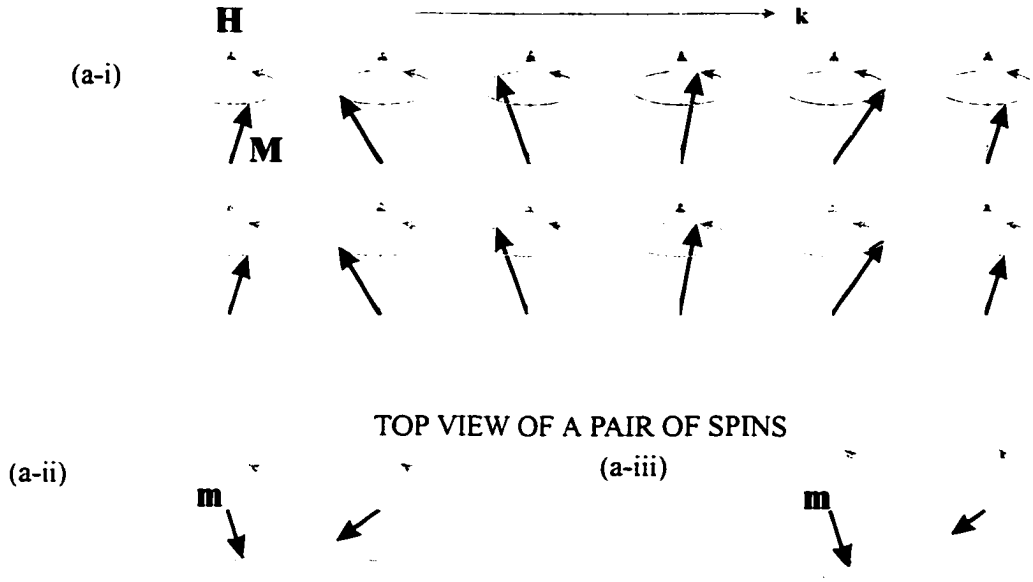

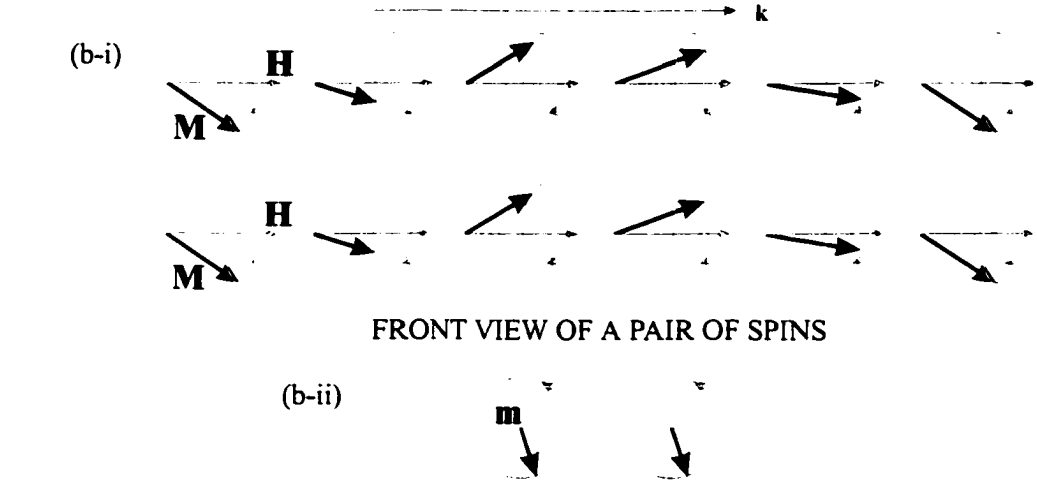

Figure 2.2. Schematic representation of two spin waves. The schematics in (a) and (b) show spin waves which propagate perpendicular and parallel to the external field, respectively. The wave propagation direction is indicated by the arrow labeled **k**. The schematics in (a-i) and (b-i) show perspective views of the respective spin waves. The schematics in (a-ii) and (a-iii) show a pair of the spins in (a-i) from the top. The schematic in (b-ii) shows a pair of the spins in (b-i) from the front.

spin wave precession, thereby lowering its frequency. In the case of (b), the propagation is parallel to the magnetic field and the generation of volume dipole fields is minimal. In this case, circular precession is shown in (b-ii).

The dispersion relations which describe the above waves are obtained by solving Equation (2.3) in the absence of exchange and anisotropy for the dynamic response of the magnetization. The dispersion relation which results from this formalism is given by

$$\omega_k = |\gamma|\sqrt{H_0^2 + H_0 4\pi M_S \sin^2\theta_k} = \sqrt{\omega_H^2 + \omega_H \omega_M \sin^2\theta_k}\,. \qquad (2.6)$$

In Equation (2.6) θ_k defines the angle between the propagation direction of the spin wave and the static magnetic field. A zero and ninety degree angle denotes propagation parallel and perpendicular to the static magnetic field, respectively. Note that in Equation (2.6) the saturation magnetic induction $4\pi M_S$ appears rather than the magnetization M. This is a consequence of the use of Gaussian units for a magnetic sample brought to saturation. This dispersion relation describes the spin waves where ellipticity is taken into account. It can be shown that, if $\omega_M \ll \omega_H$, an expansion of Equation (2.6) yields

$$\omega_k = \omega_H + \frac{\omega_M}{2}\sin^2\theta_k + \ldots. \qquad (2.7)$$

In the limit $\omega_M \ll \omega_H$, the precession of the magnetization is essentially circular [12]. Therefore, Equation (2.7) is the dispersion relation which describes the spin waves where ellipticity is ignored. Equations (2.6) and (2.7) show the spin wave behavior is a function of the angle θ_k. Note that Equations (2.6) and (2.7) were obtained in the absence of exchange and anisotropy for an unbounded magnetic sample. The spin wave dispersion where exchange and anisotropy are taken into account is considered by Gurevich [13].

It is of interest to note that, for propagation parallel to the magnetic field where

$\theta_k = 0$, both Equations (2.6) and (2.7) are equivalent to the ferromagnetic resonance frequency ω_H given by Equation (2.5). If, however, $\theta_k = 90°$, Equation (2.6) yields

$$\omega_k \to \omega_B = \sqrt{\omega_H (\omega_H + \omega_M)}, \tag{2.8}$$

and Equation (2.7) yields

$$\omega_k \to \omega_S = \omega_H + \frac{\omega_M}{2} + \ldots . \tag{2.9}$$

Equations (2.5), (2.8), and (2.9) represent important limits for spin wave excitations in the development which follows. These limits are plotted in Figure 2.3 for the parameters H = 1350 Oe and $4\pi M_S = 1800\text{G}$. The vertical axis shows frequency in GHz while the horizontal axis shows wave number in rad/cm. The boundaries $\omega_H/2\pi$, $\omega_B/2\pi$ and $\omega_S/2\pi$ are shown in Figure 2.3. Figure 2.3 shows clearly that these boundaries occur in the range of microwave frequencies. The lower frequency limit of these spin waves occurs at the boundary $\omega_H/2\pi$. The upper boundary $\omega_S/2\pi$ occurs at a higher frequency than the boundary $\omega_B/2\pi$. This shows that, as explained earlier for spin waves which propagate perpendicular to the static magnetic field, elliptical precession occurs at a lower frequency than circular precession.

It will be shown in the next section that low wave number spin waves in a bounded magnetic sample with frequencies between $\omega_B/2\pi$ and $\omega_S/2\pi$ describe waves of a surface character. While, the spin waves bounded by $\omega_B/2\pi$ and $\omega_H/2\pi$ describe waves of a volume character. These surface and volume waves will be explained in more detail in the next section.

Thus far damping has been ignored. However, in real systems there are losses which

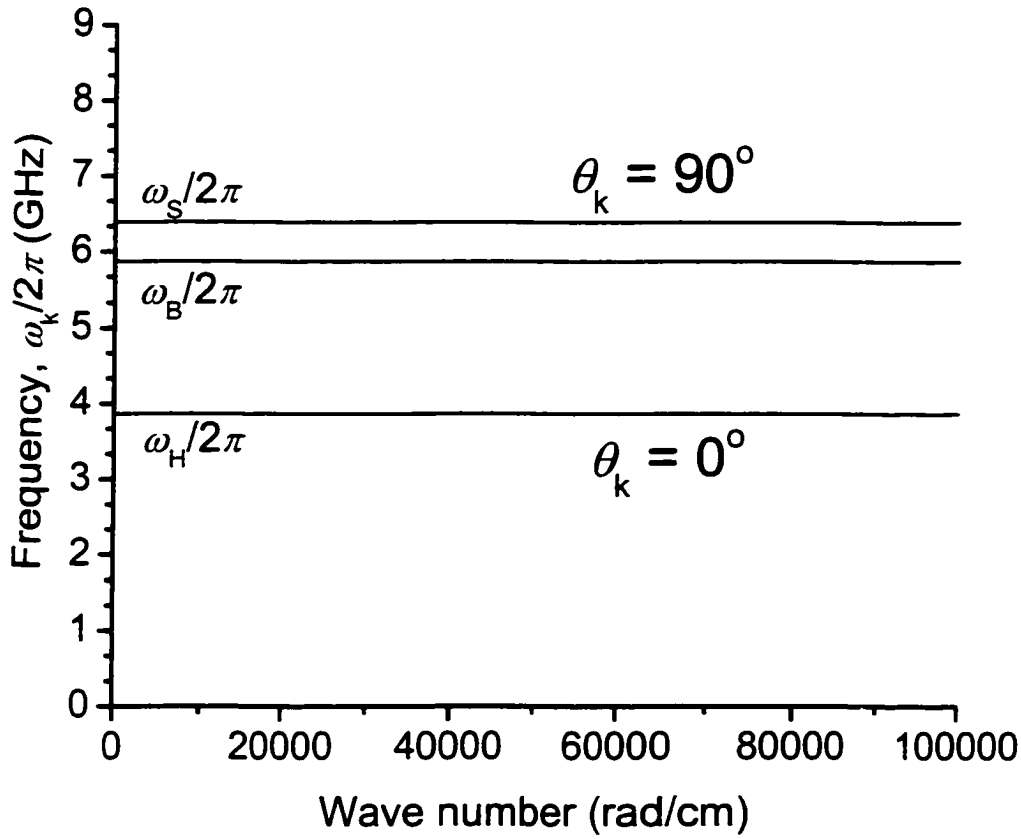

Figure 2.3. Limits of the spin wave dispersion given by Equations (2.5), (2.8) and (2.9) for the parameters H = 1350 Oe and $4\pi M_s$ = 1800 G. The top curve shows Equation (2.9). The middle curve is a plot of Equation (2.8). The lower curve shows Equation (2.5). The appropriate angles θ_k and frequencies $\omega/2\pi$ are labeled in the figure.

cause the precession of the magnetization to be damped. One way to model damping is to introduce a complex angular frequency. If one allows

$$\omega \rightarrow \omega + i\omega_r = \omega + \frac{i}{T_r}, \tag{2.10}$$

then the harmonic oscillation of the magnetization will be damped exponentially in time with a characteristic decay time T_r. Another way to model the damping of waves is to introduce a complex wave number. If one allows

$$k \rightarrow k + ik_r = k + \frac{i}{Z_r} \tag{2.10}$$

then the harmonic oscillation of the magnetization will be damped exponentially in space with a characteristic decay length Z_r. These relaxation times and distances are connected through the relation $Z_r = T_r |v_g|$, where v_g is the group velocity of the wave. In the literature, instead of decay lengths or times, typically the FMR linewidth is used. The damping time and length can be related to this FMR linewidth through the relation

$$\Delta H = \frac{2}{T_r |\gamma|} = \frac{2|v_g|}{Z_r |\gamma|}. \tag{2.11}$$

The FMR linewidth parameter is commonly used to measure the quality of a ferrite sample. For single crystal YIG films ΔH is typically 0.3 Oe at 5 GHz. This corresponds to a characteristic decay time on the order of hundreds of nanoseconds and, assuming v_g on the order of 10^6 cm/s, a characteristic decay length on the order of a few millimeters. Equation (2.11) holds strictly only for unbounded samples or samples with spherical symmetry. However, for the high frequency excitations in thin YIG films used in this thesis, Equation (2.11) would only be modified by a factor on the order of unity [11]. So,

for the sample loss measurement in Chapter 5, this linewidth parameter will be implemented.

2.3 Magnetostatic Spin Waves

Magnetostatic spin wave excitations in thin ferrite films are low wavenumber spin waves contained within the boundaries shown in Figure 2.3. In order to recover the dispersion relations which describe these excitations, Maxwell's boundary value problem must be solved. The solution of this problem shows that the waves which propagate in a bounded magnetic solid have a very rich dispersive character.

The full solution of Maxwell's boundary value problem shows that waves with different polarization couple differently to the magnetic system. The waves which couple weakly to the magnetic system are referred to as "fast" electromagnetic (EM) waves while those that couple strongly to the magnetic system are called "slow" spin waves. Figure 2.4 shows the boundaries of the spin wave manifold in Figure 2.3 for a smaller span of wave numbers where these so-called "fast" and "slow" waves are visible. From Figure 2.4 it is evident that, in the range of frequencies where "slow" spin waves exist, the "fast" EM waves occur only at very low wavenumbers. This fact allows one to make a significant simplification to Maxwell's boundary value problem. This so-called magnetostatic approximation allows one to ignore these "fast" EM waves in the limit of relatively large MSW excitation wave number.

The mathematical consequence of the magnetostatic approximation is that the curl of the magnetic field vanishes inside and outside the sample. Therefore, the magnetic field

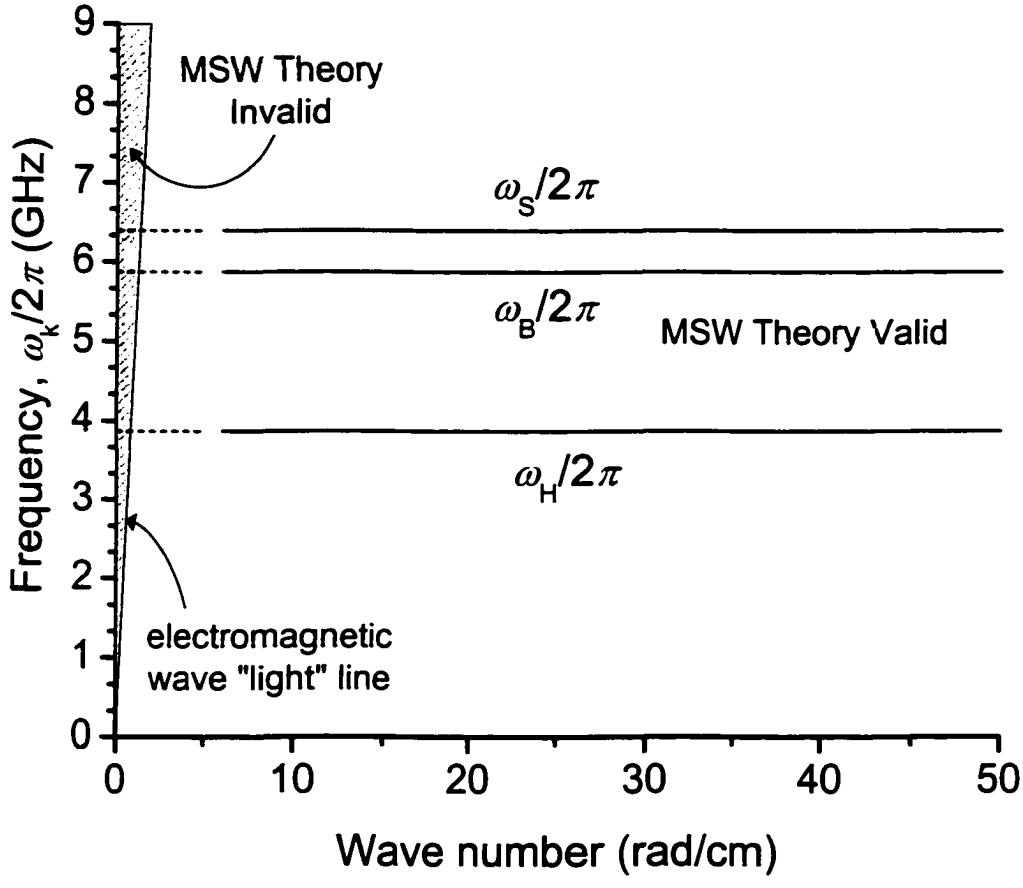

Figure 2.4. Diagram which shows the spin wave manifold of Figure 2.3 for a smaller span of wave numbers where the "fast" electromagnetic waves are visible. The shaded region of the graph shows where the magnetostatic approximation is invalid.

can be written in terms of a scalar magnetic potential $\mathbf{H} = -\nabla\Psi$. In addition, the magnetic field can be separated into space dependent and independent parts **h** and **H**, respectively. If the fields associated with excitation are ignored, **h** is associated only with spin waves. Therefore, $\mathbf{h} = -\nabla\Psi$. With this relation, along with the divergence equation $\nabla\cdot(\mathbf{h}+4\pi\mathbf{m}) = 0$, one may derive the partial differential equation for Ψ within the film. This relation is known as Walker's equation and is given by

$$(1+\chi)\left[\frac{\partial^2\Psi}{\partial x^2}+\frac{\partial^2\Psi}{\partial y^2}\right]+\frac{\partial^2\Psi}{\partial z^2} = 0. \qquad (2.12)$$

In Equation (2.12), z is the propagation direction and χ is the diagonal element of the susceptibility tensor which connects the microwave magnetic field to the dynamic component of the magnetization for a particular field-sample geometry. If one uses the susceptibility tensor for an unbounded magnetic sample in the absence of exchange and anisotropy given by $\chi = \omega_H\omega_M/(\omega_H^2-\omega^2)$ and solves Equation (2.12) for a plane wave with a purely real wave number, Equation (2.6) is recovered. The full susceptibility tensor is considered, among others, by Stancil [11].

Walker's equation is perhaps the most important equation for MSW theory. It is evident from Equation (2.12) that outside the film, where $\chi = 0$, Ψ is governed by Laplace's equation. From Walker's and Laplace's equations one may obtain the dispersion relations for magnetostatic spin waves by solving the electromagnetic boundary value problem for a plane wave in a particular field-sample geometry. The resultant dispersion relations for two particular cases will be addressed below.

The two particular cases of MSW excitations in tangentially magnetized ferrite films to be considered are shown in Figure 2.5. In Figure 2.5 the ferrite film is represented by

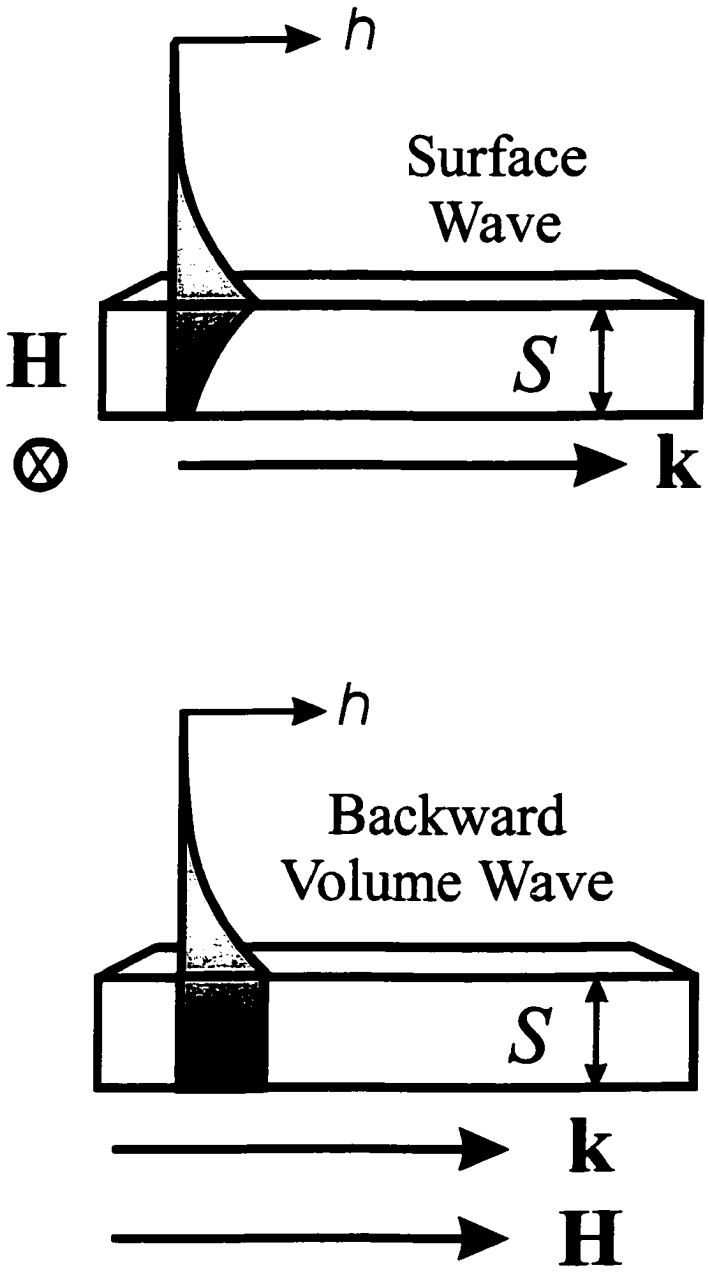

Figure 2.5. Schematic representation of two limiting MSW configurations. The diagrams in (a) and (b) correspond to the magnetostatic surface wave (MSSW) and magnetostatic backward volume wave (MSBVW) configurations, respectively. The directions of the external magnetic field and the wave propagation direction are represented by the arrows labeled **H** and **k**, respectively. The samples thickness is labeled *S*. The shaded shapes labeled *h* are schematic representations of the distribution of the magnitude of the microwave magnetic field inside and outside the sample.

the gray rectangle of thickness S and the distribution of the microwave magnetic field intensity h is shown by the shaded gray region. The existence of this field intensity outside the film is critical to the detection of MSW excitations to be considered in Chapter 4. Figure 2.5 (a) shows the magnetostatic surface wave (MSSW) configuration. In this case the film is magnetized in plane and the wave propagates in the film plane perpendicular to the external field. The term "surface" comes from the fact that the magnitude of the dynamic magnetic field is largest at one surface, as shown schematically in Figure 2.5 (a).

Figure 2.5 (b) shows the magnetostatic backward volume wave (MSBVW) configuration. In this case, the film is magnetized in plane and the wave propagates parallel to the external field. The term "volume" is derived from the fact that the magnitude of the dynamic magnetic field is distributed harmonically across the film thickness.

The magnetostatic surface spin wave dispersion relation is given by

$$\omega_k = \sqrt{\omega_B^2 + \frac{\omega_M^2}{4}\left(1 - e^{-2kS}\right)}. \tag{2.13}$$

Equation (2.13) was first elaborated by Damon and Eshbach in 1961 [14]. The upper curve of Figure 2.6 is a plot of Equation (2.13) for the parameters $H = 1350\,\mathrm{Oe}$, $4\pi M_S = 1800\,\mathrm{G}$, and $S = 7\,\mu\mathrm{m}$. A peculiarity of MSSW excitations is their essentially unidirectional character. In reality surface waves are bi-directional, however the excitation efficiency of waves which travel in the $-k$ direction is relatively poor. Furthermore, in the experiments, these $-k$ waves travel on the film surface in contact with a dielectric substrate and thus experience higher losses. It is of interest to note that for

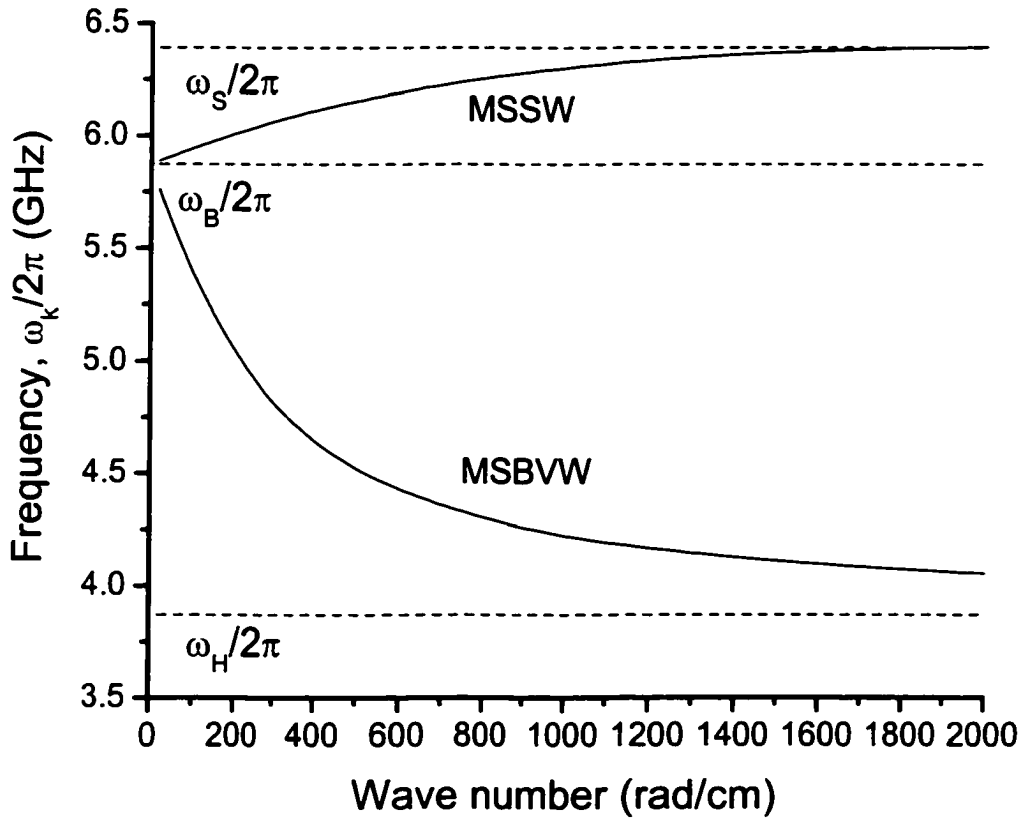

Figure 2.6. Dispersion diagram of MSW excitation frequency vs. wave number for two in plane magnetized thin film configurations. The upper and lower curves represent the dispersion relation for MSSW and MSBVW excitations, respectively. The MSSW and MSBVW dispersions were obtained from Equations (2.15) and (2.13) for the same parameters as Figure 2.3 and a film thickness S = 7 μm. The horizontal dashed lines represent the same band limits shown in Figures 2.3 and 2.4.

$k \to 0$ Equation (2.13) reduces to the resonance condition of Equation (2.8), that is $\omega_k = \omega_B$. Furthermore, for $k \to \infty$ this relation reduces to the resonance condition of Equation (2.9), that is $\omega_k = \omega_S$. These limits are evident in Figure 2.6.

The magnetostatic backward volume spin wave dispersion is obtained from Walker's equation in the form of the transcendental relation

$$\tan\left[\frac{kS}{2\sqrt{-(1+\chi)}} - \frac{(n-1)\pi}{2}\right] = \sqrt{-(1+\chi)}, \qquad n = 1,2,3.... \tag{2.14}$$

Equation (2.14) was first elaborated by Damon and Eshbach in 1961 [14]. Recall that χ, which was given above under Equation (2.12), is a function of frequency. Note that the MSBVW dispersion relation is multi-mode in character. Due to the efficiency of their excitation and their low group velocity, the higher order MSBVW modes have no significant influence in the experiments to be considered in this thesis and are thus ignored. A simplifying relation for the lowest order mode was derived by Kalinikos [see, e.g., Ref. 11] and is given by

$$\omega_k = \sqrt{\omega_H^2 + \omega_H \omega_M \left(\frac{1 - e^{-kS}}{kS}\right)}. \tag{2.15}$$

This relation is valid for $kS \ll 1$. This relation holds for the experiments to be considered later and is thus employed for theoretical comparisons. The lower curve of Figure 2.6 is a plot of Equation (2.14) for the same parameters as Equation (2.13). It is of interest to note that for $k \to 0$ this relation reduces to the resonance condition of Equation (2.8), that is $\omega_k = \omega_B$. Furthermore, for $k \to \infty$ this relation reduces to the resonance condition of Equation (2.5), that is $\omega_k = \omega_H$. These limits are indicated in Figure 2.6.

Apart from the mathematical analysis given above, one can understand the behavior of MSW excitations from more intuitive physical considerations based on volume dipolar and surface demagnetization energies. These considerations will allow one to explain qualitatively the shapes of the dispersion characteristics shown in Figure 2.6. A detailed discussion of these waves is given by Hurben [15].

First, consider the shape of the MSSW dispersion. Note from Figure 2.6 that the dispersion for MSSW excitations starts at ω_B at low wave number and rises to ω_S as the wave number increases. Recall that excitations at ω_B have an elliptical precession, while those at ω_S have a nearly circular precession in spite of the fact that ω_M is on the same order as ω_H. Recall further from the discussion of Figure 2.2 that spins which propagate perpendicular to the magnetic field with $k = 0$ precess in phase and there are minimal volume dipolar energies. However, due to the existence of a film surface, there are dynamic surface demagnetization effects for these $k = 0$ excitations. These demagnetization effects cause the precession cone to be modified to an elliptical shape. Now consider a $k \neq 0$ excitation. The spins for this excitation precess with a phase shift between them. As the wave number increases, so too does the phase shift between adjacent spins. As a consequence, the volume dipolar effects increase with an increase in wave number. These volume dipolar effects induce an ellipticity in the precession which is counter to the ellipticity induced by the film surface. Therefore, as the wave number increases the precession becomes more circular and the energy of these waves increases. This is how one receives a wave which propagates perpendicular to the field with a circular precession even when ω_M is on the same order as ω_H. This increase in frequency, and therefore energy, with wave number is evident in Figure 2.6.

Consider now the shape of the MSBVW dispersion. Note first from Figure 2.6 that the dispersion for MSBVW excitations starts at ω_B at low wavenumber and drops to ω_H as the wave number increases. Note further that excitations at ω_B have an elliptical precession, while those at ω_H have a circular precession. Recall further, from the discussion of Figure 2.2, that spins which propagate parallel to the magnetic field experience essentially no volume dipolar effects. There are, however, dynamic surface demagnetization effects due to the existence of the film surface. These demagnetization effects cause the precession cone of these $k = 0$ excitations to be modified to an elliptical shape. The existence of the surface is how one receives a wave which propagates parallel to the field with an elliptical precession. As the wave number increases, the wavelength decreases and the net surface dynamic demagnetization effect begins to average to zero. Therefore, as the wavenumber of these waves increases, the energy of these waves decreases as reflected in Figure 2.6.

With both a mathematical and intuitive description of MSW excitations, the nonlinear dynamics of these waves will be addressed. The dispersion relations for MSSW and MSBVW excitations will be critical in Chapter 3.

CHAPTER 3

THEORY OF ENVELOPE SOLITONS AND MODULATIONAL INSTABILITY

The so-called nonlinear Schrödinger (NLS) equation, obtained from a wave amplitude dependent dispersion relation, can be used to describe envelope solitons and modulational instability. In this chapter, the method of envelopes will be used to obtain the NLS equation and, from this equation, introduce envelope solitons and modulational instability. The development in Sections 3.1 – 3.3 relies heavily on the text by Remoissenet [2]. Section 3.4 will rely on the relations obtained in Chapter 2.

In Section 3.1, the method of envelopes will be used to obtain the NLS equation. In Section 3.2, the criteria for, and equations of, single bright and dark envelope solitons obtained from the NLS equation model will be developed. In Section 3.3, the concept of modulational instability and its connection to envelope solitons will be developed. Section 3.4 will conclude this chapter with an evaluation of the group velocity, dispersion, and nonlinear coefficients from the dispersion relations obtained in Chapter 2. These coefficients, which appear as parameters in the NLS equation, are critical to the analyses in this thesis.

3.1 The Nonlinear Schrödinger Equation

In this section, the method of envelopes will be applied first to a linear dispersion relation in order to obtain the linear Schrödinger equation. Next, through an extension of the formalism to an amplitude dependent dispersion relation, the NLS equation will be recovered.

The method of envelopes is essentially a Taylor series expansion of a dispersion relation ω_k about some carrier wavenumber k_0. Under certain assumptions this expansion can be generalized to an equation of motion for a wave packet envelope. The method of envelopes is valid for a wave packet which consists of a sinusoidal carrier of constant frequency ω_0 and wave number k_0 modulated by an envelope function u. It is assumed that u varies slowly in space and time. As a consequence of this slow variance, the waveform contains a large number of carrier wave crests and the amplitude distribution is concentrated in wave numbers close to the carrier wave number k_0. These assumptions constitute the so-called envelope approximation.

Consider the dispersion relation of the form

$$\omega_k = \omega(k). \tag{3.1}$$

An expansion of Equation (3.1) around the carrier wave number k_0 yields

$$\omega_k - \omega_0 = \left.\frac{\partial \omega_k}{\partial k}\right|_{k=k_0} \cdot (k-k_0) + \frac{1}{2}\left.\frac{\partial^2 \omega_k}{\partial k^2}\right|_{k=k_0} \cdot (k-k_0)^2 + \ldots. \tag{3.2}$$

In Equation (3.2), the group velocity v_g and dispersion coefficient D, given by $\partial\omega_k/\partial k = v_g$ and $\partial^2\omega_k/\partial k^2 = D$, are evaluated at $k = k_0$. Both v_g and D can be

obtained from the linear dispersion relations in Chapter 2. In terms of the new variables, $\Omega = \omega_k - \omega_0$ and $\mathrm{K} = k - k_0$, Equation (3.2) becomes

$$\Omega = v_g \mathrm{K} + \frac{1}{2} D \mathrm{K}^2 . \tag{3.3}$$

Equation (3.3) is the dispersion relation for the envelope of a wave. Under the envelope approximation, Ω and K are small and can be replaced by the operators $-i \cdot (\partial/\partial t)$ and $i \cdot (\partial/\partial z)$, respectively, where z and t are the slow space and time variables of the envelope function $u \propto \exp(i\Omega t - i\mathrm{K}z)$. Substitution of these operators in Equation (3.3) yields an expression, when allowed to operate on u, of the form

$$i\left(\frac{\partial u}{\partial t} + v_g \frac{\partial u}{\partial z}\right) - \frac{1}{2} D \frac{\partial^2 u}{\partial z^2} = 0 . \tag{3.4}$$

Equation (3.4) governs the evolution of the wave envelope. If i is replaced by $i\hbar$ and D is replaced by $\hbar^2/2m$, the resultant equation is formally similar to the linear Schrödinger equation for a quantum mechanical free particle. The time evolution of solutions to Equation (3.4) shows a dispersive spreading of the wave packet envelope. This is a consequence of the dispersion coefficient D which modifies the phase of each Fourier component of the wave packet during propagation.

In order to recover the NLS equation consider a dispersion relation, which is modified from the form of Equation (3.1) to depend on the square of the wave amplitude, of the form

$$\omega_k = \omega\left(k, |u|^2\right) . \tag{3.5}$$

The $|u|^2$ dependence in Equation (3.5) enters into the dispersion relations for MSW

excitations in Chapter 2 through the ω_M term. The details of this dependence will be given in section 3.4. If one proceeds as in the linear case and expands Equation (3.5) one obtains

$$\omega_k - \omega_0 = \left.\frac{\partial \omega_k}{\partial k}\right|_{k=k_0} \cdot (k-k_0) + \frac{1}{2}\left.\frac{\partial^2 \omega_k}{\partial k^2}\right|_{k=k_0} \cdot (k-k_0)^2 + \left.\frac{\partial \omega_k}{\partial |u|^2}\right|_{|u|^2=0,\, k=k_0} |u|^2 + \ldots. \quad (3.6)$$

This equation is formally similar to Equation (3.2) with the addition of a nonlinear term. Thus, when the nonlinear effects are taken into account, the linear Equation (3.3) is modified to a nonlinear relation for the wave envelope dispersion given by

$$\Omega = v_g \mathrm{K} + \frac{1}{2} D\mathrm{K}^2 + N|u|^2. \quad (3.7)$$

If one follows the same procedure as for the linear case, it is possible to obtain an equation of motion for the envelope of the wave in the standard form

$$i\left(\frac{\partial u}{\partial t} + v_g \frac{\partial u}{\partial z}\right) - \frac{1}{2} D \frac{\partial^2 u}{\partial z^2} + N|u|^2 u = 0. \quad (3.8)$$

Equation (3.8) is the NLS equation. The dispersion coefficient *D*, the group velocity v_g, and the nonlinear coefficient *N*, which appear in the NLS equation, can be obtained from an explicit dispersion relation. In Section 3.4 the dispersion relations for the MSW excitations considered in Chapter 2 will be used to obtain these parameters.

The phase shifts of the Fourier components of the wave packet introduced by the nonlinear term can, under certain conditions, cause wave packet compression. This compression may compensate for the dispersive spreading of the wave packet and yield envelope solitons which propagate without change of shape. The cubic nonlinearity term $N|u|^2 u$ in Equation (3.8) represents a four wave mixing process of the type

$$\begin{aligned} 2\omega(k_0) &= \omega(k_1) + \omega(k_2) \\ 2k_0 &= k_1 + k_2 \end{aligned} \quad . \tag{3.9}$$

In fact, it is important to note that the NLS equation can be rigorously derived from the conservation Equations (3.9) through a Hamiltonian formulation [16].

3.2 Bright and Dark Envelope Solitons

As mentioned in the previous section, the compensation of the dispersive and nonlinear terms in the NLS equation may yield envelope soliton solutions. Two types of envelope solitons, bright and dark, are admitted by the NLS equation. When the product of the dispersion and nonlinearity is less than zero, $ND < 0$, the formation of bright solitons is possible. This criterion, referred to as attractive nonlinearity, is satisfied for MSBVW excitations. When the product of the dispersion and nonlinearity is greater than zero, $ND > 0$, the formation of dark solitons is possible. This criterion, referred to as repulsive nonlinearity, is satisfied for MSSW excitations.

For the case of attractive nonlinearity the NLS equation admits solutions of the form

$$u(x,t) = u_{\max} \operatorname{sech}\left[u_{\max} \sqrt{\left|\frac{N}{D}\right|} (z - v_g t) \right]. \tag{3.10}$$

In 1972, Zakharov and Shabat showed that such a solution is a bright envelope soliton [17]. Moreover, they have shown that any initial localized disturbance will evolve into a soliton which, once formed, will propagate with permanent form. It is of interest to note that, as a consequence of the compensation between phase shifts from the nonlinear and dispersive terms, the phase change across the width of the pulse is approximately zero [18].

Figures 3.1 shows the signature amplitude vs. time profile for a bright envelope soliton at $z = 0$. The plot in Figure 3.1 is for the parameters $|N| = 8\times10^{9}$ rad/s, $|D| = 3.5\times10^{6}$ cm^2/rad·s, $|v_g| = 3\times10^{6}$ cm/s, and $u_{max} = 0.01$. These values are typical of MSBVW excitations with attractive nonlinearity. In the figure the shaded gray area indicates the region where the carrier signal exists. The amplitude profile shows the narrow and bright nature of the amplitude profile for a bright soliton. The phase vs. time profile would be approximately zero across the width of the bright soliton. The amplitude and phase vs. time profiles are useful in the identification of bright solitons in experiment.

For the case of repulsive nonlinearity, the NLS equation admits solutions of the form

$$u(x,t) = u_{max}\sqrt{1-m^2\mathrm{sech}^2\left[\sqrt{\left|\frac{N}{D}\right|}m\ \ u_{max}(z-v_g t)\right]}. \tag{3.11}$$

In Equation (3.11), m is a parameter which controls the depth of modulation given by $m^2 = \left(u_{max}^2 - u_{min}^2\right)/u_{max}^2$, where u_{max} and u_{min} are the maximum and minimum amplitude values of the envelope function u, respectively. The phase time function $\theta(x,t)$ for the above solution is given by

$$\theta(x,t) = \tan^{-1}\left\{\frac{m}{\sqrt{1-m^2}}\tanh\left[\sqrt{\left|\frac{N}{D}\right|}m\ \ u_{max}(z-v_g t)\right]\right\}. \tag{3.12}$$

A solution of the form given by Equations (3.11) and (3.12) was originally found by Zakharov and Shabat in 1973 [19]. They referred to this solution as a hole or dark soliton. The name comes from the fact that the solution corresponds to a dip, or hole, in the envelope function. For the case $m = 1$, the value of u_{min} is zero and Equation (3.11)

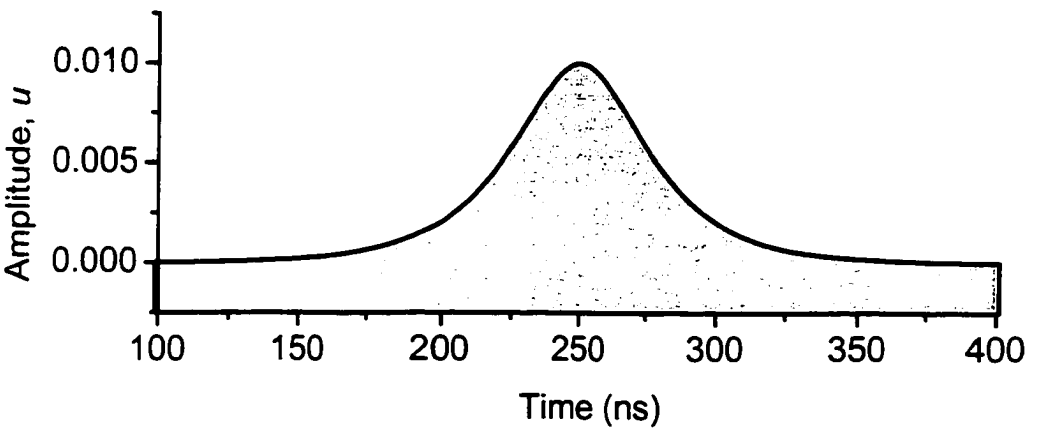

Figure 3.1. Plot of the amplitude vs. time of a bright envelope soliton. The graph shows the time dependence of a bright envelope soliton given by Equation (3.11) at a fixed distance.

becomes

$$u(x,t) = u_{\max} \tanh\left[\sqrt{\frac{N}{D}} u_{\max}(z - v_g t)\right]. \tag{3.13}$$

This solution represents a black soliton. In addition, it can be shown that Equation (3.13) has a phase jump of 180° at the center of the pulse.

Figure 3.2 shows the signature amplitude and phase time profiles for dark and black envelope solitons at $z = 0$. The plots in Figure 3.2 are for the parameters $|N| = 8\times10^9$ rad/s, $|D| = 3.5\times10^6$ cm^2/rad·s, $|v_g| = 3\times10^6$ cm/s, and $u_{\max} = 0.01$. These values are typical for MSSW excitations with repulsive nonlinearity. The amplitude and phase of a dark, or gray, soliton with $m = 0.9$ are shown in Figure 3.2 (a) and (c), respectively. The amplitude and phase of a black soliton with $m = 1$ are shown in Figure 3.2 (b) and (d), respectively. The shaded regions in (a) and (b) show where the carrier signal exists. As is evident from graphs (a) and (b), the dip in the amplitude profile for a black soliton goes to zero while for a gray soliton the dip goes to some nonzero value. Additionally, graphs (c) and (d) show that the phase jump across the pulse is 180° for the black soliton and is some non zero value less than 180° for the gray soliton. The amplitude and phase vs. time profiles for dark solitons are useful in their identification in experiment.

3.3 Modulational Instability and Envelope Solitons

The existence of soliton solutions to the NLS equation has been established. However, the development above is related to the formation of *single soliton pulses* as

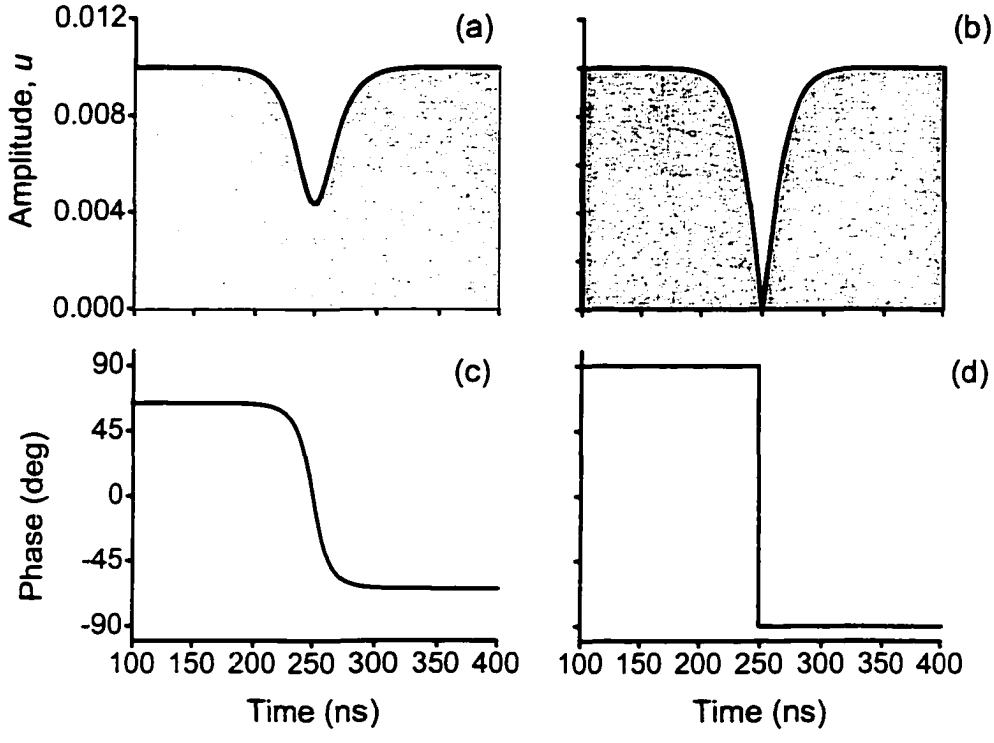

Figure 3.2. Plot of dark and black envelope soliton amplitude and phase vs. time profiles. Graphs (a) and (c) show the amplitude and phase vs. time profiles for a gray envelope soliton given by Equations (3.11) and (3.12), respectively, for $m = 0.9$ at a fixed distance. Graph (b) shows the time dependence of a black envelope soliton envelope given by Equation (3.13) at a fixed distance. Graph (d) shows the 180° phase jump indicative of a black envelope soliton.

predicted from the NLS equation model. These pulses are formed in experiment from input pulses [2 – 4, 20, and Refs. therein]. In this section, the modulational instability of a uniform wave train solution of the NLS equation will be introduced. Furthermore, how this modulational instability can lead to the formation of envelope soliton pulse *trains* will be developed.

In general, it is possible to show that the NLS equation in the frame moving at the group velocity v_g admits a plane wave solution of the form $u = u(z,t)\exp(i\theta(z,t))$ which is unstable to small sinusoidal perturbations of the wave envelope [2]. This modulational instability of the wave envelope is observed for $ND < 0$ [2]. In the case of input pulses considered in Section 3.2, this attractive nonlinearity led to the formation of bright soliton pulses. In the case of a plane wave, this attractive nonlinearity can lead to the formation of an envelope soliton "pulse *train*". In this thesis, the term "pulse train" will be used to describe the shape of this strongly modulated wave envelope. Modulational instability is not observed for $ND > 0$. The modulation frequency where the instability growth rate is a maximum is given by

$$F_{\max} = \frac{|N|u_{\max}^2}{2\pi}. \tag{3.14}$$

For $N = 1\times10^{10}$ rad/s and $u_{\max}^2 = 0.01$, Equation (3.14) yields $F_{\max} \sim 10$ MHz. In the presence of wave damping, the modulation frequency has a lower limit [16]. In magnetic systems this minimum frequency is given by

$$F_{\min} = \left(\frac{1}{2\pi}\right)\frac{1}{T_r} \approx \left|\frac{\gamma}{2\pi}\right|\frac{\Delta H}{2}. \tag{3.15}$$

It will be shown in Chapter 5 that the losses for the films used in the experiments are ΔH

= 0.5 Oe. For this value of ΔH, Equation (3.15) yields $F_{min} \sim 1\,\mathrm{MHz}$.

The modulational instability described above occurs spontaneously due to intrinsic fluctuations. In this case, the instability process is referred to as self phase or spontaneous modulational instability and is described by the single NLS equation model. Modulational instability may also occur through the application of an external signal. In this case, it is referred to as cross phase or induced modulational instability.

This thesis is concerned with the induced modulational instability of waves. An analysis of two coupled NLS equations shows that the cross interaction which occurs for induced modulational instability is twice as effective as for self modulational instability. In addition, the instability condition for induced modulational instability is very rich when compared to the self modulational instability case [see, e.g., 21]. In fact induced modulational instability is observed for both attractive and repulsive nonlinear systems. Moreover, the modulation frequency were the instability growth rate is a maximum for a single wave given by Equation (3.14) is increased in the presence of a second modulationally unstable wave. Furthermore, waves which are modulationally stable by themselves are often unstable in the presence of a second wave. Thus the nonlinear behavior of two coupled waves, to be investigated in this thesis, can differ qualitatively and quantitatively from the behavior of a single wave.

Figure 3.3 shows schematically the development of induced modulational instability. Graphs (a) and (b) show schematic representations of the power vs. frequency spectrum and power vs. time profile, respectively, for two low power co-propagating waves. Graphs (c), and (d) - (e) show the power vs. frequency and power vs. time responses, respectively, of two co-propagating waves in the regime of induced modulational

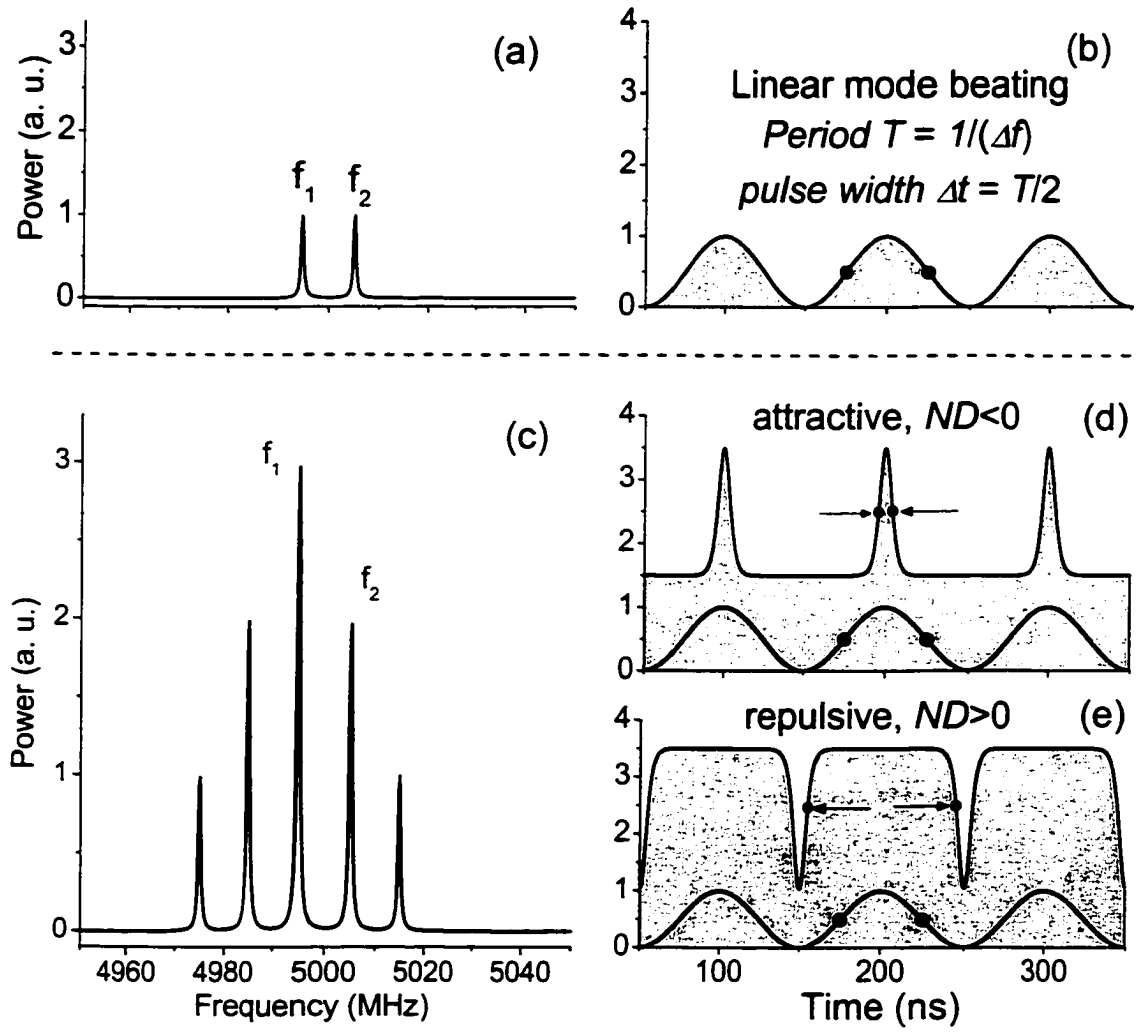

Figure 3.3. Schematic representation of bright and dark soliton pulse train formation due to the induced modulational instability of two waves. Graph (a) is a schematic of the power vs. frequency spectrum of two cw signals at low power. Graph (b) is the corresponding envelope power vs. time profile. Graph (c) is a schematic of the power vs. frequency spectrum of two cw signals above the power threshold for induced modulational instability. Graphs (d) and (e) are the corresponding bright and dark envelope power vs. time profiles for attractive and repulsive nonlinearity, respectively.

instability. In the frequency spectra shown in (a) and (c), the initial frequencies f_1 and f_2 are labeled. In the time domain, shown in (b), (d), and (e), linear and nonlinear mode beating profiles are shown. The shaded regions in (b), (d), and (e) indicate where the carrier signal exists. The two black dots in each of the time response graphs are indicative of the pulse width.

Graph (a) shows two equal power spikes in the frequency spectrum expected for the linear response of two co-propagating waves. Graph (b) shows the power envelope time domain response with the expected unity modulation depth and the $\sin^2(2\pi\alpha t)$ envelope shape, where $\alpha = |f_1 - f_2|/2$. The period of this power envelope is $T = 1/|f_1 - f_2|$ and the half power pulse width is $\Delta t = T/2$. The half power points are indicated in (b) by the black dots. Graph (d), as compared to graph (a), shows the appearance of additional satellite harmonics in the frequency spectra for the higher power regime of induced modulational instability. Note that the separation between adjacent satellite harmonics is equal to the separation in frequency of the initial signals f_1 and f_2. Also note that the power level of these harmonics decreases as one moves away from the carrier frequency f_1.

The profiles in (d) and (e) are indicative of the nonlinear time responses in the induced modulational instability regime. The shapes of the pulses in (d) and (e) can be attributed, in part, to the multiple frequency harmonics in (c). In (d), the higher power attractive nonlinearity causes a narrowing of the bright crests in the linear profile. It is as though the half power points in graph (c) were attracted to one another in the high power case to form these bright nonlinear pulses. This "attraction" may give rise to a bright

soliton pulse train. In (e), the higher power repulsive nonlinearity causes a narrowing of the dark dips in the linear profile. It is as though the half power points in graph (c) were repelled from one another in the high power case to yield dark nonlinear pulses. This "repulsion" may give rise to a dark soliton pulse train. In fact, the formation of nonlinear bright and dark *soliton* pulse trains, due to self and induced modulational instability in nonlinear dispersive media, was observed [see, e.g., Refs. 2 – 5 and 9 – 10].

The development of the induced modulational instability shown schematically in Figure 3.3 can be realized experimentally through the propagation of two cw signals in a nonlinear dispersive media. The induced modulational instability mechanism is observed for large amplitude waves. The nonlinear interaction of the two cw signals above this threshold gives rise to satellite harmonics in the frequency spectrum. In the time domain, a nonlinear pulse train is formed. Through the proper choice of parameters, bright and dark *soliton* pulse trains may be obtained. This thesis is devoted to the investigation of such soliton trains. Due to the width of the frequency spectrum of these pulse trains, their description could require analysis based on a system of coupled NLS equations. However, in this thesis, the single NLS was used to model the formation of such pulses where possible.

3.4 Group Velocity, Dispersion Coefficient, and Nonlinearity for Magnetostatic Spin Waves

The evaluation of the group velocity v_g, dispersion coefficient D, and nonlinear term N for MSW excitations is necessary in order to compare the predictions of the NLS

equation model to the results. The dispersion relations for MSSW and MSBVW excitations obtained in Chapter 2 will be used to evaluate explicitly the group velocity and dispersion coefficient. For the evaluation of the nonlinear coefficient a modified dispersion relation, which depends on the square of the wave amplitude, will be used. This modified dispersion relation will be explained later in this section. The parameters of the NLS equation for MSW excitations were first considered in detail by Zvezdin and Popkov [22].

The dispersion relations for MSSW and MSBVW excitations are given by Equations (2.13) and (2.15), respectively. In order to obtain the group velocity for the NLS equation the first partial derivative of these relations with respect to k is taken and is then evaluated at $k = k_0 \to 0$. The carrier wave number is allowed to vanish for simplicity. However, recall that the excitations to be used in this thesis are around 100 rad/cm. Therefore, the difference between the coefficients in the NLS equation evaluated at 0 or 100 rad/cm is small. The resultant relation for surface waves is

$$v_g^{(MSSW)} = \frac{\omega_M^2 S}{4\omega_B}. \tag{3.16}$$

Whereas for backward volume waves the group velocity parameter is given by

$$v_g^{(MSBVW)} = -\frac{\omega_M \omega_H S}{4\omega_B}. \tag{3.17}$$

Note that for MSBVW excitations the group velocity is negative. This is an indication of the "backward" nature of these waves. The difference between the values of the group velocity at 0 and 100 rad/cm is 10 % for MSSW excitations and only 5 % for MSBVW excitations. For the analyses in this thesis this precision is acceptable.

In order to recover the dispersion coefficient for the NLS equation, one need simply

take a second derivative of the dispersion relations with respect to k, and evaluate the results at $k = 0$. These coefficients are critical for the evaluation of the attractive or repulsive nonlinearity of MSSW and MSBVW excitations mentioned in Section 3.1. For surface waves the dispersion coefficient is given by

$$D^{(MSSW)} = -\frac{\omega_M^2 S^2}{2\omega_B}\left[1+\frac{\omega_M^2}{8\omega_B^2}\right]. \tag{3.18}$$

For backward volume waves the dispersion coefficient is given by

$$D^{(MSBVW)} = \frac{\omega_M \omega_H S^2}{2\omega_B}\left[\frac{1}{3}-\frac{\omega_M \omega_H}{8\omega_B^2}\right]. \tag{3.19}$$

Note that the dispersion coefficient for MSSW excitations is negative and the dispersion coefficient for MSBVW excitations is positive. The signs of these coefficients are also evident from the curvature of the dispersion relations plotted in Figure 2.8 of Chapter 2.

In order to recover the nonlinear coefficient one must first consider a wave amplitude dependent dispersion relation of the form given by Equation (3.6). For the case of MSW excitations, the $|u|^2$ dependence enters the dispersion relations through the ω_M term. As alluded to at the end of Section 2.1, for large values of the dynamic component of the magnetization the value of $\omega_M = |\gamma| 4\pi M_S$ may be replaced by

$$\omega_M \rightarrow |\gamma| 4\pi M_S (1-|u|^2) = \omega_M (1-|u|^2). \tag{3.20}$$

With this modified value of ω_M inserted into the dispersion relations given by Equations (2.13) and (2.15), wave amplitude dependent dispersion relations of the form of Equation (3.6) are recovered. The values of the nonlinear coefficients for MSSW and MSBVW excitations can be obtained from these new relations by differentiating with respect to

$|u|^2$. When evaluated at $k=0$ and $|u|^2=0$, the values of N for the MSSW and MSBVW cases are equal and are given by

$$N^{(MSSW)} = N^{(MSBVW)} = -\frac{\omega_H \omega_M}{2\omega_B}. \tag{3.21}$$

Note that for both MSSW and MSBVW excitations the value of the nonlinear coefficient is negative. This means that, as the value of the dynamic component of the magnetization increases, the frequency of the excitation decreases.

From these values and the values of the dispersion coefficients it is clear that the condition for attractive nonlinearity, $ND < 0$, is satisfied for MSBVW excitations. Furthermore, the condition for repulsive nonlinearity, $ND > 0$, is satisfied for MSSW excitations. Therefore, one would expect from the predictions of the single NLS equation that dark solitons are supported by MSSW excitations and bright solitons are supported by MSBVW excitations. Furthermore, modulational instability is observable only for MSBVW excitations. The formation of solitons and *induced* modulational instability, as predicted by the single NLS equation model, are observed in this thesis. In addition, the formation of bright and dark soliton-like pulse trains formed due to *induced* modulational instability was observed for cases not predicted by the NLS equation model.

The theory presented here and in Chapter 2 constitutes the theoretical basis for the results. In some cases, the equations obtained in Chapters 2 and 3 will be used to compare with the experimental results. These comparisons will be presented in Chapters 5 and 7.

CHAPTER 4

MEASUREMENT SYSTEMS AND TECHNIQUES

Two measurement systems, the frequency filtered active resonant ring (ARR) system and the inductive magnetodynamic probe (IMP) system, were developed for the investigation of linear and nonlinear MSW excitations. A YIG film delay line and microwave generation and detection instrumentation are central to these systems. In this chapter, these central elements will be described first. Then, from the basis of these elements, the frequency filtered ARR and IMP systems and their peripheral elements will be described in detail.

Section 4.1 will describe the YIG film delay line. Section 4.2 will describe the central microwave instrumentation. In section 4.3, the frequency filtered ARR system and its operation will be described. In section 4.4, the IMP system and its operation will be described. Sections 4.3 and 4.4 will conclude with a short summary of the measurements to be performed with the respective systems.

4.1 The YIG Film Delay Line

Figure 4.1 shows a schematic representation of the YIG film delay line which is a key element of the frequency filtered ARR and IMP systems. These systems will be used to perform the experiments on linear and nonlinear MSW excitations in thin YIG films to be described later. Through the use of Figure 4.1, the components of the full delay line assembly, and how the assembly allows for the excitation and detection of MSW signals, will be described. In addition, a representative transmitted power and phase vs. frequency characteristic of the delay line in the MSBVW configuration will be given and explained. This explanation will rely on the MSBVW dispersion relation obtained in Chapter 2.

The YIG film delay line assembly depicted in Figure 4.1 consists essentially of three pieces; (1) a YIG film waveguide under an applied static magnetic field, (2) planar microstrip transmission lines, and (3) a housing. The rectangular thin ferrite film waveguide represented in Figure 4.1 consists of a thin ferrite film on a dielectric substrate. For the experiments, the waveguide was cut from low microwave loss single crystal YIG grown on large disks of 0.5 mm thick gadolinium gallium garnet substrates by the method of liquid phase epitaxy (LPE) [23]. The chemical formula for YIG is $Y_3Fe_5O_{12}$. Two separate YIG samples were used in this thesis. One of the samples used was provided by Dr. J. Douglas Adam of Northrop Grumman, Baltimore, Maryland. This sample was 4.4 μm thick and was used in the linear MSW signal response measurements presented in Chapter 5. The other sample was provided by Prof. Boris A. Kalinikos of St. Petersburg Electrotechnical University, St. Petersburg, Russia. This sample was 6.9 μm thick and was used throughout the nonlinear measurements to be

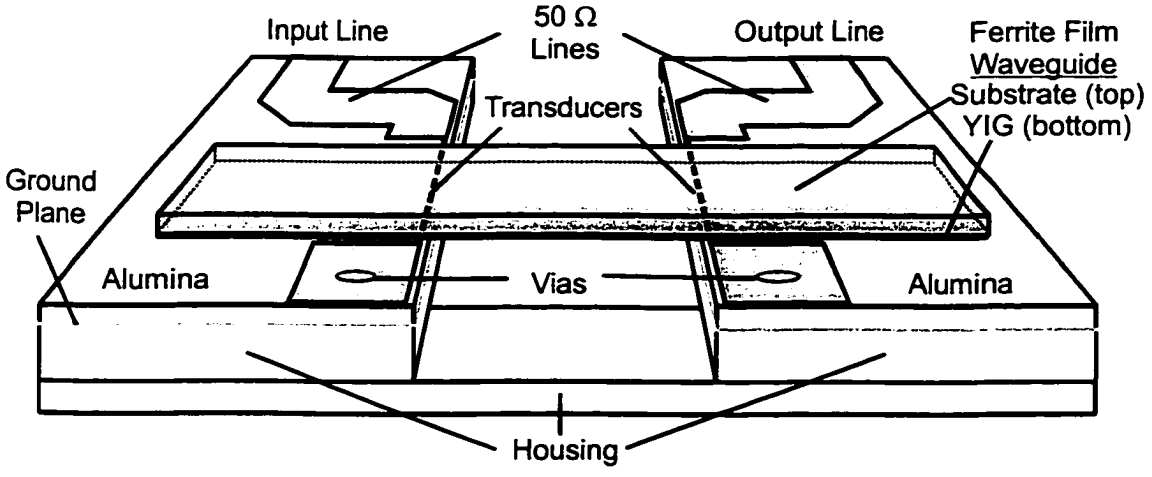

Figure 4.1. Schematic representation of YIG film delay line assembly.

presented in Chapters 6 and 7.

For use in the delay line, both samples were cut from disks into long narrow rectangular waveguides with a diamond saw. The 4.4 μm thick sample was cut into a 2 mm wide, 17.9 mm long waveguide. The 6.9 μm thick sample was cut into a 1.4 mm wide, 18.8 mm long waveguide. The lengths of the waveguides were chosen in order to avoid reflections from the ends which could interfere with the measurements. Due to the roughness of the diamond saw blade, it was necessary to polish the edges of the waveguides in order to avoid additional losses due to edge imperfections. These waveguides were placed YIG face down on the microstrip transducers of the delay line as shown in Figure 4.1. For the experiments, the waveguide was magnetized in either the MSSW or MSBVW configuration. These configurations are described in Chapter 2.

Consider now the planar microstrip transmission lines shown in Figure 4.1. Each line consists of three parts; (1) a silver ground plane, (2) a specially designed microwave signal conducting line with via contact to the ground plane on the opposite side, and (3) a 0.5 mm thick alumina substrate with $\varepsilon_r \simeq 10$ which separates the ground plane and the conductor. The ground plane and the grounded conducting line are obtained from 5 μm thick silver which coats both sides of an alumina substrate.

The conducting lines used in all the experiments were fabricated from silver on an alumina substrate through a standard photolithographic technique [24]. The fabrication was performed by Professor Boris A. Kalinikos in St. Petersburg, Russia. The conducting line consists of a wide 50 Ω section and a narrow transducer section terminated with a via contact through the alumina substrate to the ground plane. The 50 Ω section of the conductor is represented in Figure 4.1 by the thick shaded part of the

line, while the narrow transducer is represented by the thin dotted black line under the YIG film. The width of the 50 Ω section of the line is approximately equal to the 0.5 mm thickness of the alumina substrate [24] and provides minimum impedance mismatch with the other 50 Ω microwave components of the measurement system. The narrow transducer section of the line is 50 μm wide and 2 mm long. This size does introduce an impedance mismatch but simultaneously allows for broad band excitation and detection of MSW signals. The via ground termination of the conducting line is represented by the shaded circle on the square pad in Figure 4.1. This via hole is coated with silver to provide an ohmic contact between the conducting line and the ground plane. The ground plane is in contact with the delay line housing to be described below.

Consider now the delay line housing. The design requirements of the housing will be described here. First, the housing must be made from a nonmagnetic material, usually aluminum or brass, and fit within electromagnet pole pieces separated by a minimum of six inches. Second, the housing should hold the planar microstrip transmission lines such that the ground plane is in ohmic contact with the metal housing. Third, the part of the housing which holds the microstrip transmission lines should allow for a variation in the separation between the individual transmission lines. Fourth, the housing should hold two SMA flange mount jacks which are also in ohmic contact with the delay line housing. These jacks allow for the application of microwave power to the input line and reception of microwave power from the output line through an interface between 50 Ω SMA coaxial cable and the planar transmission lines. Since the ground plane of the transmission line and the ground of the SMA cable are both in ohmic contact with the delay line housing, the entire system shares the SMA cable ground. It should be noted

here that, for use in the IMP system, the delay line housing must be modified to expose the YIG film surface to the inductive probe.

Now that the assembly of Figure 4.1 has been described, the delay line excitation and detection of MSW signals may be described. A mathematical explanation of MSW excitation and detection is given by Stancil [see 11 and Refs. therein], among others. A more qualitative and physical explanation will be given here. When microwave power is applied to the input transmission line, a microwave current propagates down the line to the narrow transducer section. When the current travels down the narrow transducer, a microwave field radiates into the area above the transducer. Due to the high dielectric constant of the transmission line, these fields radiate from the transducer into the near field [24] where the YIG film waveguide is positioned. This radiating magnetic field drives the magnetic moments in the region close to the transducer. These driven moments couple to other moments and a wave propagates down the sample. Since the wave which propagates down the sample is also radiating from the surface of the sample, a microwave current is induced in the receiving transducer. In this way the reception and detection processes of the delay line are reciprocal. The term "delay line" comes from the fact that the magnetization waves have a group velocity much lower than that of the "fast" electromagnetic (EM) waves as explained in Chapters 2 and 3. Thus, there is a delay between the magnetization and EM waves.

As mentioned earlier, the maximum excited wavelength is determined by the width of the transducer used in the delay line and is given approximately by the relation

$$k_{max} \sim \frac{2\pi}{W}, \tag{4.1}$$

where W is the width of the transducer. This corresponds to a k_{max} on the order of 10^3

rad/cm. In the experiments, the spin wave excitations have wave numbers near 100 rad/cm, well below k_{max} and above the wavelength of the pure "fast" EM waves. As explained in Chapter 2, spin waves in this region are referred to as magnetostatic spin waves.

Figure 4.2 shows a representative transmitted power and phase vs. frequency characteristic of the delay line in the MSBVW configuration with the 4.4 μm thick YIG film waveguide. Figure 4.2 (a) shows the transmitted power while (b) shows the phase. A microwave signal of constant power was applied to the input of the YIG film delay line and the signal frequency was swept. In the particular case of Figure 4.2 the constant power level was -10 dBm. This power level is well within the linear regime. The distance between the input and output transducers of the delay line was 0.9 cm and the applied magnetic field was approximately 1200 Oe.

First consider Figure 4.2 (a). The power level of the signal from the output transducer of the YIG film delay line was sent to a signal analyzer and measured as a power level in dBm for the span of frequencies within the sweep. The resultant transmitted power vs. frequency profile is shown in (a).

Now consider Figure 4.2 (b). For the acquisition of this phase profile, the signal received by the signal analyzer from the output transducer of the delay line was compared to a reference signal of the same frequency. The phase difference, in degrees, between the signal from the output of the delay and the reference signal was measured by the signal analyzer for all the values of the frequency within the sweep. This profile is shown in Figure 4.2 (b) and constitutes the phase vs. frequency characteristic of the delay line.

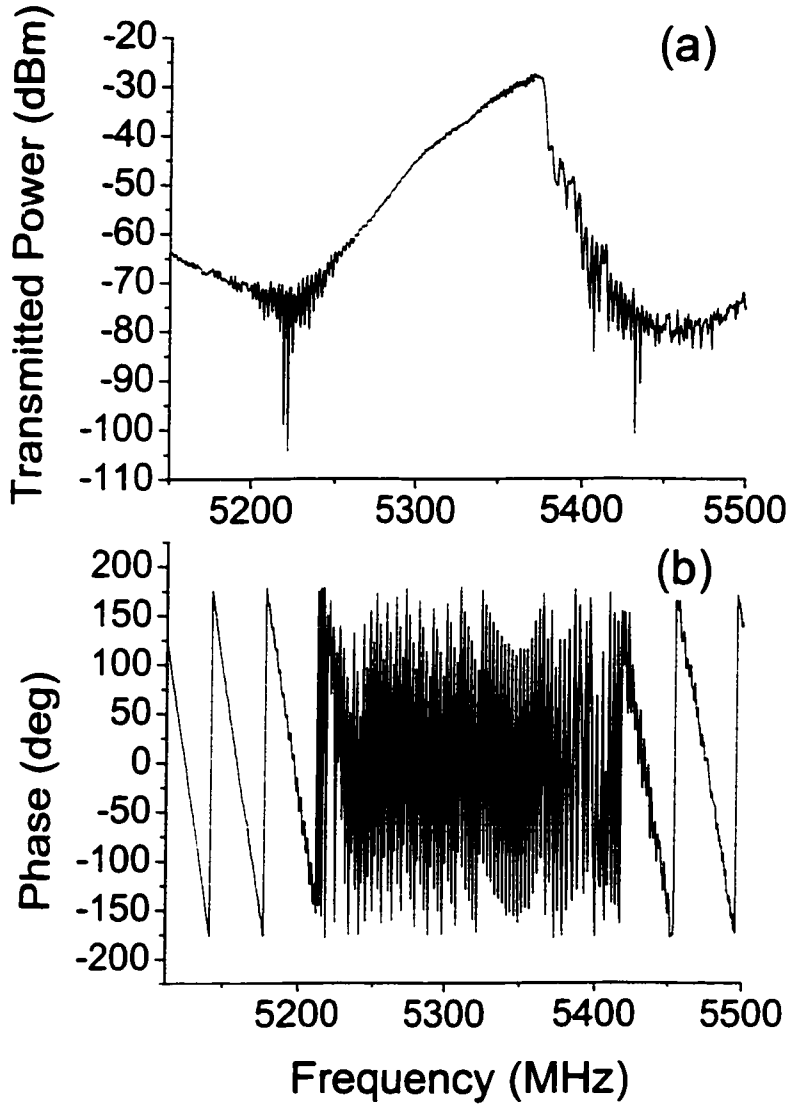

Figure 4.2. Representative transmitted power and phase vs. frequency characteristics of the YIG film delay line in the MSBVW configuration.

It is easy to explain the shapes of the characteristics in Figure 4.2. The arguments to be presented here are based on the dispersion relation for MSBVW excitations and can be generally applied to the MSSW case. Recall the shape of the dispersion characteristic for MSBVW excitations shown in Figure 2.7. It is clear from the dispersion characteristic that MSBVW excitations with higher frequency have higher group velocity. When considered in the time domain, the waves with higher group velocity which propagate down the length of the sample will experience smaller attenuation. This fact, along with the lower excitation efficiency of higher k waves, is reflected in the transmitted power vs. frequency characteristics shown in Figure 4.2 (a). The upper frequency band edge, seen in (a) as the point of lowest attenuation, corresponds approximately to the minimum excited wave number where the group velocity is highest.

The phase vs. frequency characteristic shown in Figure 4.2 (b) may also be explained from the consideration of the dispersion for MSBVW excitations. It is clear from the figure that, within the band of MSBVW excitations seen in (a), the phase changes very rapidly. Outside this excitation band the phase changes relatively slowly due to the detection of a "fast" EM leakage signal. The difference in the phase change in these two regions is reflective of the "slow" wave nature of MSW excitations relative to the direct "fast" wave nature of the EM leakage. Though it is difficult to see in the scale of graph (b), the phase change for the lower frequency MSBVW excitations is slightly more rapid than for the higher frequency excitations. This fact is also a reflection of the shape of the dispersion characteristic. In fact, in the next chapter, characteristics like those in Figure 4.2 will be used to obtain the dispersion characteristics ω vs. k for MSBVW and MSSW excitations.

4.2 Microwave Generation and Detection Instrumentation

With the delay line described, the microwave generation and detection instrumentation can be addressed. With this instrumentation and the YIG film delay line described in Section 4.1, basic MSW experiments have been performed [see, e.g., 4]. The ARR and IMP systems, to be described in the last two sections, are augmentations of this basic experimental system.

Figure 4.3 shows a block diagram of the basic MSW experimental system which contains the central microwave instrumentation. The instrumentation can be considered in two arms, an input arm and an output arm, connected to the YIG film delay line situated between the pole pieces of an electromagnet. The input arm consists of two microwave sources, a power amplifier, and a 30 dB directional coupler. The input arm supplies microwave power to the input of the delay line and a 30 dB down reference signal to a signal analyzer. The output arm consists of three signal analyzers and a pair of 3 dB directional couplers. The output arm is used to analyze the signal from the output of the delay line. In Figure 4.3 the YIG film delay line is shown schematically oriented in the MSBVW configuration, though the MSSW configuration was also accessible.

First consider the microwave generation equipment of the input arm. The key elements to the input arm are the Hewlett-Packard (HP) synthesized sweepers, labeled microwave source A and B in Figure 4.3. These sources were used to provide frequency and power stable microwave signals to the YIG film delay line. Source A is a model HP83623B synthesizer sweeper. Source B is a model HP83650A synthesized sweeper.

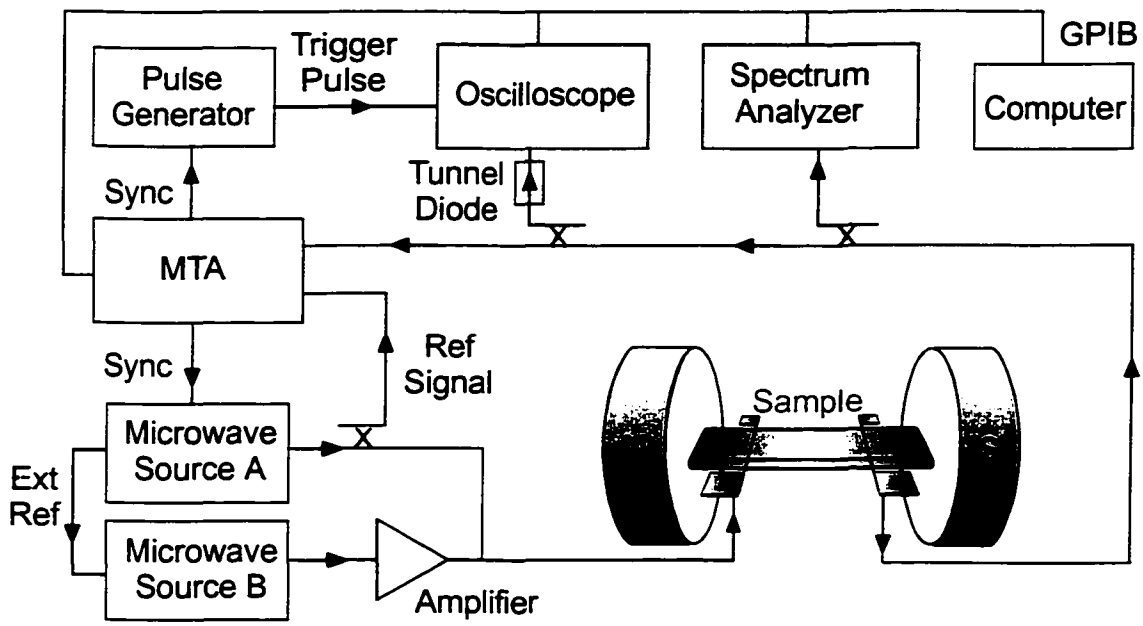

Figure 4.3. Schematic representation of the input arm, delay line, and output arm. The input arm consists primarily of the microwave sources which provide the input signal to the delay line and a reference signal to the MTA. Source B is referenced to source A. A schematic of the YIG film delay line is shown with the external magnetic field represented by two pole pieces of an electromagnet. The output arm consists of signal analyzers and a pulse generator. The pulse generator is used as a trigger signal for the oscilloscope. The microwave sources and the pulse generator are controlled by the MTA through 20 MHz synchronization connections. Data is acquired from the MTA, oscilloscope and spectrum analyzer with LabView programs facilitated by GPIB connections to a computer. Where appropriate, the arrows indicate the direction of the microwave signal.

The frequency range of source A was 50 MHz to 20 GHz and the dynamic power range was –20 to 25 dBm. The frequency range of source B was 50 MHz to 50 GHz and the dynamic power range was –20 to 18 dBm. The sweepers were equipped with a HP general purpose interface bus (GPIB) which made the interface with a computer or other similarly equipped devices possible. Additionally, source A provides a 20 MHz reference signal to source B. In this way source B is externally referenced to source A. This synchronization provides the stability necessary for the experiments.

Consider now the signals applied to the input of the delay line from sources A and B shown in Figure 4.3. The microwave signal supplied by source A is separated by a 30 dB directional coupler. The 30 dB down signal from the coupler is sent to one input of the microwave transition analyzer (MTA). This signal is used primarily as a reference for phase measurements. The direct signal from the coupler is sent to the input of the delay line. Consider now the signal from source B. The microwave signal supplied by source B is amplified by the power amplifier. The amplifier, manufactured by Narda/DBS, operates in the frequency range between 2 and 8 GHz and has a maximum output power of approximately 27 dBm. Therefore, the signals from source A and B have approximately the same maximum power at the input of the delay line. The signals from one or both of these sources may be used to excite MSW signals as described in Section 4.1.

Now consider the microwave detection equipment of the output arm. The most important components of the output arm are the signal analyzers. In Figure 4.3 the signal analyzers are the rectangles labeled MTA (microwave transition analyzer), spectrum analyzer, and oscilloscope. These signal analyzers allow for a wide variety of

measurements to be performed on the signal from the output of the delay line. Consider first the MTA. The HP71500A MTA is capable of measuring the amplitude and phase vs. time response of a microwave output signal. In addition, a GPIB connection with microwave source A allows one to perform additional measurements which include: (1) frequency swept power and phase measurements and (2) power swept measurements. The MTA, and the other signal analyzers, were connected through a GPIB interface to a computer in order to facilitate data acquisition through National Instruments LabView programs.

The MTA also acts as a master to the system. Through two 20 MHz synchronization connections, the MTA controls both the HP8161A pulse generator and source A of the input arm. Since the MTA controls both source A and the pulse generator, the pulse generator can be used to provide a trigger pulse to the HP Infiniium oscilloscope to be described below. This trigger pulse is referenced to a certain fixed phase angle of the signal from source A. In this configuration, the oscilloscope is sensitive to phase changes in the envelope signal from the output of the delay line.

The HP54845A Infiniium oscilloscope and the HP8593E spectrum analyzer were used to perform additional power vs. time and power vs. frequency measurements, respectively. The signal applied to the oscilloscope was first converted to a power by a microwave tunnel diode with a rise time of approximately 1 ns. This power from the diode was registered on the screen of the oscilloscope as a voltage. The oscilloscope and the MTA were used to measure the power vs. time profiles of single and multi-harmonic signals from the output of the delay line. The HP spectrum analyzer was used to measure the power vs. frequency characteristics of these signals.

When considered together, the input arm, the output arm, and the delay line constitute the basic MSW measurement system. This basic measurement system is the basis of the frequency filtered ARR and IMP measurement systems used to perform all the measurements to be presented in this thesis. The active resonant ring (ARR) and inductive magnetodynamic probe (IMP) systems and their operation will be considered in the next sections.

4.3 The Frequency Filtered Active Resonant Ring System

For the frequency filtered active resonant ring (ARR) system, the YIG film delay line, with a modified transducer design, is connected in a feedback loop. This configuration of the delay line gives rise to a resonance condition and the design of the transducers gives rise to a specially tailored symmetrical transmitted power vs. frequency characteristic of the YIG film delay line. This system will be used in the self generation of trains of stable spin wave envelope solitons to be presented in Chapter 6. The configuration of the delay line will be described first, followed by a description of the specially designed transducers.

Figure 4.4 shows the frequency filtered ARR system. The YIG film delay line is connected in a feedback loop with the power amplifier, discussed above, and a variable attenuator. The directional couplers DC1 and DC2 provide a connection between the ring and the microwave detection and generation equipment, respectively. The variable attenuator, manufactured by Narda, has a frequency range of 2 – 8 GHz and provides attenuations from 0 to 100 dB.

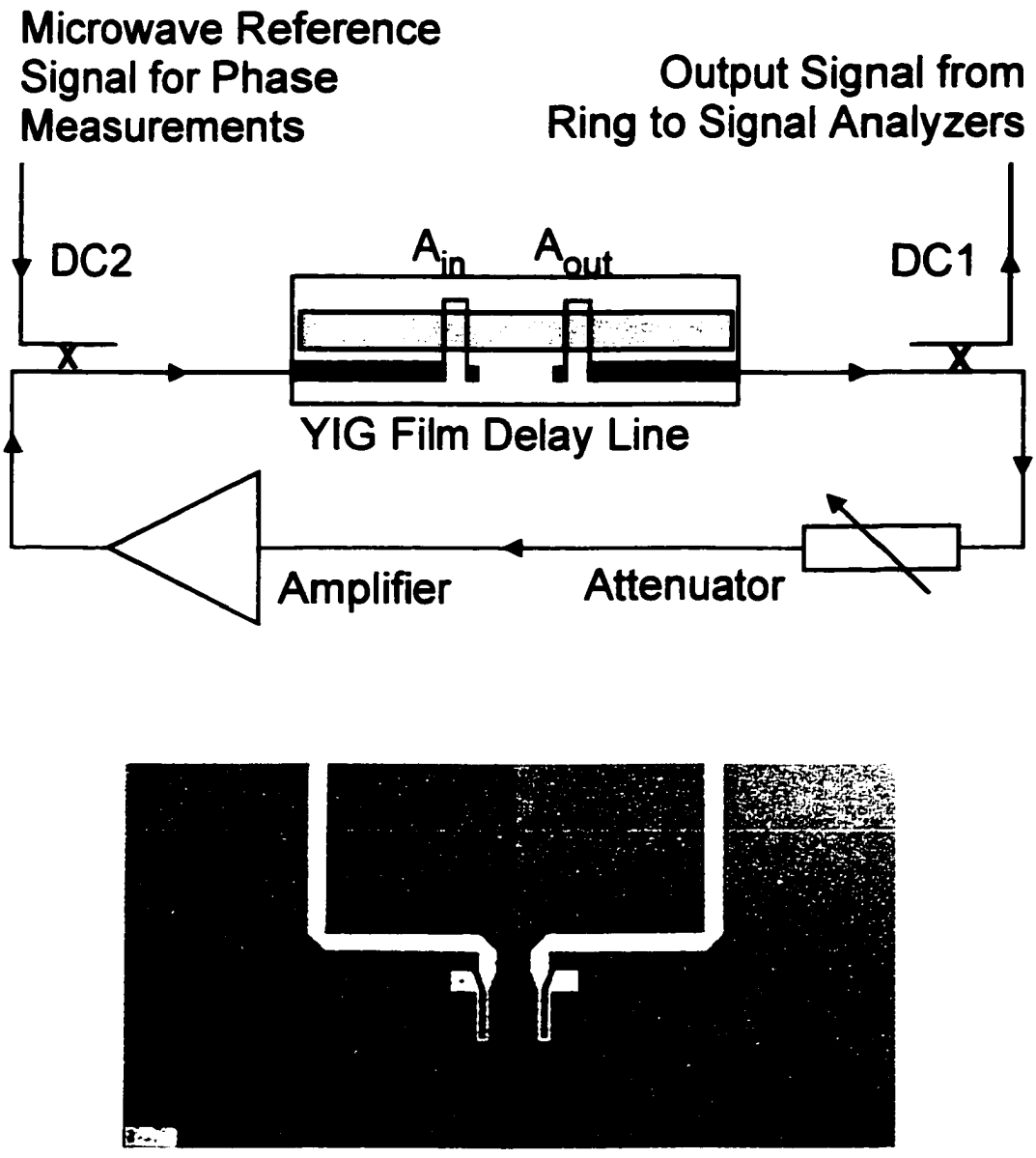

Figure 4.4. Schematic representation of the frequency filtered active resonant ring (ARR) system. The diagram shows the delay line connected in a ring with an amplifier and an attenuator. The directional couplers, labeled DC1 and DC2, are for microwave signal application and detection. Where appropriate, the arrows indicate the direction of the microwave signal. The input and output u-shaped transducers are labeled. The photograph shows an enlarged view of the u-shaped transducers used in the experiments. The distance between each element of the u-shaped transducers in the photo is 0.26 mm.

When connected as shown in Figure 4.4 the active ring has a resonance condition given by

$$k_n(\omega)L + \phi_e = 2\pi n, \qquad n = 1,2,3..., \tag{4.2}$$

where $k_n(\omega)$ is the wave number of the MSW excitation in the ring, L is the separation between the transducers of the delay line, and ϕ_e is the phase associated with the electronic components of the ring [1]. The ARR structure will self oscillate when the gain, introduced by the active amplifier, compensates for the losses in the ring. The accessible frequencies for this oscillation are determined by the ring resonance condition given by Equation (4.2). At the threshold of oscillation, the frequency with the lowest losses will begin to oscillate. The frequency of this resonance can be controlled with the antenna separation and design. Typically, the parameters are chosen such that the oscillation occurs for approximately $n = 5$. When the gain in the ring increases, through a decrease in the variable attenuator setting, a comb of frequencies is excited in the ring. These resonances are phase locked due to the induced modulational instability mechanism which exists at these high ring gains and frequency separations.

When the ring self oscillates, in the linear or nonlinear regime, a microwave signal propagates around the ring. In the experiments, this signal is coupled to the signal analyzers, described in Section 4.2, through the 3 dB directional coupler DC1 shown in Figure 4.4. The application of a microwave signal to the ring, through the 30 dB directional coupler DC2, was also necessary. This signal allowed for the characterization of the ARR structure. In addition, a direct signal was sent to the MTA and used as a synchronization and reference signal for phase measurements on the signal from the output of the ring. For the phase measurements, the signal sent to the ring was made

small to ensure that its influence on the self oscillation of the ring was negligible.

Consider now the specially designed transducers used in the delay line labeled A_{in} and A_{out} in Figure 4.4. As with the single element transducers, the u-shaped transducers are 50 μm wide and made from silver on an alumina substrate. A photograph of the actual transducers is shown under the schematic in Figure 4.4. The rest of the transmission line in Figure 4.4 is identical to that of the transmission line of Figure 4.1. The u-shaped transducers provide a filtering characteristic of the delay line which is different from the single element transducers shown in Figure 4.1. The transmission characteristic will not be given here but instead in the chapter on results. However, some qualitative remarks about its shape will be given.

The transmitted power vs. frequency characteristic of the u-shaped transducers is similar to that of the single transducer, but with a reduced bandwidth and a modified shape. The MSW pass band starts for signals at zero wave number as for the single element antenna. However, since each element of the u-shaped transducer excites an MSW signal, some interesting artifacts in the transmitted power vs. frequency characteristic appear. These artifacts arise due to the interference between the two excited signals. First, the maximum excited wavenumber is decreased from the value given by Equation (4.1). This occurs when the signals from each element of the u-shaped antenna interfere destructively for a null output. Due to the fact that the signals from each element of the transducer are excited 180° out of phase, destructive interference occurs for

$$k_{\max} \sim \frac{2\pi}{d}. \tag{4.3}$$

In Equation (4.3), d is the distance between the individual elements of the u-shaped transducer. In the experiment d is 0.026 cm and therefore $k_{max} \approx 250\,\text{rad/cm}$. This is an order of magnitude smaller than the maximum wavenumber excited by the single element transducer. This creates a transmitted power vs. frequency characteristic which is narrower in frequency than that of the single element transducer characteristic. Additionally, the shape of the pass band is slightly modified by the continuous transition between the destructive and constructive interference of the two excited MSW signals. The resultant shape matches approximately the symmetrical frequency spectrum of a single SWE soliton. This modified characteristic was chosen in order to facilitate the stable generation of soliton trains in the ring. The filtering suppresses the excitation of spurious frequency harmonics in the ring which may lead to instability in the soliton train. The details of this excitation will be given in Chapter 6 on the results on soliton self generation.

4.4 The Inductive Magnetodynamic Probe System

The IMP (inductive magnetodynamic probe) system is essentially the addition of a scanning localized probe [25] to the MSW delay line. The probe provides an additional means of signal acquisition from the YIG film surface. Aside from the linear measurements to be presented in Chapter 5, the newly developed IMP system will be used in the experiments on the formation of solitons due to the induced modulational instability of co-propagating MSW excitations presented in Chapter 7. Figures 4.5 and 4.6 show a schematic and photograph, respectively, of the IMP system. The upper

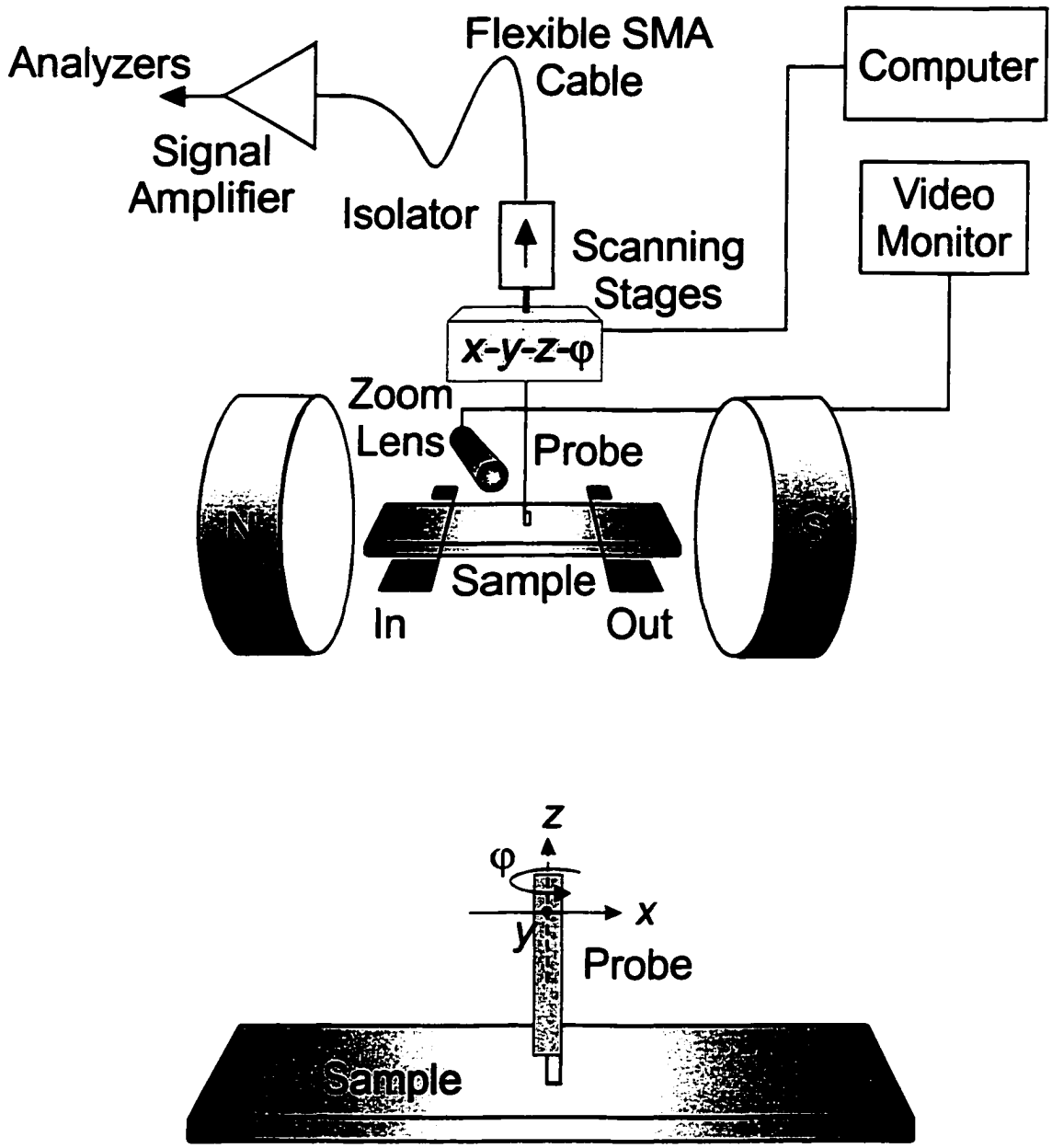

Figure 4.5. Schematic representation of the IMP measurement system. The upper diagram shows the IMP system overview. The lower diagram shows the probe-sample geometry on an enlarged scale.

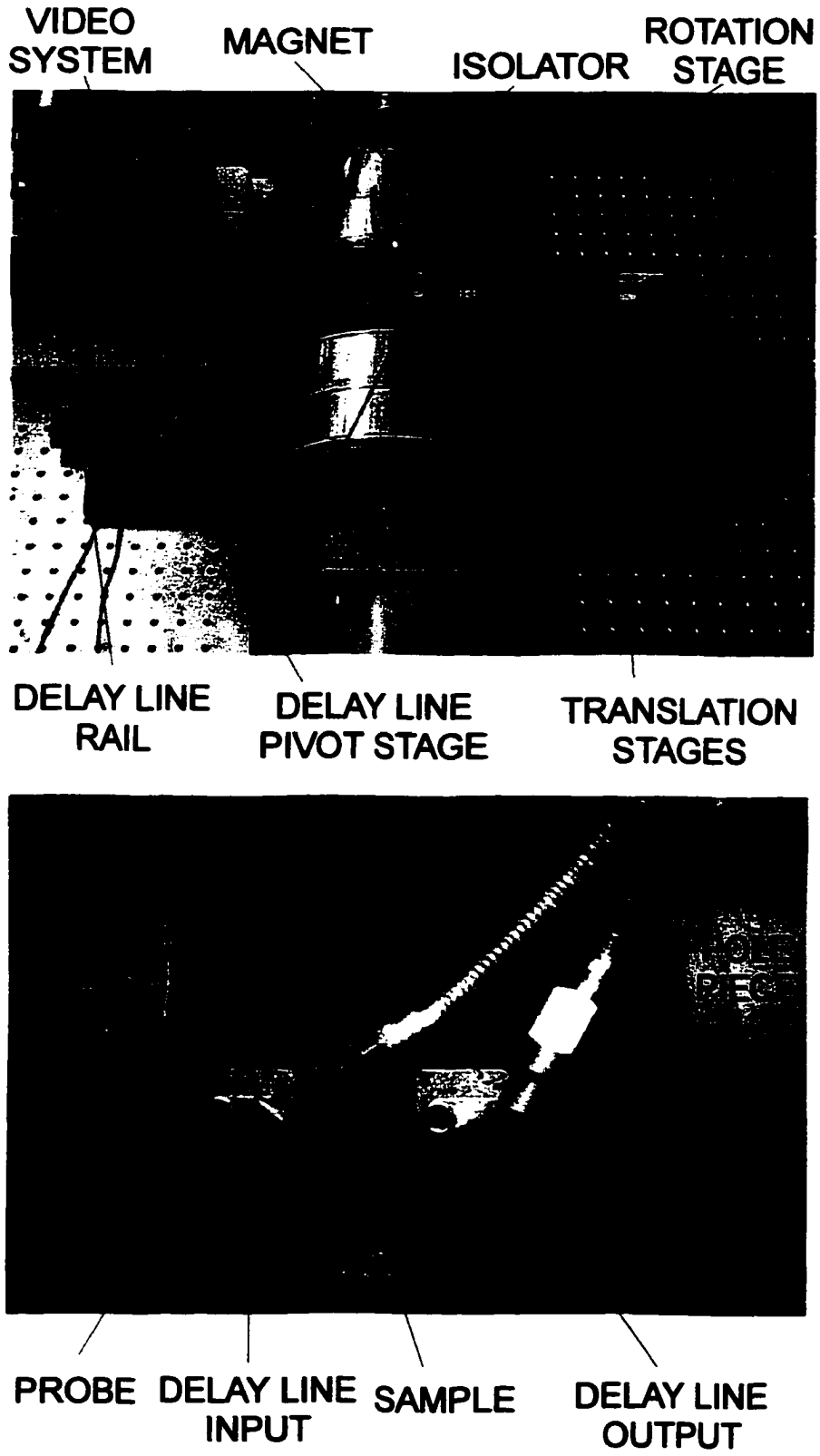

Figure 4.6. Photographs of the IMP measurement system. The upper photograph shows an overview of the IMP system. The lower photograph shows the probe-sample geometry within the magnet gap.

images in each figure show the system overview while the lower images show the probe-sample geometry within the pole pieces of the electromagnet.

The probe system consists of four main parts: (1) the scanning and rotation stages, (2) the video zoom system, (3) the delay line stage, and (4) the probe. The components of the IMP system will be described followed by an overview of the operation of the IMP system. The description and operation of the IMP system will rely heavily on Figures 4.5 and 4.6.

The translation and rotation stages used in the IMP system were provided by OWIS GmBh. Three translation stages were assembled in a standard $x - y - z$ configuration. The $x - y$ stages were OWIS 2 phase stepper motor LM60 translation stages and were used to control the scanning plane of the probe. These stages were computer controlled through a stepper motor SM30 PC card through a LabView program. An OWIS manual VT80 translation stage was added as a z stage. At the end of an arm attached to the z stage, an OWIS 2 phase stepper motor DMT40 rotation stage was attached. The rotation stage was modified in order to accept the probe assembly. The resolution of the LM60 translation stages was better that 0.5 μm. The resolution of DMT40 rotation stage rotation was better than $0.01°$. The resolution of the VT80 stage probe was better than 1 micron. This assembly was attached to a rail on a vibration resistant honeycomb breadboard. This breadboard was then positioned flush with the electromagnet. The translation-rotation assembly was then positioned along the rail such that the rotation stage was centered directly above the open space between the pole pieces of an electromagnet. This configuration is clearly shown in Figure 4.6.

The video zoom system consists of a zoom camera and a Sony Trinitron monitor

PVM – 14N6U purchased from Edmund Industrial Optics (EIO). The zoom camera consists of an EIO model number 52 – 460 CCD camera, an EIO model number 54 – 671 video zoom microscope, an EIO model number 54 – 175 ring illuminator, and an EIO model number 53 – 953 light source. This zoom camera assembly was connected to a boom stand and positioned on the opposite side of the electromagnet from the translation-rotation stage assembly. In this way the probe and YIG film sample, positioned within the electromagnet pole pieces, was visible. With the video zoom system it was possible to resolve sizes much smaller than one micron on the Sony Trinitron monitor.

The delay line is essentially the same as the one described in Section 4.2 except that here special modifications were made to expose the YIG film surface to the rotation stage and, thus, the probe. This newly designed delay line structure is placed on an optical post and connected to an optical rail in the same way as the translation stages described above. The optical rail is connected to a metal plate. The metal plate is connected to another honeycomb breadboard. Tension springs separate this connection and allow for the orientation of the sample plane. This capability is needed to insure that the scanning plane of the probe is the same as the plane of the YIG film. This assembly is placed on the same side of the electromagnet as the video zoom system. In this position, the rail extends into the electromagnet so that the delay line can be positioned between the magnet pole pieces.

The probe consists of (1) a piece of 0.5 mm diameter semi-rigid coaxial cable with a SMA jack at one end and an open at the other end and (2) a short piece of 50 μm diameter copper wire. The SMA jack at one end of the coaxial cable is threaded into a holder and held with a set screw. The SMA jack, which extends above the top of the

holder, accepts an SMA cable. The short piece of the 50 μm diameter wire is carefully soldered to the open end of the semi-rigid coaxial cable, which extends below the bottom of the holder. This short piece of wire is manipulated into a square loop which connects the center and outer conductor of the coaxial cable. The loop may be further manipulated such that the face of the loop is 100 μm across. Smaller probe loop faces are difficult to achiever due to the 50 μm diameter of the wire and the limitations of manual manipulation. Polystyrene covers the square loop to provide additional support for the loop. The probe assembly is accepted by the rotation stage described above. In this way the probe is positioned above the YIG sample. Greg Boll of Pico-Probe, a division of GGB Industries in Naples, Florida, is gratefully acknowledged for his assistance in the manufacture of the probe.

The overall configuration and basic operation of the IMP system is given here. The rider which holds the delay line is manually positioned between the pole pieces of the electromagnet. Once within the pole gap the sample is found with the video zoom system. Next, the probe is carefully lowered to just above the sample surface and the sample plane is carefully leveled to that of the scanning plane of the probe. Finally the probe is oriented such that the plane of the square loop is parallel to the microstrip transducer. When a microwave signal is applied to the delay line, the signal which propagates within the sample radiates from the sample surface. These fields, which are derived directly with the dynamic component of the magnetization, are probed by the loop through induction. The probe detection process is very similar to the detection of MSW signals with a microstrip transducer. In such a case, the resolution of the probe is approximately the inverse of the maximum detectable wavenumber given by Equation

(4.1). The 50 μm diameter of the wire used in the probe yields a resolution on the order of tens of microns. This resolution will be verified in Chapter 5. The signal at the output of the probe passes through an isolator. The isolator insures that a microwave signal does not reenter the probe through reflection. The probe signal then passes through a signal amplifier and is sent to the input of a signal analyzer.

Through signal measurements at different points on the sample, time and space resolved contours of the dynamic magnetization may be constructed. Only the relative amplitude of the dynamic magnetization may be gleaned from these contours. Through a LabView program it is possible to generate a three column array of positions and corresponding amplitudes necessary to generate such contours. This array can be plotted as a contour with a program written in Interactive Data Language 5.4.1. The IMP system may be used to measure full contours or to measure only data from individual points or lines along the sample.

The IMP system was used to perform linear and nonlinear measurements on MSW excitations. In Chapter 5 the linear measurements will be presented. In Chapter 7 measurements on solitons formed due to the induced modulation instability of co-propagating MSW excitations will be presented. A summary of the important microwave devices used in the measurement systems is given in Table 4.1.

Table 4.1. Table of microwave components used in the measurement systems.

Device	Manufacturer (Model Number)	Frequency Range
Microwave Source A	Hewlett-Packard (HP83623B)	50 MHz – 20 GHz
Microwave Source B	Hewlett-Packard (HP83650A)	50 MHz – 50 GHz
MTA (microwave transition analyzer)	Hewlett-Packard (HP71500A)	DC – 40 GHz
Oscilloscope	Hewlett-Packard (HP54845A)	DC – 1.5 GHz
Spectrum Analyzer	Hewlett-Packard (HP8593E)	9 kHz – 26.5 GHz
Amplifier	Narda/DBS (DBS0208N323)	2 – 8 GHz
Signal Amplifier	Lambda (T3-P037-005) (translated from Russian)	5 – 8 GHz
Variable Attenuator	Narda (786B)	3 – 8 GHz
30 dB Directional Coupler	Krytar (2618)	1.7 – 20 GHz
3 dB Directional Coupler	Arra (6-9200-2)	1 – 20 GHz
SMA Coaxial Cable	Midisco (Various)	DC – 40 GHz
Isolator	Midisco (M3I2080)	2 – 8 GHz
Tunnel Diode	Advanced Control Components (ACTP – 1555PC2)	2 – 8 GHz

CHAPTER 5

LINEAR RESPONSE OF YIG FILM WAVEGUIDES: IMP SYSTEM MEASUREMENTS

In this chapter, the linear MSW signal response of YIG film waveguides is measured and analyzed. This linear response is necessary for a meaningful interpretation of the nonlinear signal response to be presented in Chapters 6 and 7. These linear measurements were performed with the IMP system and the YIG film waveguides described in Chapter 4. Many of the results demonstrate unique capabilities of the IMP system.

Section 5.1 will present results on the linear signal response of a single MSBVW excitation in a 4.4 μm thick YIG film waveguide. The linear transmitted power and phase vs. frequency responses of the YIG film waveguide as measured by the probe will be compared to the delay line transducer response given in Chapter 4. In addition, the probe and transducer responses will be used to obtain the low power MSBVW dispersion ω vs. k for the 4.4 μm thick YIG film waveguide. Section 5.2 will deal with the linear signal response of two counter-propagating MSBVW excitations in a 4.4 μm thick YIG film waveguide. It will be shown that the analysis of such a configuration can be used as an alternative and more direct method for the measurement of the MSW dispersion. In addition, these results will demonstrate the probe spatial resolution. The MSW

dispersion characteristics obtained with this technique will be compared to those obtained in Section 5.1. In Section 5.3, the linear signal response of two co-propagating MSBVW excitations in a 4.4 μm thick YIG film waveguide will be considered. An analysis of this linear mode beating will demonstrate the time resolution of the IMP system. Section 5.4 will conclude this chapter with results on the linear MSW signal response of the 6.9 μm thick YIG film waveguide. This waveguide will be used in the nonlinear measurements presented in Chapters 6 and 7. In this section the IMP system will be used to obtain the linear MSW dispersion and loss parameters for MSBVW and MSSW excitations.

5.1 The Linear Response of a Single MSW Excitation

The linear transmitted power and phase vs. frequency responses of the YIG film waveguide, as measured by the IMP system, will be given in this section. These responses are indicative of the propagation of a single MSW excitation within a YIG film waveguide over a band of frequencies. This response will be compared to the delay line transducer response explained in Chapter 4. In addition, the probe and transducer responses will be used to obtain the low power MSW dispersion ω vs. k for the 4.4 μm thick YIG film waveguide. This technique will be referred to as the phase technique. From this comparison, it will be evident that, as expected, the probe essentially responds as a short element of grounded transducer.

Figure 5.1 shows linear transmitted power and phase vs. frequency characteristics and a low power MSW dispersion obtained from these characteristics. The delay line was oriented in the MSBVW configuration. The external magnetic field was about 1200 Oe. The graphs in the left column (a), labeled "transducer", show the transmitted power and phase vs. frequency response of the YIG film delay line transducers described in Chapter 4. These measurements were performed with the basic MSW delay line measurement system. The distance between the input and output transducers of the delay line was 0.9 cm. The graphs in the right column (b), labeled "probe", show the same response for the signal picked up by the probe of the IMP system from the YIG film surface. The distance between the probe and the input transducer of the delay line was 0.6 cm. The probe loop was oriented such that the probe loop face was parallel to the input transducer. Graph (c) shows the MSW dispersion obtained from the probe and transducer

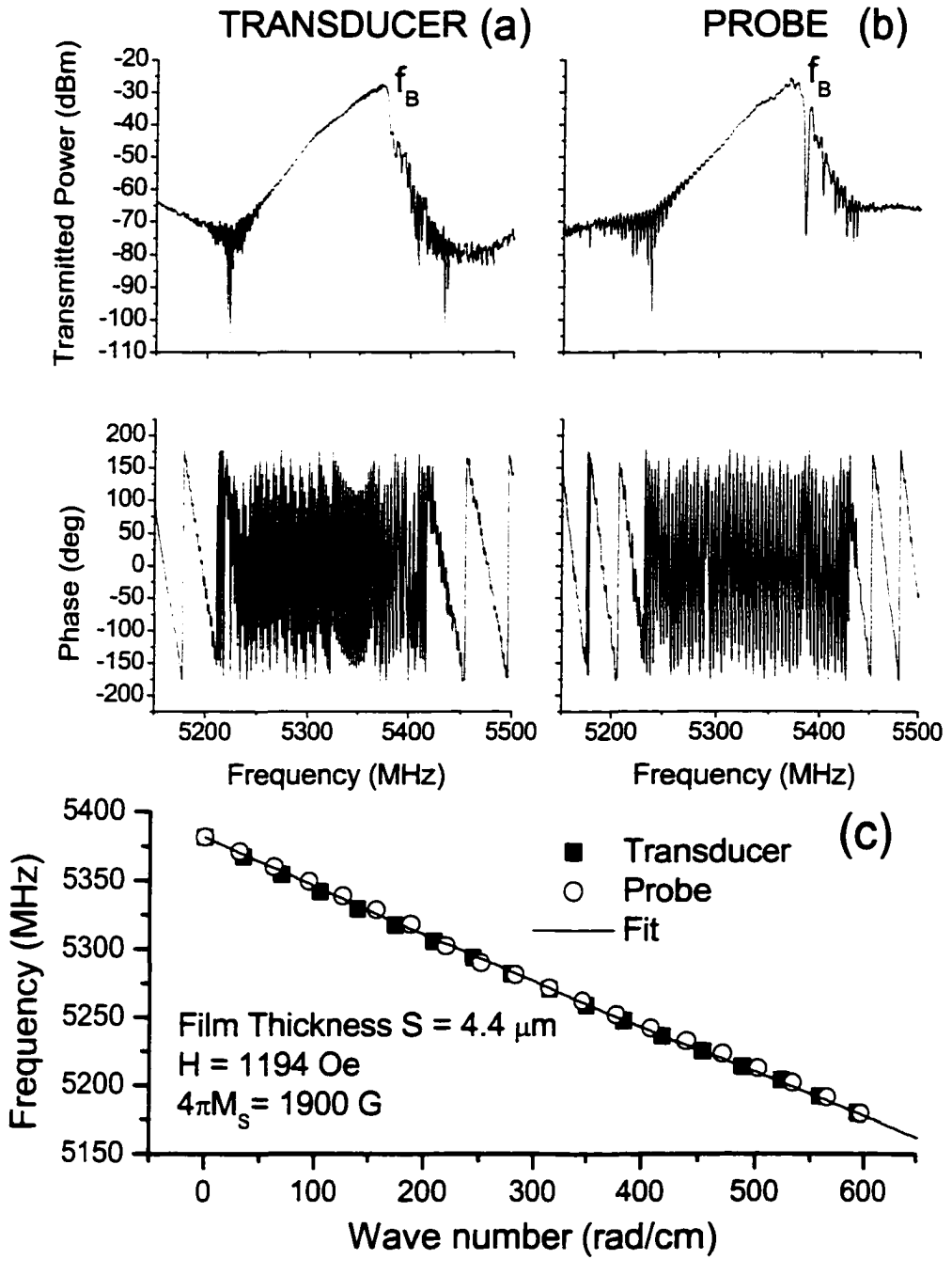

Figure 5.1. Graphs (a) and (b) show the transmitted power and phase vs. frequency characteristics for the probe and output transducer of the delay line. The measurements utilized a 4.4 μm thick YIG film in the MSBVW configuration. Graph (c) shows MSBVW dispersion characteristics constructed from the responses in (a) and (b). The data in (c) were fit to Equation (2.15) with the parameters given in the figure.

responses in (a) and (b).

Before an explanation of the method by which the MSW dispersion may be obtained from the characteristics in graphs (a) and (b), some comments about these responses will be made. As explained for the transducer response in Section 4.1, the transmitted power vs. frequency characteristic of both the probe and the transducer show minimum losses at approximately $k = 0$. These points are marked on both responses by $f_B = \omega_B / 2\pi$ and both occur at approximately 5382 MHz. It is important to note that the artifacts in the transmitted power vs. frequency characteristic which occur at frequencies above f_B are due to spurious MSSW excitations. If the probe is rotated from parallel to the transducers to perpendicular, the MSSW response in graph (a) increases and the MSBVW response decreases. In fact, this is the method by which the probe is oriented. When the low power MSBVW response is a maximum, and the MSSW response is a minimum, the probe is taken to be parallel to the transducer. Also note that, since the transducer separation distance is larger than the probe distance from the input transducer, the total phase change reflected in the probe phase characteristic is smaller than that of the transducer characteristic.

Measurement of the MSW dispersion through the transmitted power and phase vs. frequency characteristics is done in two steps. First, from the transmitted power vs. frequency characteristic, the frequency which corresponds to lowest excited wave number is estimated. For the case of MSBVW excitations this $k = 0$ excitation occurs at $f_B = \omega_B / 2\pi$. The value of f_B can be determined with an accuracy of about 5 MHz. Second, the frequencies and their corresponding wave numbers are determined from the phase vs. frequency characteristic through the relation $k_n L = 2\pi n$ where L is the

distance the MSBVW signal has traveled. A column of wave numbers k_n and frequencies f_n can be determined if it is assumed that $k_n L$ is the total phase. For the probe data, n = 0, 3, 6, 9... 57 and L = 0.9 cm were used. For the transducer data, n = 0, 5, 10, 15... 85 and L = 0.9 cm were used.

A plot of these wavenumbers and frequencies constitutes the dispersion of the MSBVW excitations and appears in graph (c) of Figure 5.1. The open circles show the probe data, while the solid squares show the transducer data. It is evident from the data in graph (c) that the MSBVW dispersion obtained from the probe and transducer responses coincide. This is quantitative evidence that the probe responds to the MSW signal within the YIG film waveguide in essentially the same manner as a grounded microstrip transducer. The solid line in (c) shows an excellent fit to the data through the use of Equation (2.15). The parameters used to perform the fit are a film thickness of $S = 4.4\,\mu\text{m}$, a saturation magnetization of $4\pi M_S = 1900\,\text{G}$, and an external magnetic field of $H = 1194\,\text{Oe}$. In the next section, the dispersion relations obtained from transmitted power vs. frequency responses of the transducers and probe will be compared to a direct measurement of the MSBVW dispersion which utilizes the scanning capability of the IMP system and two counter-propagating MSBVW excitations.

5.2 Linear Standing Wave Response of MSW Excitations

In this section, the linear signal response of two counter-propagating MSBVW excitations in a 4.4 μm thick YIG film waveguide as measured by the IMP system will be given. It will be shown that the analysis of the resultant standing wave pattern can be

used as a direct method for the measurement of the MSW dispersion. In addition, these results will demonstrate the probe spatial resolution. A comparison of the MSW dispersion characteristic obtained with this technique will be compared to the dispersion obtained in Section 5.1. The details of the experiments on, and the analysis of, these excitations will be given below.

A constant frequency, low power microwave signal is applied to both microstrip transducers of the delay line. The resultant counter-propagating MSW excitations set up a standing wave pattern. With the IMP system the signal strength at regular intervals along the sample width and length is measured. A contour, indicative of the standing wave pattern set up by the two counter propagating waves, may be generated from the data. The analysis of this contour allows one to directly determine the wavelength of the specific frequency applied. If one performs these measurements for a variety of frequencies within the MSW excitation band, it is possible to generate frequency and wavelength pairs. In this way, it is possible to measure directly the MSW dispersion. This technique will be referred to as the standing wave technique.

Figure 5.2 shows a set of four contours for different frequencies within the MSBVW excitation transmission vs. frequency band of the 4.4 μm thick sample shown in Figure 5.1. A small schematic of the counter-propagating wave configuration used to generate the contours is shown in the inset. Though ten contours were generated, only four representative scans are shown in Figure 5.1. The contours in (a) – (d) utilized MSBVW excitations at frequencies of 5371, 5365, 5338, and 5313 MHz, respectively. The frequencies of the excitations in (a) - (d) were 11, 17, 44, and 69 MHz from the band edge frequency, respectively. The distance between every third maxima gives the

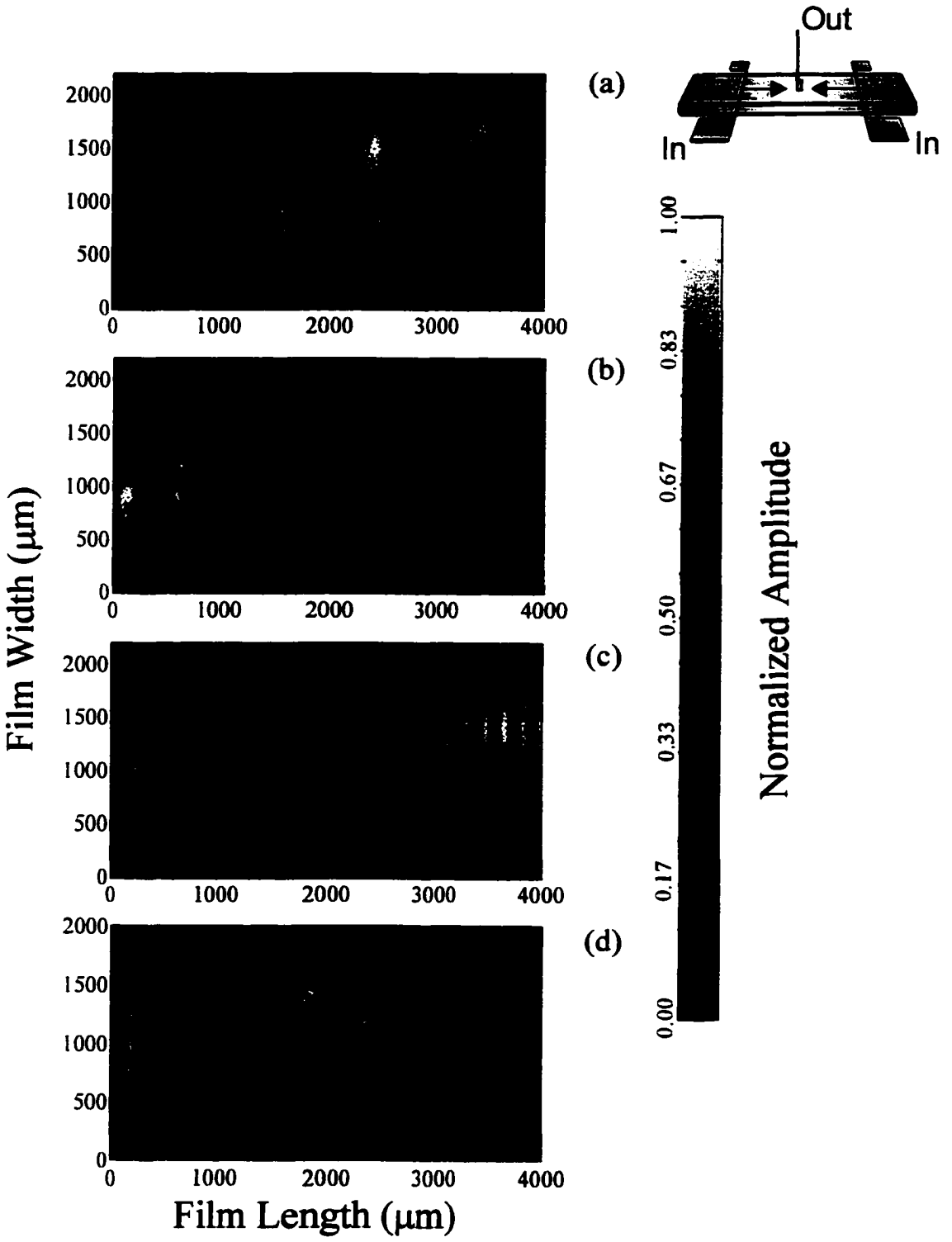

Figure 5.2. Four spatial contours of normalized amplitudes. The contours show standing wave patterns formed from two counter-propagating MSBVW excitations in a 4.4 μm thick YIG sample. The measured wavelengths in contours (a) - (d) were 2.025 mm, 1.414 mm, 0.515 mm, and 0.320 mm, respectively.

wavelength of the excitation mapped in the contours of Figure 5.2. The measured wavelengths for the contours in (a) – (d) were 2.025 mm, 1.414 mm, 0.515 mm, and 0.320 mm, respectively. Note that these wavelengths are in the range of MSW excitations and are not due to long wavelength EM waves in air. It is important to note that in Figure 5.2 (d) it is possible to easily resolve better than one eighth of a wavelength. This means that the spatial resolution of the probe is easily better than 40 μm in accordance with the tens of microns predicted by Equation (4.1). With the frequencies and wavenumbers known, it is possible to use the above contours to plot the dispersion and compare it to the phase technique results.

Figure 5.3 shows the results of the dispersion characteristics from the phase and standing wave techniques. The open circles and solid squares, as well as the solid line fit, are the same as in Figure 5.1. The crosses represent the dispersion results from the standing wave technique. The agreement between the different techniques, as well as the theory, is excellent. Due to this result, the assertion that the probe responds to the MSW signal within the film essentially as a grounded microstrip transducer is supported.

In practice, both the phase and standing wave techniques are used to measure the sample dispersion. Usually the dispersion is measured, first, through the phase technique. Then, the results of the phase technique are checked against the standing wave technique results for a few particular frequency-wavenumber pairs. In this way the dispersion can be measured with high accuracy. With these dispersion characteristics, it is possible to know the wavenumber of the MSW excitation in the experiment.

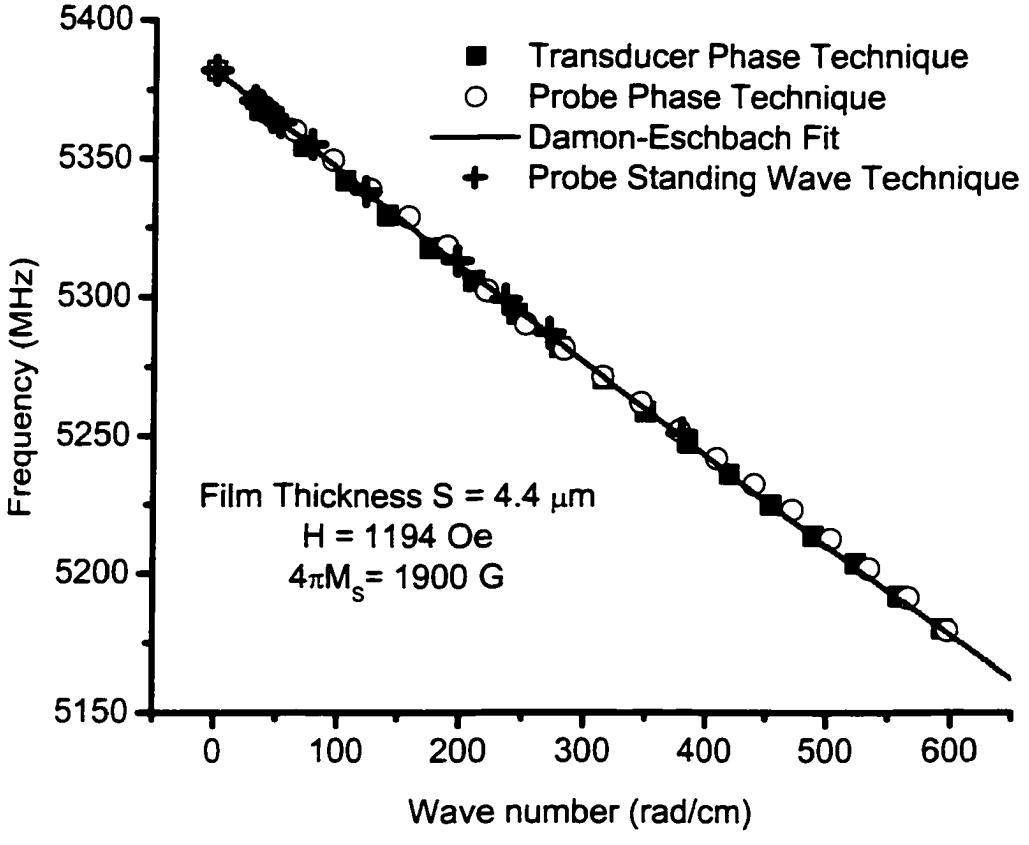

Figure 5.3. Graph of the measured and calculated frequency vs. wavenumber for MSBVW excitations in a 4.4 μm thick YIG film waveguide. The solid squares, open circles, and solid line are from Figure 5.1. The crosses are the data points obtained from the probe using the standing wave technique.

5.3 Linear Mode Beating Response of MSW Excitations

In this section the linear signal response of two co-propagating MSBVW excitations in a 4.4 μm thick YIG film waveguide as measured by the IMP system will be given. The linear mode beating spatial response measured by the IMP system will be compared to the theoretically expected response. In addition, these results will demonstrate the time resolved capability of the IMP system. For the IMP system the signal analyzers determine the *value* of the time resolution. In the case of time resolved measurements the signal analyzer to be used is the HP Infiniium oscilloscope. The time resolution of this signal analyzer is determined approximately by the one nanosecond rise time of the tunnel diode used at its input. The ability to perform the time resolved measurements with the IMP system is important to the results in Section 7.1.

The ability to perform time resolved measurements with the IMP system relies heavily on (1) the stable synchronization of the microwave sources and (2) the proper triggering of the HP Infiniium oscilloscope described in Section 4.3. The configuration used to achieve this synchronization and triggering is explained in Chapter 4. The five key devices used in the synchronization and triggering are: (1) the HP Infiniium oscilloscope, (2) the two HP synthesized sweepers, (3) the HP programmable pulse generator, and (4) the HP MTA. A description of these devices can be found in Chapter 4. Here a brief review of the configuration of these five devices is given.

A schematic representation of the configuration of the experimental setup can be found in Figure 5.4 (a). Microwave source B is externally referenced to source A. In addition, source A is controlled by the MTA, not shown in the inset, through a GPIB

connection and a 20 MHz synchronization input. The programmable pulse generator is also controlled by the MTA through another GPIB connection and the same 20 MHz synchronization input. Therefore, through the MTA, it is possible to synchronize the microwave sources to the pulse generator such that at the leading edge of each pulse from the pulse generator the signals from the sources begin with a constant phase angle. The pulse from the pulse generator is sent to the oscilloscope as a trigger signal. The microwave signal from the probe is sent to another channel of the oscilloscope which, in this configuration, is sensitive to phase changes in the probe signal.

Figure 5.4 (b) shows two power vs. time profiles. The profiles in Figure 5.4 (b) are the power vs. time signals from the surface of the film picked up by the probe at two different positions. These signals are the power envelopes of the two co-propagating MSBVW signals. The two microwave signals applied to the input of the delay line, from sources A and B, had frequencies of 5377 MHz and 5347 MHz, respectively. These frequencies are very close to the band edge frequency of 5382 MHz. The difference between the frequencies was 30 MHz. This corresponds to the envelope of an interference pattern with a period of 33.3 ns. This is reflected in Figure 5.4 (b). It is important to note that without the trigger pulse and the stable synchronization of the sources and the pulse generator, the microwave power envelopes shown in Figure 5.3 (b) would be unstable.

The upper trace in Figure 5.4 (b) was picked up by the probe at a distance of 2 mm from the input antenna of the delay line. The lower trace was picked up at a distance of 4 mm from the input of the delay line. Note first the attenuation the signal has suffered between the two measurement points. Second, note that a phase shift has occurred

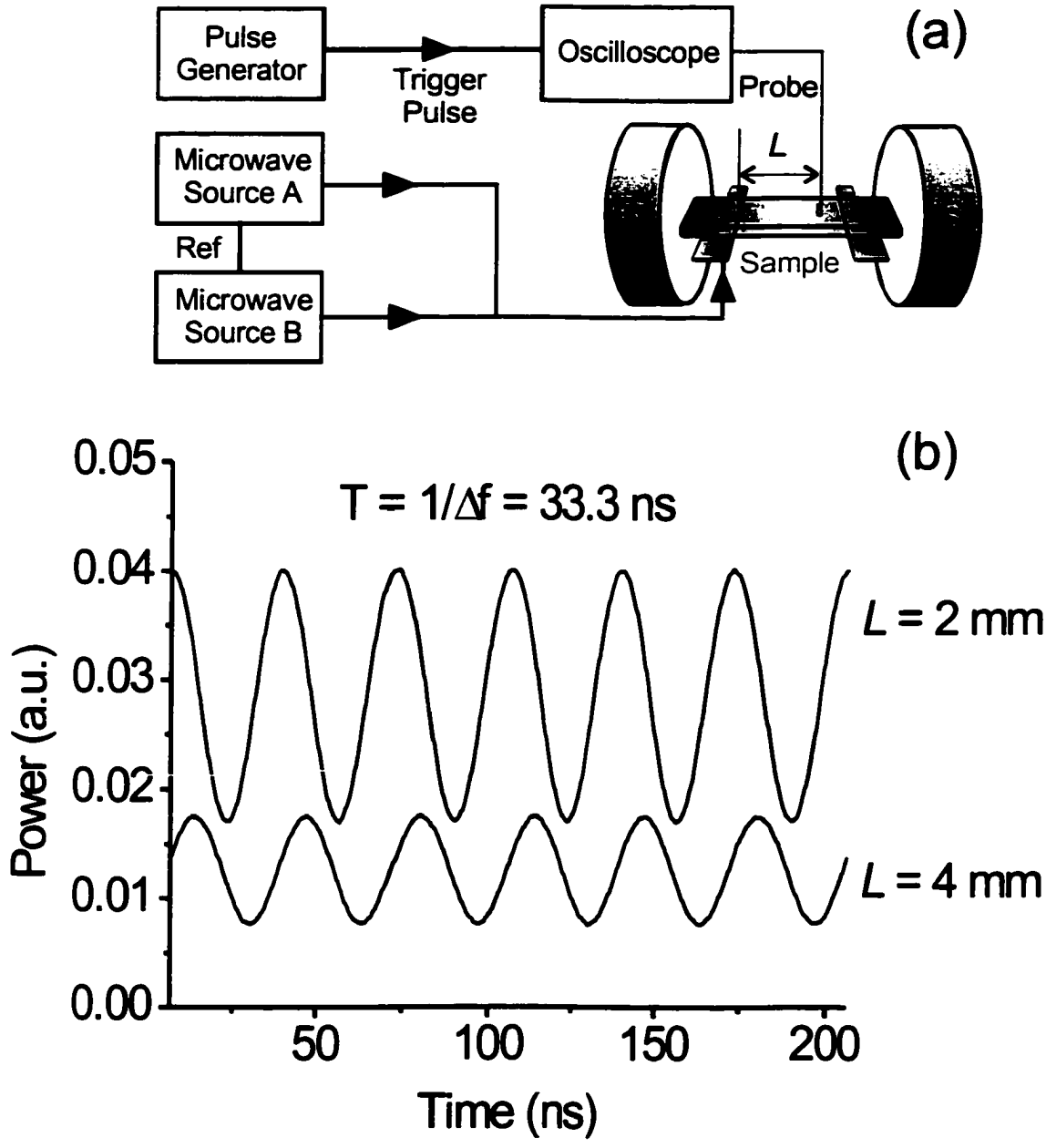

Figure 5.4. Schematic of the experimental configuration for time resolved measurements and representative power vs. time profiles. The schematic in (a) shows the IMP system configuration. The data in (b) shows two representative microwave signals. The signals are the result of two co-propagating MSBVW excitations with different frequencies. The frequency difference was 30 MHz. The upper and lower traces were acquired by the probe at a distance of 2 and 4 mm from the input of the YIG film delay line, respectively.

between the two points. This phase shift is only measurable due to the complex synchronization of the experimental apparatus outlined above. It is precisely this phase shift that will be utilized for the performance of the time resolved measurements.

The goal of the time resolved measurement is to be able to measure the spatial distribution of the magnetization for a constant value of time. These measurements are performed in a way very similar to the space resolved measurements described in Section 5.2 except that the signal strengths, detected at regular intervals along the sample width and length, are obtained for a constant value of time. As was demonstrated by the two traces in Figure 5.4 (b), the value of the power at some fixed value of time will change due to both the attenuation of the signal and the phase shift of the signal between the individual measurement points.

Figure 5.5 shows the results of a time resolved measurement in the form of a contour of normalized powers. The parameters of the measurement are the same as in Figure 5.4 above. The contour shows both the phase shifts and attenuation mentioned above. The main result of this contour is the demonstration of time resolved capability of the IMP system.

A comparison between the period of the waveform in the time and space domains demonstrates quantitatively the time resolved capability of the IMP system. As mentioned above, the period of the waveform in the time domain is 33.3 ns. The measured period of the waveform in the space domain with the contour was approximately 0.0800 cm. This period was measured between the maxima at 3 mm and 5 mm. It is possible to compare these two results through the use of the previously obtained group velocity. The spatial period Γ should be $\Gamma = Tv_g$, where T is the period

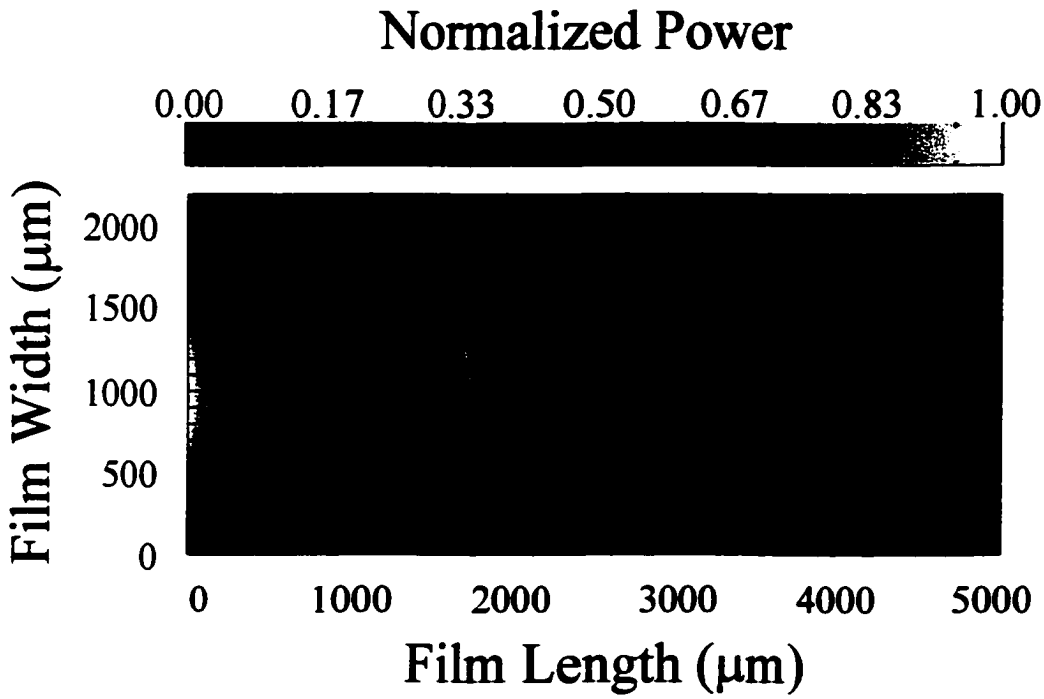

Figure 5.5. Spatial contour of normalized powers which demonstrates the time resolved capability of the IMP system. This contour was generated with the IMP system and two co-propagating MSBVW signals with frequencies separated by 30 MHz. These MSBVW signals are the same as those in Figure 5.4. This contour shows a spatial period of approximately 0.08 cm. This is in good agreement with the spatial period predicted from the temporal period.

in the time domain equal to 33.3 ns and v_g is group velocity previously obtained dispersion relation for the 4.4 μm thick YIG sample. The low wavenumber group velocity obtained from the Equation (3.19) is $v_g \cong -2.28\times10^6$ cm/s. This group velocity yields a spatial period $\Gamma = 0.0760\,\text{cm}$. The error between the measured and predicted values is approximately 5 %. This demonstrates the time resolved capability of the IMP system. This time resolved capability will be used in Chapter 7.

5.4 Linear Loss and Dispersion of a 6.9 Micron Thick YIG Film Waveguide

The measurements in Sections 5.1 – 5.3 utilized the 4.4 μm thick YIG film waveguide. However, in the nonlinear measurements in Chapters 6 and 7, the 6.9 μm thick YIG film waveguide will be used. In this section the linear dispersion and loss parameters for MSSW and MSBVW excitations will be measured with the help of the IMP system. First, the sample dispersion results will be presented, followed by loss parameter results. The results on the MSSW and MSBVW dispersion will be useful for the presentation of the results in Chapters 6 and 7. The results on the sample loss demonstrate another capability of the IMP. The sample loss also relates to the minimum modulation frequency expected for MSW excitations presented in Chapter 3.

Figure 5.6 shows the obtained MSSW and MSBVW dispersion characteristics. The solid squares are the experimental points determined from the probe transmitted power and phase vs. frequency responses outlined in Section 5.1. The probe was 0.7 cm from the input transducer of the YIG film delay line. The upper curve shows the MSSW dispersion, while the lower curve shows the MSBVW dispersion. The lines represent fits

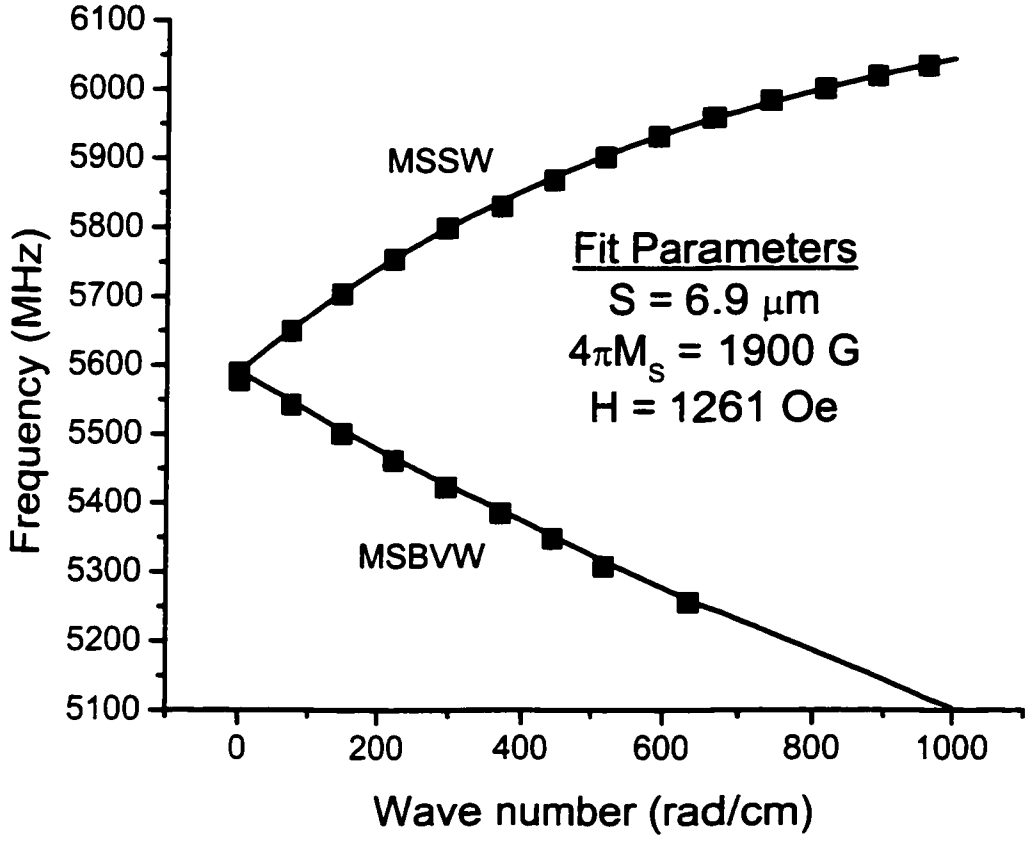

Figure 5.6. Graph of the measured and calculated frequency vs. wavenumber for MSW excitations in the 6.9 μm thick YIG film waveguide. The solid squares are the data points obtained through the probe phase technique. The solid line indicates the calculated frequency vs. wave number characteristic. The calculated curve utilized Equations (2.15) and (2.17). The parameters are given in the figure.

to the data through Equations (2.13) and (2.15) for the MSSW and MSBVW dispersions, respectively. These dispersion characteristics were checked directly with the probe with the standing wave technique, described in Section 5.2, for four particular wave number-frequency pairs. In this way the dispersion was obtained with very high accuracy. These graphs will be useful for the determination of the wave number of a particular excitation in the results of Chapters 6 and 7.

Note that the curvature of the MSSW dispersion is higher than that of the MSBVW dispersion. This indicates that the group velocity and dispersion coefficient of MSSW excitations is higher than that of MSBVW excitations. The value of the group velocity at $k \to 0$ obtained from the data in Figure 5.6 is approximately $v_g \cong 5.5 \times 10^6$ cm/s and $v_g \cong -3.6 \times 10^6$ cm/s for the MSSW and MSBVW excitations, respectively. In addition, note that the MSSW dispersion includes wave number data points up to $k = 950$ rad/cm while the MSBVW dispersion includes wave number data points up to only $k = 650$ rad/cm. Since the attenuation of MSBVW excitations over a fixed distance is greater than that for MSSW excitations, the band of detectable wave numbers is smaller for MSBVW excitations.

Consider now the fits to the data represented by the solid lines in the graphs. Equations (2.13) and (2.15) were used to fit the MSSW and MSBVW data, respectively. It was possible to fit both sets of data with the same parameters. The parameters are given in Figure 5.6 and are as follows: film thickness $S = 6.9\,\mu$m, external magnetic field $H = 1261$ Oe, and saturation magnetization $4\pi M_S = 1900$ G. The values of the group velocity determined with these parameters and Equations (3.16) and (3.17) are

$v_g = 5.49 \times 10^6$ cm/s and $v_g = -3.64 \times 10^6$ cm/s for the MSSW and MSBVW excitations, respectively. This is in good agreement with the experiment.

Turn now to the determination of the sample losses. The IMP measurement system was critical to the accuracy of these measurements. A schematic representation of the probe-sample geometry is shown in the inset of Figure 5.7. In order to obtain the sample loss, a pair of output power P_{out} vs. input power P_{in} curves for both MSSW and MSBVW excitations were measured by the probe. These curves are shown in Figure 5.7. Graph (a) shows the results for MSSW excitations while graph (b) shows the results for MSBVW excitations. The frequencies of the excitations used in Figure 5.7 were chosen near the maximum of the transmission characteristic for both MSSW and MSBVW excitations. This frequency value was nominally 5590 MHz in both cases. The curves in graphs (a) and (b) were measured with the probe at a distance d of 4 mm and 8 mm from the input microstrip transducer. The curves are labeled with the appropriate distances in the figure. The analysis of these curves allows one to recover the sample loss.

In order to obtain the loss parameter from the curves in Figure 5.7 the dependence of the output power on the input power for two particular distances must be known. As alluded to at the end of Section 2.2, the connection between the input and output power may be written as

$$\begin{aligned} P_{out}^{(1)} &= AP_{in} \exp(-2k_r^{MSW} d^{(1)}) \\ P_{out}^{(2)} &= AP_{in} \exp(-2k_r^{MSW} d^{(2)}) \end{aligned} . \tag{5.1}$$

In Equations (5.1) the superscripts (1) and (2) denote the curves obtained at distances of 4 and 8 mm, respectively. Also in Equations (5.1), k_r^{MSW} is the inverse of the effective decay length of the MSW excitation. The coefficient A in Equations (5.1) is

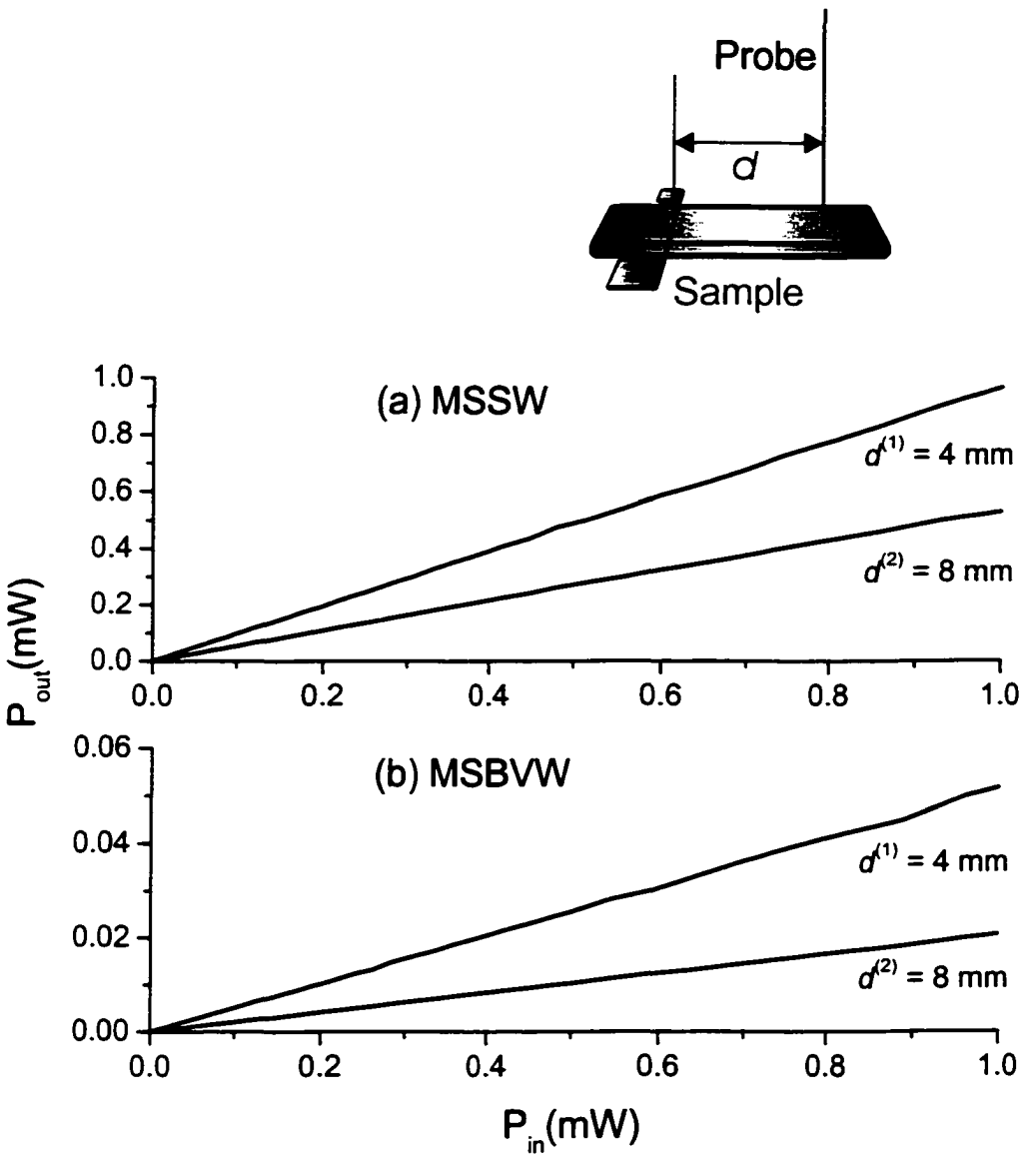

Figure 5.7. Output power vs. input power curves. The curves in (a) and (b) were obtained for MSSW and MSBVW excitations, respectively. The upper and lower curves in each graph were obtained at distances of 4 and 8 mm, respectively. Both curves were obtained at a nominal frequency of 5590 MHz, near the point of maximum transmitted power. These curves will be used to obtain the losses for the sample.

representative of other loss sources, independent of distance and power, such as excitation efficiency and reflection loss. A simple manipulation of Equations (5.1) yields

$$k_r^{MSW} = \frac{\ln(P_{out}^{(2)}/P_{out}^{(1)})}{2L}, \tag{5.2}$$

where $L = d^{(2)} - d^{(1)}$. It is evident from Equation (5.2) that one may easily obtain k_r^{MSW} and therefore Z_r^{MSW} for both MSSW and MSBVW excitations from the data in Figure 5.7. Through the use of Equation (2.11), $\Delta H = 2|v_g|/(Z_r|\gamma|)$, it is possible to obtain a linewidth parameter ΔH. Since the curves in Figure 5.7 were obtained very near $k = 0$ the value of the group velocity v_g in Equation (2.11) will be approximated to values given earlier in this section. For MSSW and MSBVW excitations these values are $v_g = 5.49 \times 10^6$ cm/s and $v_g = -3.64 \times 10^6$ cm/s, respectively. With these group velocity values, it is possible to obtain the linewidth parameters.

The results of this calculation are shown in Figure 5.8. The open squares show the results for MSBVW excitations. The solid squares show the results for MSSW excitations. The average value of the linewidths for MSSW and MSBVW excitations is given by $\Delta H = 0.46 \pm 0.01$Oe. This value of ΔH was used in Equation (3.15) to estimate the minimum modulational instability frequency. At these low frequencies, a linewidth value of 0.46 Oe is somewhat large for single crystal YIG. One would expect a value of approximately 0.3 Oe. This can be attributed to the influence of the dielectric substrate of the YIG film waveguide as well as the waveguide edges which may introduce additional losses.

The relevant linear and nonlinear theory of MSW excitations has been outlined. In addition, the measurement systems have been described in detail and the linear MSW

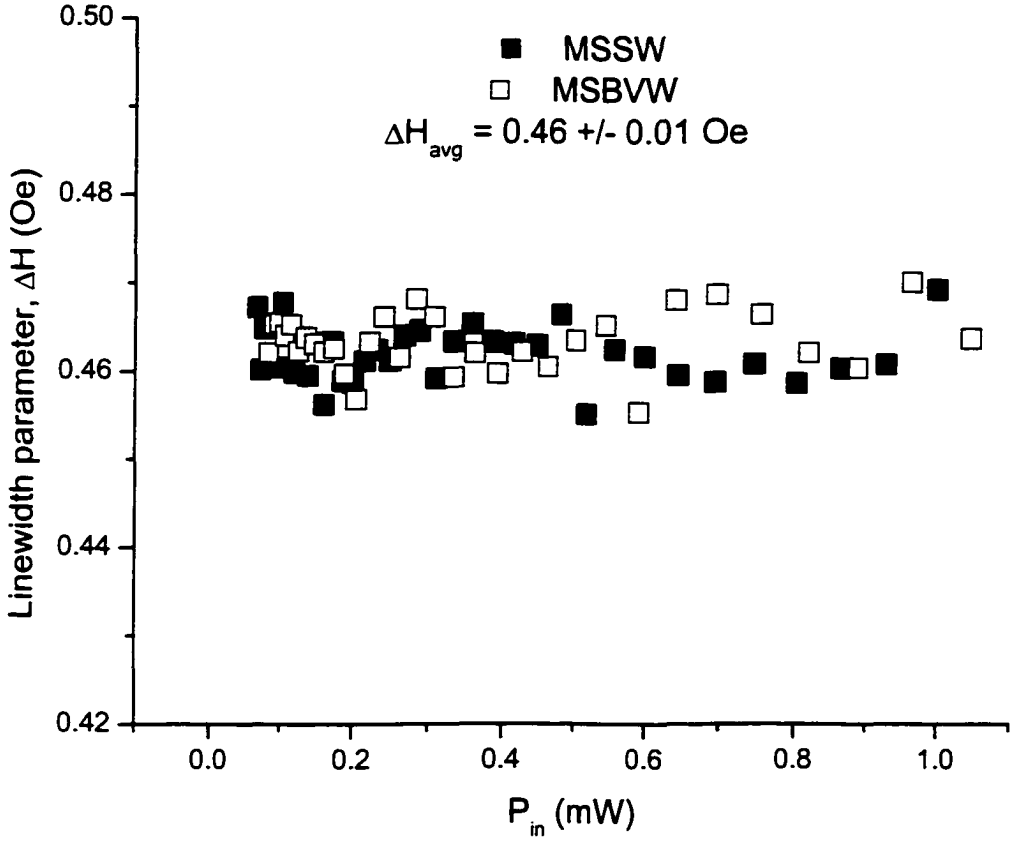

Figure 5.8. Linewidth parameter vs. input power graphs calculated from the data in Figure 5.7. The open squares show the results for MSBVW excitations. The solid squares show the results for MSSW excitations. The average linewidth is given by $\Delta H = 0.46 \pm 0.01 \text{Oe}$.

signal response of the YIG film waveguide to be used has been measured. With this background established, the nonlinear MSW signal response of 6.9 μm thick YIG film waveguide will be addressed. In Chapters 6 and 7 to follow, the measurements on the induced modulational instability of MSW excitations and SWE solitons will be presented.

CHAPTER 6

THE SELF GENERATION OF SWE SOLITONS IN FREQUENCY FILTERED ACTIVE RESONANT RINGS

This chapter presents results on the self generation of SWE solitons in a frequency filtered ARR structure. As outlined in Chapter 4, an ARR consists primarily of a YIG film delay line and a microwave power amplifier connected in a feedback loop. For high ARR gains, a nonlinear microwave signal oscillates in the ring. Through the adjustment of the nonlinear and dispersive characteristics of the ring, trains of microwave SWE solitons may be self generated. At these high ring gains, the modulational instability of the comb of filtered resonance frequencies, combined with the attractive or repulsive nonlinearity of the MSW excitations, may yield trains of SWE solitons.

Previous experiments on the self generation of SWE solitons in an ARR structure utilized a technique known as synchronized time gating [6, 7]. For this technique, a periodic interruption of the ring feedback, through the use of switching elements, allowed for the generation of both bright [6] and dark [7] soliton trains. The interruption was necessary to self generate *stable* trains of soliton pulses. Here, results on the stable self generation of SWE soliton trains through the use of a new frequency filtering technique for an ARR structure, which utilizes no switching elements, is presented.

For the frequency filtering technique, the transmitted power vs. frequency

characteristic of the delay line in the ring is matched to the power vs. frequency spectrum of a single soliton from the desired train of pulses. This matching controls the number and relative amplitude of the ring resonant frequencies self generated at high gain. The frequency spectra matching, combined with the proper adjustment of the nonlinear and dispersive characteristics of the ring, allows for the stable self generation of SWE solitons. The frequency filtering of the ring eliminates the need for periodic interruption and greatly simplifies the self generation technique.

Envelope bright and dark solitons were self generated in frequency filtered ARR structures which utilized the 6.9 μm thick YIG film. It should be noted that this new technique allowed for the first excitation of single black solitons in ferrite films. Due to their novelty, the results for dark MSSW solitons will appear first in Section 6.1. The results for bright MSBVW solitons will appear in Section 6.2. The amplitude or power and phase vs. time profiles, together with the power vs. frequency spectra, of the self generated microwave pulses support their envelope soliton nature.

6.1 Dark Soliton Self Generation in a Frequency Filtered Active Resonant Ring

This section presents results on the self generation of SWE dark solitons in a frequency filtered ARR structure. The main body of experimental results on trains of envelope dark solitons in solid state media has been for optical solitons in fibers and SWE solitons in ferrite films. A considerable amount of the work on optical dark soliton trains is reviewed by Taylor [3]. Recently, SWE dark soliton trains have been observed in active resonant rings through the use of synchronized time gating [7]. As described in Chapter 3, dark envelope solitons are robust, narrow, nonlinear pulses which have a nonzero phase jump across their width. The time gating technique of Reference 7 utilizes switching elements in the ring as described earlier. However, due to the phase constraints introduced by the periodic interruption in the ring, only black soliton *pairs* were excited [8]. The single fundamental SWE black soliton has, therefore, not been observed.

Through the use of a frequency filtered ARR structure, which requires no switching elements, the self generation of SWE black and gray single soliton pulse trains from MSSW excitations has been observed. The two key differences between the frequency filtered ARR experiments and those which utilize synchronized time gating [6, 7] are (1) the u-shaped microstrip transducers used in the MSW delay line and (2) the absence of any switching elements in the ARR structure. A schematic representation of the frequency filtered ARR structure and a description of its operation are given in Chapter 4. For the experiments presented here, the separation between the two elements of the u-shaped transducer was $d = 0.26$ mm. The separation between the two antennas was $L = 2$

mm. The bandwidth of the microwave amplifier in the ring was greater than 5 GHz with a 30 dB dynamic range and a high peak power. These amplifier characteristics ensured that the nonlinear response of the ring was determined solely by the MSSW excitations in the YIG film. The experimental data discussed below were obtained for a nominal external magnetic field $H = 970$ Oe and a film thickness $S = 6.9$ μm.

The self generation of SWE dark solitons was performed in three steps. First, the transmitted power vs. frequency profile for the MSSW YIG film delay line was measured. For this measurement a low power microwave signal was applied to the ring. These data were used to confirm the desired frequency position and shape of the delay line pass band. Second, additional transmitted power vs. frequency profiles were obtained for the entire ring structure with different values of the ring gain. These data were used to confirm the frequency positions of the ring resonances and determine the change in the response as a function of the gain. Third, the external source was disconnected and the gain was increased above the linear oscillation regime. In this regime, a train of narrow dark microwave pulses was measured at the output of the ring. The power and phase vs. time profiles, along with the power vs. frequency spectrum, were used to confirm the soliton nature of the output pulses. Fine adjustments in the external magnetic field served to shift the power vs. frequency response of the ring which allowed for the observation of black and gray soliton trains.

Figure 6.1 shows three output power vs. frequency profiles which are related to steps one and two above. Graph (a) shows the response of the ARR delay line in the absence of feedback. The response in (a) is that of the u-shaped transducer YIG film delay line. The inset of graph (a) shows a small schematic of the delay line which corresponds to the

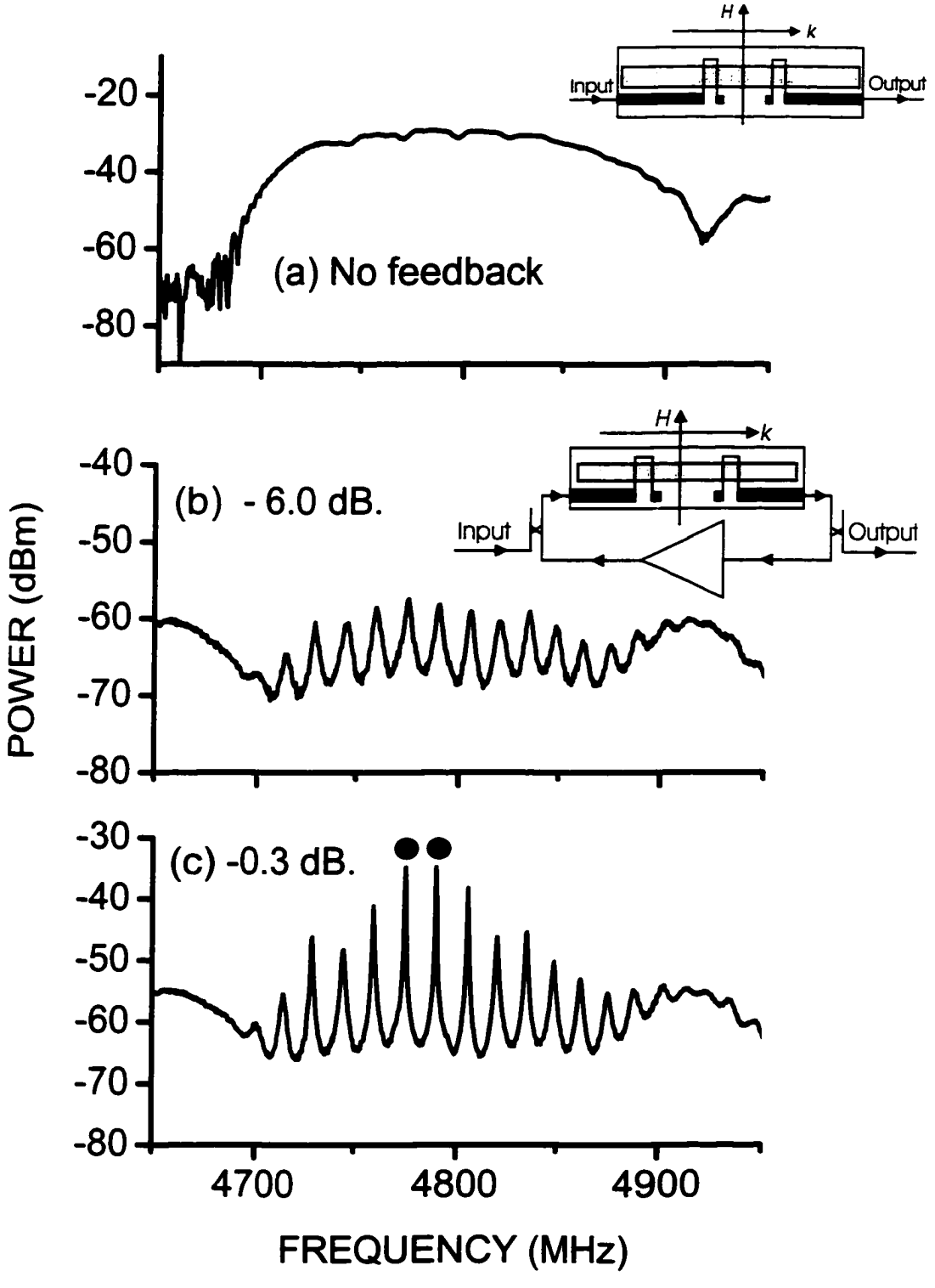

Figure 6.1. Low power frequency characteristics of the MSSW YIG film structure and resonant ring. The applicable ring gains in dB are indicated. The black dots in (c) identify the two largest ring resonance spikes.

arrangement in step one. Graphs (b) and (c) show step two where the effect of feedback on the response in (a) is observed. A simple schematic of the step two configuration is shown in the inset of graph (b).

In the case of (a), a low level input microwave power of approximately -20 dBm was applied to the MSSW delay line. The profile in (a) is typical of the delay line response for MSSW excitations, but with a reduced bandwidth and a smoother shape due to the two element transducer response as explained in Chapter 4. As described in Chapter 4, the standard pass band was modified to match the expected width of the desired single soliton power frequency spectrum. This was done in order to suppress spurious oscillations and enhance the conditions for stable soliton formation. The MSSW pass band in (a) extends from approximately 4670 MHz to 4920 MHz. The high frequency limit corresponds to a maximum wave number obtained from the MSSW dispersion given by Equation (2.13) of $k_{max} \approx 300\,\text{rad/cm}$. The parameters used in Equation (2.13) were S = 6.9 μm, $4\pi M_s = 1900\,\text{G}$, and $H = 969\,\text{Oe}$. This k_{max} is in reasonable agreement with the value obtained from Equation (4.3) $k_{max} \sim 2\pi/d \approx 250\,\text{rad/cm}$ for the u-shaped transducer, where d is the separation between the elements of the transducer.

The responses in graphs (b) and (c) are for a low power microwave signal applied to the frequency filtered ARR structure at different values of gain. The approximate ring gains are indicated in graphs (b) and (c). The zero dB gain point, shown approximately in (c), was determined experimentally as the linear self oscillation threshold of the ARR structure. The spikes in (b) and (c) of Figure 6.1 correspond to the resonant frequencies of the ring. At these spike points, the phase matching condition $k_n L + \phi_e = 2\pi n$ given by Equation (4.2) is satisfied. The spike spacing is approximately 14.6 MHz. The envelope

of these spikes is the u-shaped transducer response in (a). The two spikes in (c), denoted by the black circles, at 4778 MHz and 4792 MHz are near the peak transmission point in the pass band and have approximately equal amplitudes. When the external source is disconnected and the gain is increased to the 0 dB point, these frequencies will self oscillate and dominate the linear response. In the nonlinear self oscillation regime, at gains well above 0 dB, these equal amplitude frequencies provide the seed response for the formation of black solitons.

Small changes in the external magnetic field can serve to shift the relative position of the comb of spikes in Figure 6.1 (c) relative to the pass band of the delay line in (a). Such field changes can be used to slightly offset the power levels of the dominant spikes at 4778 MHz and 4792 MHz. In the nonlinear self oscillation regime, similar to the black soliton case, these frequencies provide the seed response for gray solitons. The seed response determined by the levels of the dominant spikes indicated in (c), combined with the induced modulational instability and repulsive nonlinearity of the MSSW signals, lead to the formation of black and gray soliton trains.

In order to understand the physical mechanisms at work here, consider the linear response of two equal amplitude co-propagating waves with different frequencies f_1 and f_2 as discussed in Chapters 3 and 5. The combination of these signals yields a nonzero background with dips to zero amplitude at the beat points. The period T of this waveform is $1/|f_1 - f_2|$. There is also a carrier phase jump of 180° across each dip. The pulse sequence produced by the interference of these two signals, therefore, can provide the seed response for a train of single black solitons. As indicated above, small changes in the field could cause a slight imbalance in these two equal amplitude signals. One still

obtains dips at the repetition period T, however, the dips do not go to zero amplitude and the phase jumps across the dips are less than 180°. This is the seed response for gray solitons.

The procedure outlined above was used to produce both black and gray fundamental dark solitons. For black solitons, the structure was first configured to produce the response shown in Figure 6.1 (c) with the two largest ring resonance spikes at equal amplitude. Next the microwave source was switched off and the gain was then increased to the point needed to (1) produce a self generated microwave response in the ring and (2) allow the nonlinear process to develop. The result was a narrowing of the envelope response to yield the cusp like dips characteristic of dark solitons.

Figure 6.2 shows representative black soliton results. These data were obtained for a ring gain of +0.5 dB and the other conditions specified above. Except for the phase data, these results are representative of data obtained with no microwave input signal. A low level microwave reference at 4785 MHz was used for the phase measurements. The power level for this reference signal was 35 dB below the power levels of the self generated frequency harmonics in the ring. Care was taken to ensure that this reference did not affect the ring signal response. The top four graphs show the experimental black soliton amplitude and phase profiles, respectively. The bottom graph shows the power frequency spectrum for the measured signal.

The signal characteristics for these data match those expected for single black solitons. The cusps in (a) and (a-e) are sharp and distinct, and fall precisely to zero at the pulse center. The data in (b) and (b-e) also show the 180° jumps in phase across the dips. The power spectrum in (c) shows multiple harmonics over a band width which is slightly

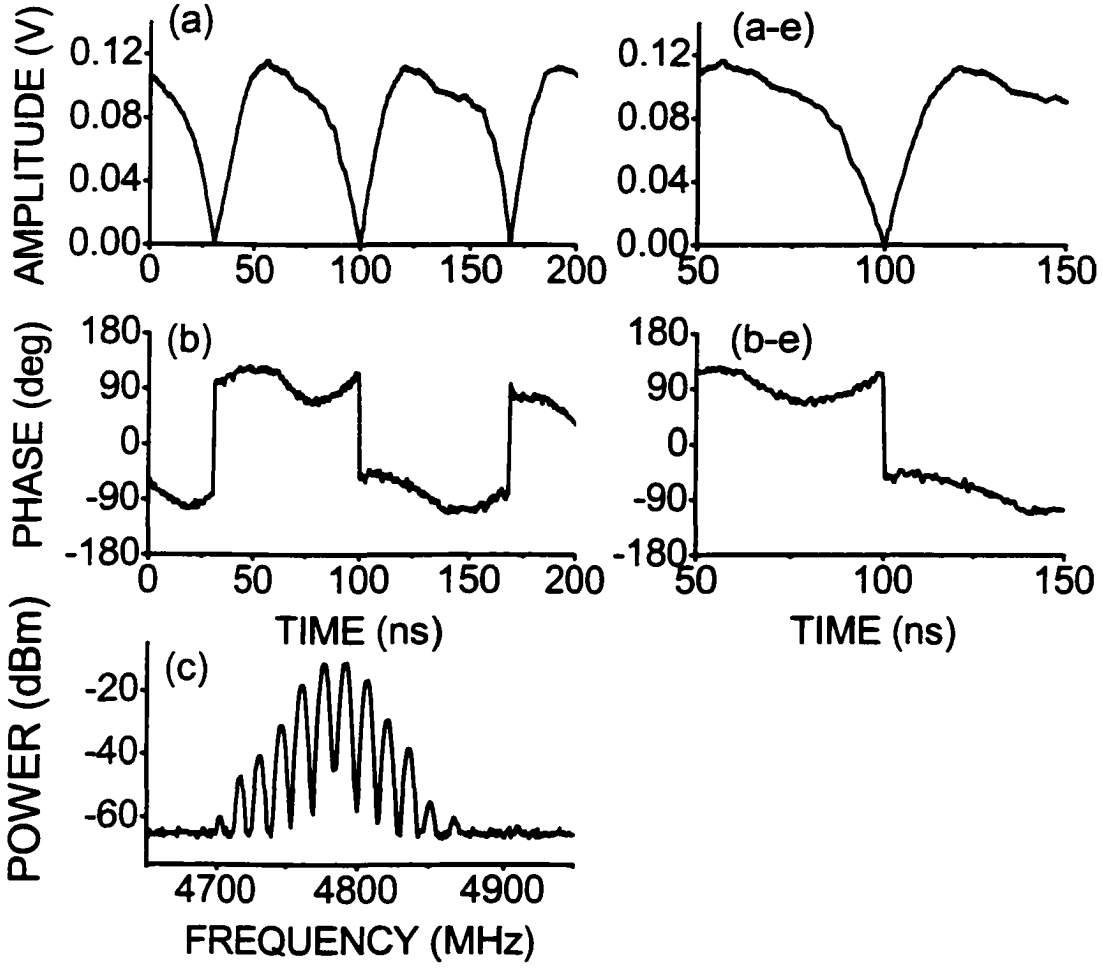

Figure 6.2. Fundamental black soliton pulse train characteristics. Graphs (a) and (b) show the microwave voltage and phase profiles, respectively, for the self generated signal in the ring structure with a ring gain of +0.5 dB. Graphs (a-e) and (b-e) show the same signals as in (a) and (b) but on an expanded time scale. Graph (c) shows the corresponding power vs. frequency spectrum of the ring signal.

narrower than the pass band in Figure 6.1 (a). Note that the two primary peaks in (c) have equal amplitudes. Note also that the self generated black soliton sequence has a power frequency spectrum with peaks which coincide with the cw resonance frequencies of the ring shown in Figure 6.1 (c). The 14.6 MHz spacing in the frequency peaks corresponds to a repetition period of 68.5 ns. This value matches the observed repetition period for the black soliton train in (a) and (b).

It should be emphasized that these signals consist of trains of single black solitons, not the double cusp dips which have been previously reported for *pairs* of black solitons [7, 8]. It should also be emphasized that these stable soliton signals were obtained with no external microwave signal applied to the ring. These single black solitons were self generated solely through the nonlinear feedback process within the ring.

Figure 6.3 shows representative data on the self generation of gray soliton trains. The conditions were the same as for the data in Figure 6.2, except that the static magnetic field H was reduced from 970 Oe to 968 Oe. This small change served to slightly imbalance the amplitudes of the two dominant spikes in the power spectrum of Figure 6.2 (c). This imbalance yielded the seed signals needed for gray soliton generation. The format for Figure 6.3 is the same as for Figure 6.2.

The gray soliton data show different characteristics compared to the black soliton data in Figure 6.2. (1) The dips in amplitude do not go to zero. (2) The dips are more rounded and less cusp like. (3) The phase changes around each dip are no longer abrupt. (4) The overall phase change associated with a given dip is smaller than 180°. (5) The two main peaks in the power spectrum show a slight imbalance. The features shown in Figure 6.3 are representative of gray solitons. The particular data in Figure 6.3 show

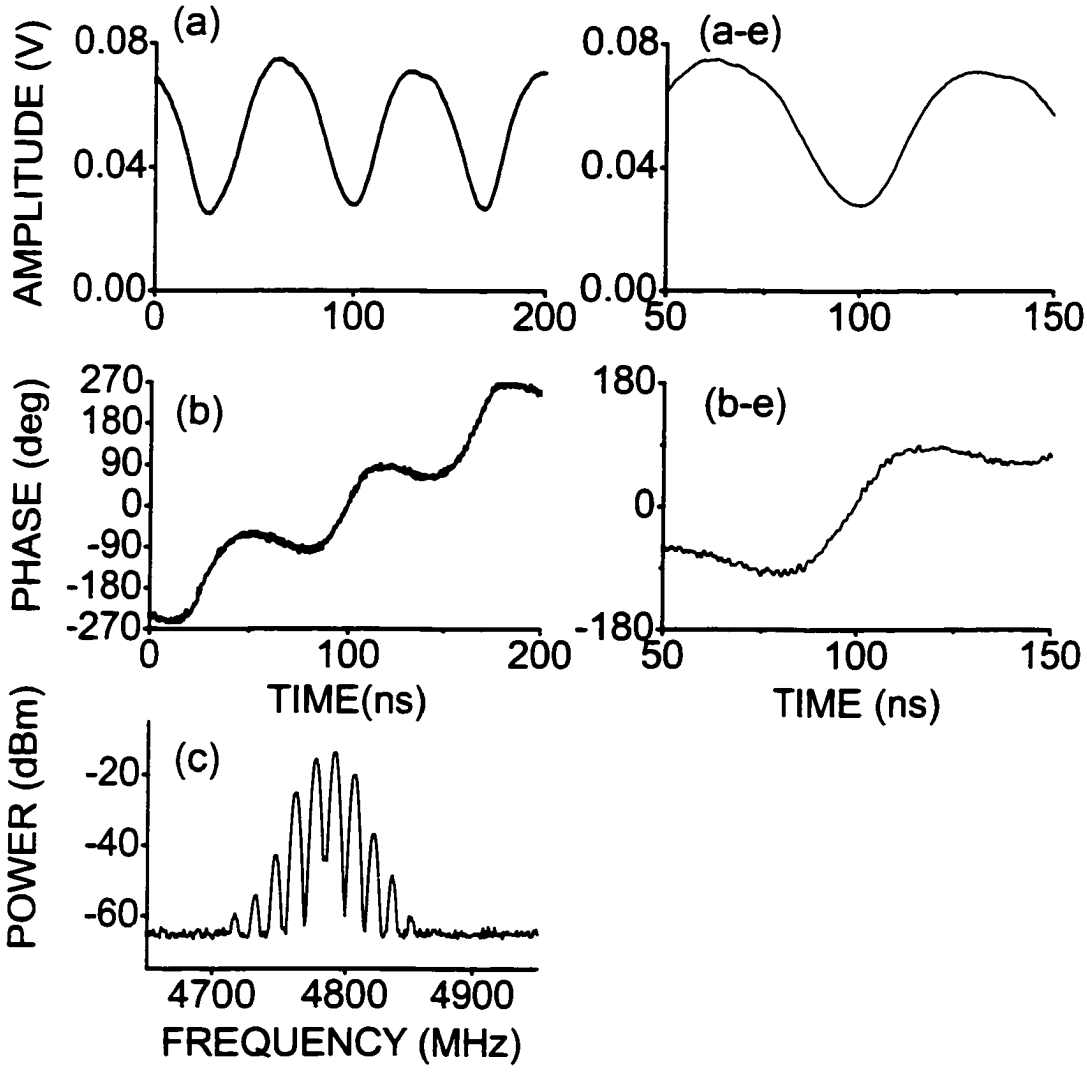

Figure 6.3. Gray soliton pulse train characteristics. Graphs (a) and (b) show the detected microwave voltage and phase profiles, respectively, for the self generated signal in the ring structure for a gain of +0.5 dB. Graphs (a-e) and (b-e) show the same signals as in (a) and (b) but on an expanded time scale. Graph (c) shows the corresponding power-frequency spectrum of the ring signal.

phase changes for each dip of about 150°. The widths of the gray soliton dips were found to change with the strength of the ARR gain. Higher gains yielded narrower widths.

The dark soliton response characteristics shown in Figures 6.2 and 6.3 could be maintained for a range of gain settings of approximately 1 dB. When the ring gain is significantly higher than +0.5 dB, as for the above data, the amplitude and phase profiles become distorted and the power frequency spectrum demonstrates bifurcations and a chaotic behavior. These features of the response at high gain levels require further study. In addition to the achievement of fundamental dark soliton generation, the technique has potential applications to the study of chaos in these systems.

In summary, the self generation of single SWE black solitons has been reported. The filtered feedback technique allows for the self generation of *single* stable black and gray microwave solitons, even though the phase constraints imposed on black solitons preclude their creation from conventional input microwave signals. The combination of a properly devised filtering response for the MSW signal feedback in the resonant ring structure, the modulational instability of the MSW signals and the repulsive nonlinearity of the MSSW excitations, make possible the creation of such fundamental dark soliton signals. This technique represents a new and generally applicable approach to dark soliton production for nonlinear dispersive waveguiding media.

6.2 Bright Soliton Self Generation in a Frequency Filtered Active Resonant Ring

This section presents results on the self generation of SWE bright solitons in a

frequency filtered ARR structure. Essentially, the technique used here to self generate bright envelope solitons is identical to that of the dark envelope soliton generation described in Section 6.1. In this case, however, the delay line of the frequency filtered ARR structure is rotated into the MSBVW configuration where the formation of bright solitons is predicted by the single NLS equation model. As described in Chapter 3, bright envelope solitons are robust, narrow, nonlinear pulses which have a constant phase profile across their width.

The main body of experimental results on envelope *bright* solitons trains in solid state media has been for optical solitons in fibers and SWE solitons in ferrite films. A considerable amount of the work on optical bright soliton trains is reviewed by Taylor [3]. Recently, SWE bright soliton trains have been excited in active resonant rings through the use of synchronized time gating [6]. The results presented in this section demonstrate that complicated bright microwave pulse sequences, which are needed for modern signal processing applications, can be obtained with magnetic structures and frequency filtering in a relatively simple manner. One may contrast the simplicity of this technique with Reference 6 or with a recently reported technique for the generation of bright microwave pulses which utilizes a fifteen component array of coupled phase locked loops [26].

Aside from a slightly higher field strength and the orientation of the YIG film delay line, all other parameters used in the self generation of SWE bright solitons were the same as those in Section 6.1. Similar to Section 6.1, these parameters were chosen such that the transmission profile of the u-shaped transducer delay line matched the width of the power frequency spectrum for the target *bright* soliton train. Additionally, the

amplifier response was chosen to insure that the nonlinear response of the ARR structure was determined solely by the MSBVW excitations in the YIG film. A detailed description of the frequency filtered ARR structure is given in Chapter 4.

Due to the similarities in the experiments here to those described in Section 6.1, the procedure used to self generate a stable train of bright solitons is only briefly reviewed. First, the transmitted power vs. frequency profiles of the MSBVW YIG film delay line was measured in the absence of feedback at low power. Second, additional transmission vs. frequency profiles were measured for the entire ring structure with different values of the ring gain. Fine adjustments to the external magnetic field were made to obtain a ring resonance response profile at high gain with a pronounced spike at the maximum transmission point of the YIG film delay line. Third, the external source was disconnected and the gain was increased above the oscillation threshold. As the gain was increased, a train of narrow microwave pulses was measured at the output of the ring. The power and phase vs. time profiles, along with the power vs. frequency spectrum, of these pulses were used to confirm their bright soliton nature.

Figure 6.4 shows two representative output power vs. frequency response profiles obtained for a low input power. The profiles in Figure 6.4 are similar to those in Figure 6.1 except that the profiles in Figure 6.4 are for MSBVW excitations rather than MSSW excitations. Graph (a) corresponds to the u-shaped transducer YIG film delay line response in the absence of feedback. Graph (b) corresponds to the ARR response with feedback in place and the gain set approximately to the oscillation threshold. As in Section 6.1, the ring gain for this condition was observed empirically and will be taken as 0 dB. The insets of graphs (a) and (b) show schematics of these two cases.

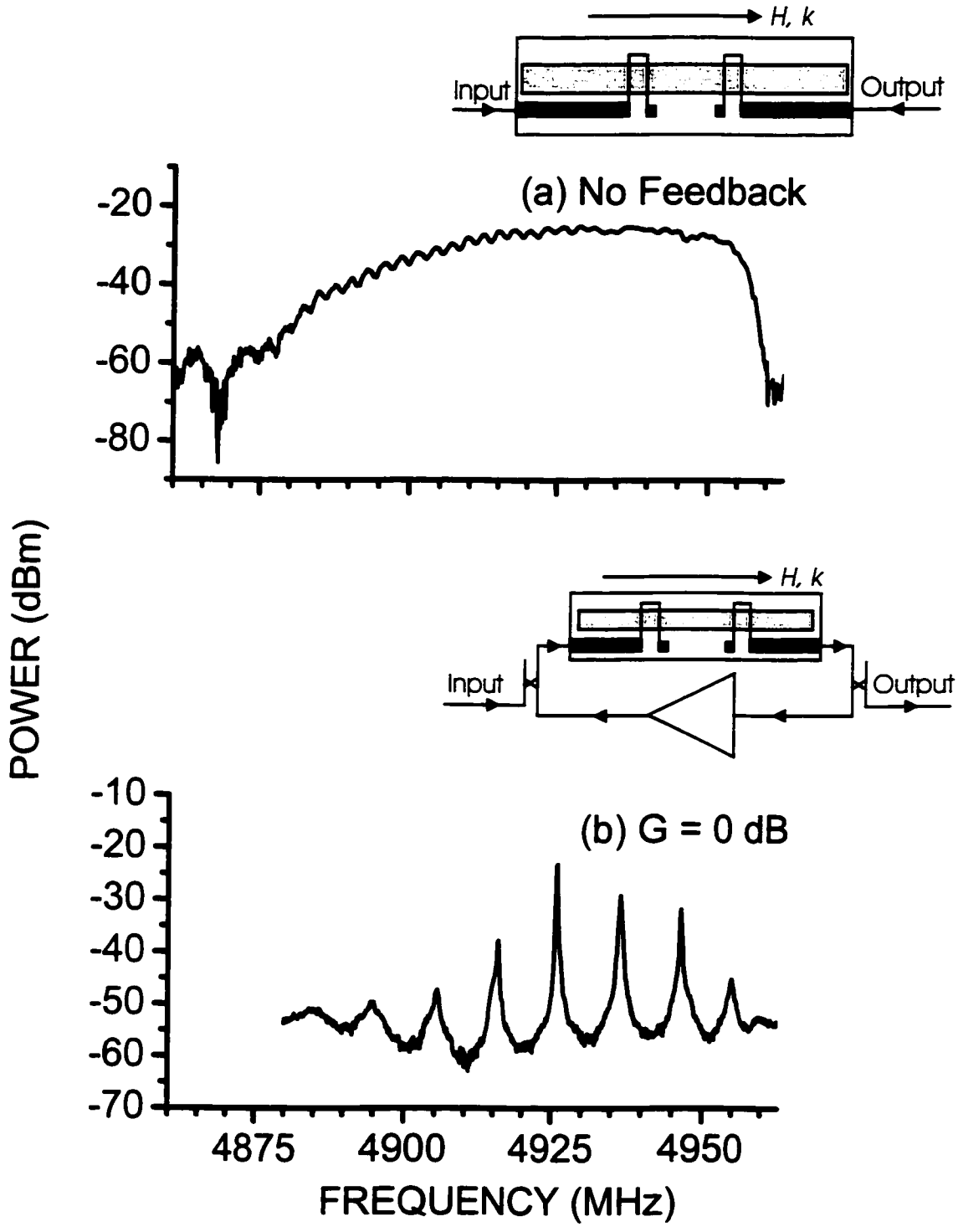

Figure 6.4. Low power frequency profiles for the delay line ring structure (a) with no feedback and (b) with feedback set at the oscillation threshold 0 dB gain point.

The profile in (a) is typical of the delay line pass band response for MSBVW excitations described in Chapter 4, but modified due to the special u-shaped antennas as described in Chapter 4. The pass band extends from approximately 4860 MHz to 4970 MHz and has a broad maximum centered around 4920 MHz. The low frequency limit corresponds to a maximum wave number obtained from the MSSW dispersion given by Equation (2.13) of approximately $k_{max} \approx 210\,\text{rad/cm}$. The parameters used in Equation (2.13) were S = 6.9 μm, $4\pi M_s = 1900\,\text{G}$, and $H = 1063\,\text{Oe}$. This k_{max} is in reasonable agreement with Equation (4.3) $k_{max} \sim 2\pi/d \approx 250\,\text{rad/cm}$ for the u-shaped transducer, where d is the separation between the elements of the transducer.

The profile in Figure 6.4 (b) shows pronounced spikes which correspond to the resonant frequencies of the ring. At these spike points, the phase matching condition $k_n L + \phi_e = 2\pi n$ given by Equation (4.2) is satisfied. The spike spacing is approximately 10.5 MHz. This separation is smaller than that for the MSSW case in Section 6.1 due to smaller slope of the MSBVW dispersion. Note the presence of one pronounced central spike and several side spikes. The side spikes are smaller than the central spike by more than 7 dB. The spike spacing, positions, and amplitudes are all a sensitive function of the delay line parameters and the field H. The adjustment of H was used to match the main spike in (b) to the maximum transmission point in (a). When the external source is disconnected and the gain is increased to the 0 dB point, this central frequency will self oscillate and dominate the linear response. In the nonlinear self oscillation regime at gains above 0 dB, this dominant central frequency will provide the seed response for the formation of bright solitons.

Figure 6.5 shows representative data on the self generation of bright solitons when

the gain is well above the oscillation threshold. The data shown are for a ring gain of 1 dB and other parameters as given above. Graph (a) shows the power vs. time profile for the soliton pulse train measured at the output of the ARR structure. Graph (b) shows the corresponding phase vs. time profile. Graph (c) gives the power vs. frequency spectrum for the signal in (a). Except for the phase data, these results are representative of data obtained with no microwave input signal. An additional low power 4927 MHz reference signal was used for the phase measurements in (b). This signal had no effect on the soliton response.

The signal characteristics for these data match those expected for SWE bright solitons. The data in (a) show the sequence of narrow microwave soliton pulses generated in the frequency filtered ARR structure. The half power pulse width of the pulses in (a) is approximately 20 ns. The phase data in (b) show the characteristic regions of constant phase across the central portion of each pulse in (a). These flat phase regions provide a quantitative signature for bright solitons. The power spectrum in (c) shows the multiple frequency harmonics which correspond to the self generated soliton pulse train in (a). Note that the band width for these harmonics match approximately the u-shaped transducer YIG film delay line frequency pass band width shown in Figure 6.4 (a). Note also that the positions of these harmonics match the resonant frequencies of the ring indicated in Figure 6.4 (c). The 10.5 MHz spacing of these harmonics implies a repetition rate for the temporal pulse train of 95.2 ns. This value closely matches the experimental pulse spacing of 94.3 ns from (a). Taken together, the data in Figure 6.5 support the bright soliton nature of these self generated microwave pulses.

Further data show that the pulse trains generated in the ring are stable and can be

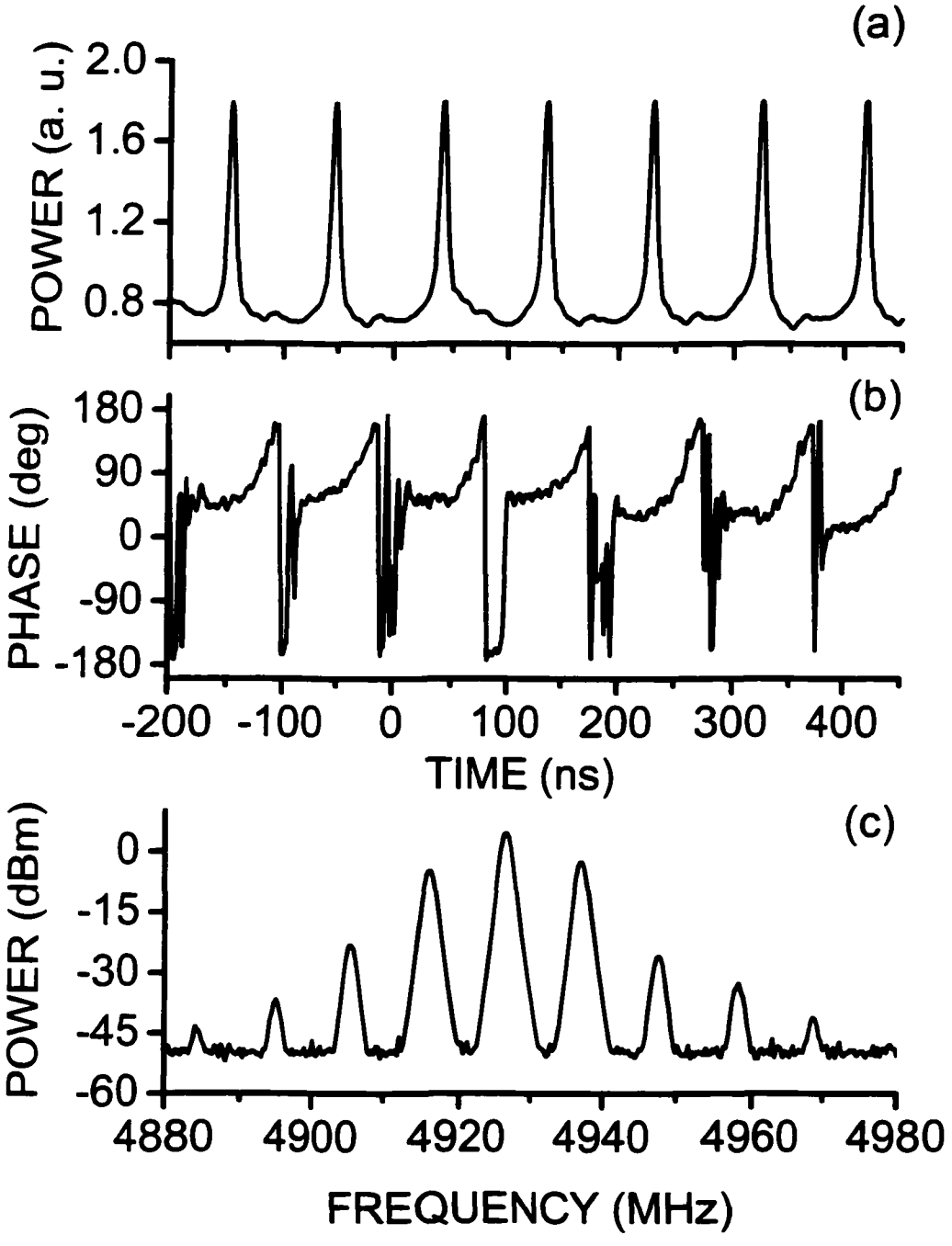

Figure 6.5. Bright soliton pulse train characteristics. Graphs (a) and (b) show the microwave power and phase profiles, respectively, for the self generated signal in the ring structure at a ring gain of +1 dB. Graph (c) shows the power frequency spectrum of the pulse train in (a).

maintained indefinitely. Stable SWE bright soliton self generation was observed over a range of ring gain values of about 2 dB. At higher gains, the signals changed significantly. The details of these changes under high gain conditions warrant further study. The main effects appear to be (1) the appearance of bifurcations in the power vs. frequency spectra and (2) the development of a chaotic signal response at very high values of the ring gain.

In summary, the self generation of bright spin wave envelope solitons by a new and general filtering technique is reported. As in Section 6.1, the key to the process is a properly devised filtering response for the nonlinear excitations. The combination of (1) the filtered feedback in the resonant ring structure, (2) the modulational instability of the ring resonances, and (3) the attractive nonlinearity of the MSBVW excitations, produces the soliton signals for a small range of gain values above the linear oscillation threshold for the ring.

The filtering technique represents a new approach to soliton generation in nonlinear dispersive waveguiding media. Previous techniques required the use of synchronized time gating. The frequency filtering allows for the excitation of a soliton train for an indefinite time duration without the application of external signals. From the point of view of applications, the filtering technique provides a new way to produce electronically controllable complicated microwave pulse configurations for various microwave engineering applications [26, 27].

CHAPTER 7

THE GENERATION OF SWE SOLITONS THROUGH NONLINEAR MODE BEATING

This chapter presents results on SWE solitons formed due to the induced modulational instability of two co-propagating MSW excitations. The formation of envelope bright and dark soliton trains through nonlinear mode beating technique has been observed in optical fibers [3] and in ferrite films [9, 10]. However, the spatial formation processes, among others, for these solitons have not been observed. The nature of the propagation of optical solitons within fibers makes their spatial formation processes difficult to probe. In the case of SWE solitons in YIG films, these processes are easily accessed through the newly developed IMP system described in Chapters 4 and 5. In Chapter 5 the linear behavior MSW excitations was probed with the IMP system. The IMP system will be used here to probe the nonlinear behavior of co-propagating MSW excitations in the 6.9 μm thick YIG film.

As in the experiments of References 9 and 10, the application of two high power microwave signals to the input of a YIG film delay line allowed for the excitation of both bright and dark spin wave envelope soliton trains. Above some threshold power, the induced modulational instability, coupled with the attractive or repulsive nonlinearity of the system, led to the formation of trains of solitons. Though the mechanisms are

different, the solitons excited through mode beating are similar to those excited through the filtered feedback technique of Chapter 6.

In Chapter 6 the results for MSSW excitations were presented first due to their novelty. In this chapter, however, the results for MSBVW excitations will be presented first. In Section 7.1, the power and phase vs. time profiles, along with the power vs. frequency spectrum, of a train of bright solitons were measured together for the first time. In addition, the bright soliton pulse width as a function of applied signal frequency separation was measured. The observation of the spatial recurrence [2] of a train of these SWE bright solitons will be presented. This recurrence was modeled through the single NLS model. Ultimately, a train of *black* nonlinear pulses was observed for these nonlinear MSBVW excitations for the first time. Black nonlinear pulse formation is not predicted by the single NLS equation model for MSBVW excitations with attractive nonlinearity. Spatial recurrence was not observed for these black nonlinear pulses.

In Section 7.2, the MSSW excitation results will be presented. Similar to Section 7.1, the power and phase vs. time profiles, along with the power vs. frequency spectrum, of a train of black solitons were measured together for the first time. In addition, the black soliton pulse width as a function of applied signal frequency separation was measured. The black soliton pulse width vs. input power was measured for the first time. Furthermore, the formation of MSSW *bright* nonlinear pulses was observed. Bright nonlinear pulse formation is not predicted by the single NLS equation model for MSSW excitations with repulsive nonlinearity. No spatial recurrence was observed for these bright or dark nonlinear MSSW pulses.

7.1 Magnetostatic Backward Volume Spin Wave Solitons Formed due to Nonlinear Mode Beating

The formation of SWE bright solitons due to the induced modulational instability of two co-propagating volume MSW excitations has been previously observed [9]. In Reference 9, the bright soliton train behavior as a function of input power was observed. However, the spatial formation processes, phase response, and behavior as a function of input frequency separation have not been observed for these pulse trains. In addition, the excitation of *dark* soliton like pulses has not been observed experimentally. From the point of view of the fundamental science, this investigation helps to illuminate the physics of two coupled waves. In addition, this work relates to and illuminates the process of the self generation of bright soliton trains in active resonant rings [28] presented in Chapter 6.

Through the basic MSW delay line measurement system, trains of bright solitons formed due to the nonlinear mode beating of MSBVW excitations, similar to those observed in Reference 9, are generated. Then the phase vs. time response and pulse width vs. frequency separation of these solitons are measured with the IMP system to help verify their soliton nature. The IMP system is then used to probe the spatial behavior of these solitons. The last part of this section addresses the formation of dark nonlinear MSBVW pulses.

Figure 7.1 shows four important graphs obtained at a nominal magnetic field of H = 1261 Oe. Graphs (a) and (b) show data in the frequency domain. Graphs (c) and (d) show data in the time domain. These data are key to the experimental process used to

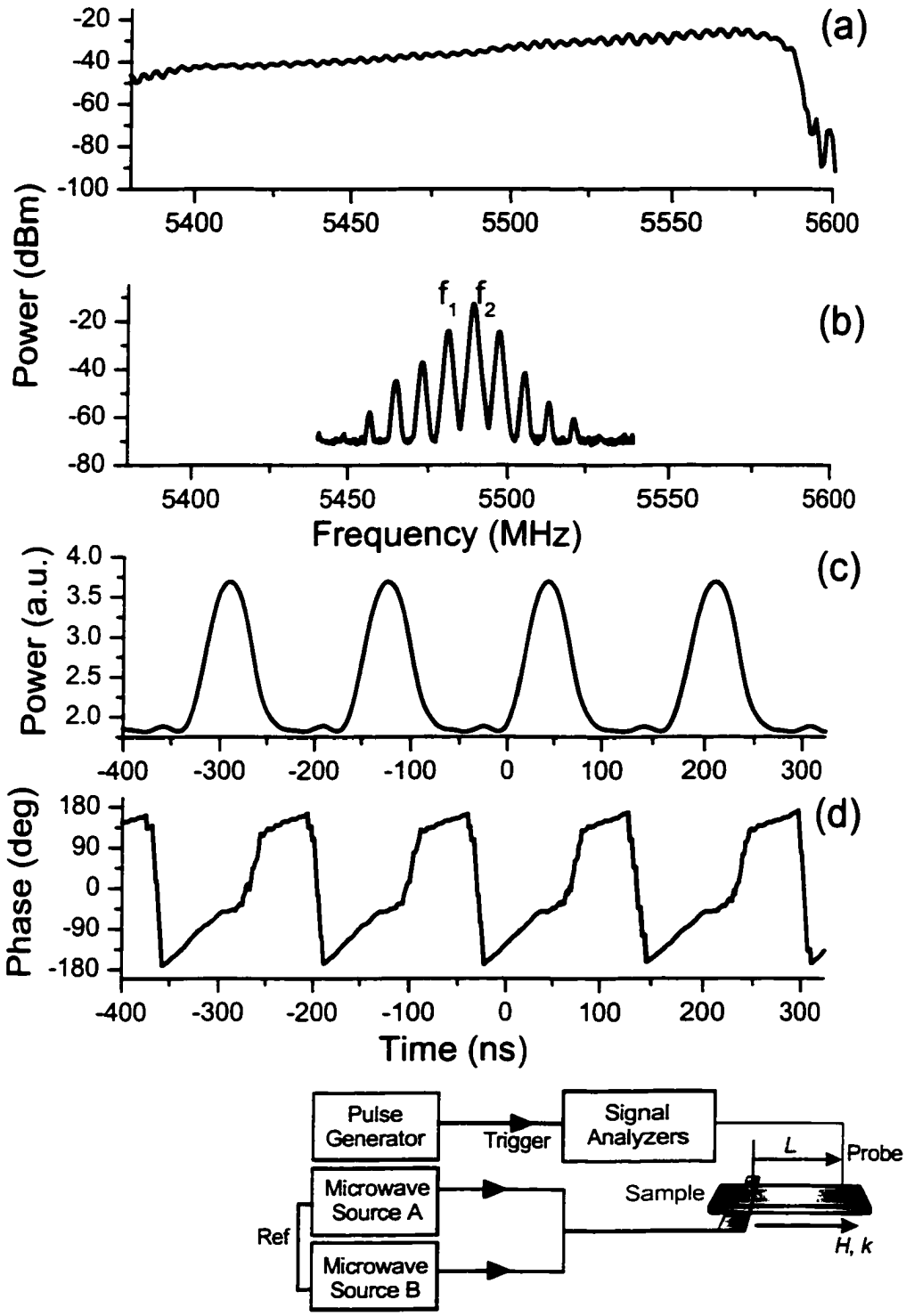

Figure 7.1. Transmitted power vs. frequency characteristic of the YIG film delay line and bright soliton pulse train characteristics. Graph (a) shows the delay line characteristic. Graph (b) shows the power vs. frequency spectrum which results from the application of two high power microwave signals to the input of the delay line. Graphs (c) and (d) show the power and phase vs. time characteristics of the bright soliton train,

generate solitons by nonlinear mode beating. A simple schematic of the experiment based on the IMP measurement system is shown in Figure 7.1.

Graph (a) shows the transmitted power vs. frequency characteristic of the single element transducer YIG film delay line. This characteristic was measured by the probe at a distance of 7 mm from the input transducer along the central axis of the film. For the data in (a) a low power microwave signal from source A was applied to the input of the delay line. The characteristic in (a) shows a narrow 200 MHz span of the MSBVW excitations, starting from approximately 5590 MHz, which is approximately two times wider than the frequency spectrum of the soliton pulse trains observed here. This insures that the losses are nearly constant across the width of the soliton frequency spectrum. This minimizes possible filtering effects.

Graph 7.1 (b) shows a representative power vs. frequency spectrum which results from the application of two high power microwave signals of different frequencies. The spectrum in (b) was received by the probe of the IMP system at the same position as for graph (a). For the spectrum in (b), the applied signal frequencies from sources A and B were 5497 and 5491 MHz, respectively. These signal frequencies are labeled f_1 and f_2 in (b) and had high input power levels of 25 and 17 dBm, respectively. These power levels were in the induced modulational instability regime. The induced satellite harmonics are visible in (b). The 6 MHz frequency separation between the applied signals and the adjacent satellite harmonics is visible in graph (b).

Turn now to the characteristics in the time domain. Figure 7.1 (c) shows a representative power vs. time profile which corresponds to the frequency spectrum shown in (b). This signal was received by the probe simultaneous to the spectrum in (b). Notice

the narrow soliton-like shape of the profiles in (c). The half power width of the pulses in (c) is approximately 50 ns. Notice further that the 167 ns pulse repetition period is equal to the inverse of the 6 MHz frequency separation of the applied signals. The data in (c) are similar to the data in Reference 9.

Figure 7.1 (d) shows the phase vs. time characteristic of the soliton pulse train. This characteristic was also measured by the probe simultaneous to the characteristics in (b) and (c). The vertical axis in (d) shows phase difference, relative to a reference signal at the frequency f_1, measured in degrees. The measurement of phase is detailed in Chapter 4. The phase profile is used to help confirm the bright soliton nature of the pulses in (c). Notice that, at the position in time of the pulses in (c), the phase characteristic shows a slight plateau. This characteristic is indicative of a bright soliton. Notice that the plateau does not extend across the entire width of the pulse. This is an indication that the solitons in (c), and thus the phase plateaus in (d), are not fully formed due to insufficient power. For higher power levels the modulation depth of the pulses in (c) would be greater and the phase plateaus in (d) would extend across the full width of the pulse.

In order to further confirm the nonlinear nature of the pulses under investigation, the half power width of the pulses was recorded as a function of frequency detuning $\Delta f = |f_1 - f_2|$ for constant input power levels of the signals. The probe distance from the input transducer was 7 mm. The power levels were 17 and 25 dBm, as above. The position in frequency of the signal f_1 was held constant at 5497 MHz and the value of f_2 was varied. The measurement results are shown in Figure 7.2. The vertical axis shows the half power pulse width in ns. The horizontal axis shows the frequency detuning of the input signals in MHz. The solid squares in the figure are the measured points. The

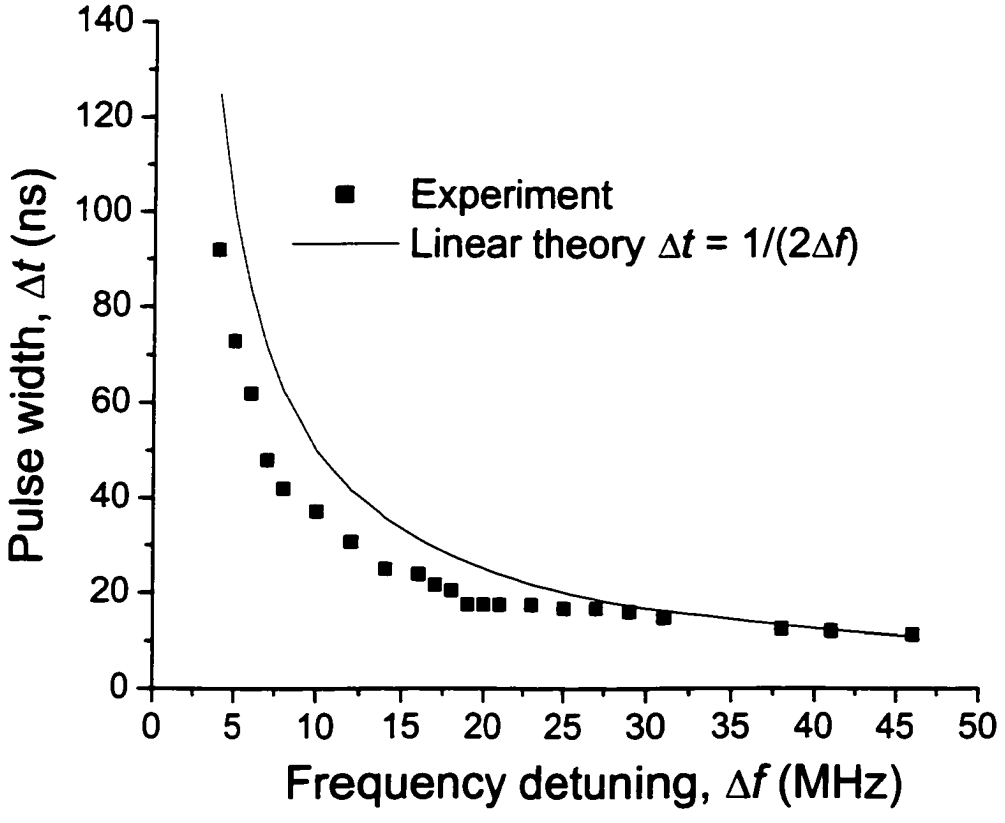

Figure 7.2. Half power pulse width vs. input signal frequency separation. The solid squares show the results of the measurements. The solid line shows the linear relation $\Delta t = 1/(2\Delta f)$. The region where the measured points fall below the solid line coincides with the region of induced modulational instability.

line shows the half power pulse width in the linear regime given by $\Delta t = 1/(2\Delta f)$.

In the region of frequency detuning between 4 MHz and 30 MHz the induced modulational instability leads to pulse narrowing and the solid squares fall below the line in the graph. Below 4 MHz, the time profiles became distorted due to losses. This is in accordance with the prediction of Equation (3.15). Equation (3.15) predicts a modulation frequency on the order of tens of MHz for self modulational instability. The larger instability region, observed here up to 30 MHz, is in accordance with the predictions that the coupled wave modulational instability is richer than that of a single wave [21]. In this region, narrow bright soliton like profiles were observed. For values of large frequency detuning the solid squares lie on the line. This is an indication that, even at high power, the induced modulational instability does not lead to a narrower pulse width for frequency detunings above approximately 30 MHz. Note that for detunings in this range, the filtering introduced by the delay line pass band is more significant. In this region linear mode beating profiles were observed. It should be noted that the 10.5 MHz frequency separation used in Section 6.2 also lies in this band of instability.

Aside from the power vs. time data in 7.1 (c), which can be found in Reference 9, the data in Figures 7.1 and 7.2 are completely new. These data were used to establish the soliton nature of the pulses and the region of induced modulational instability for the parameters of this experiment. With this established, the formation processes of these bright envelope soliton trains were investigated.

For the investigation of the spatial formation process of these nonlinear pulses the frequency separation was chosen as $\Delta f = |f_1 - f_2| = |5497 - 5489|\,\text{MHz} = 8\,\text{MHz}$ and the power levels were 25 and 17 dBm. The frequency detuning is well within the

experimentally observed region of instability and the power levels were sufficient for bright soliton train formation. The data to be presented in the two subsequent figures are related to the spatial recurrence of these bright soliton pulse trains. In order to understand the results in these figures one must understand the IMP system time and space resolved capabilities explained in Chapter 5. This system relies on a sophisticated triggering and synchronization mechanism and is shown in simplified schematic form in Figure 7.1. With this system in place it is possible to make reliable time and space resolved measurements.

The graphs in Figure 7.3 show a periodic progression in the shape of the envelope profiles. The corresponding frequency spectra are shown to the right of the individual waveforms. The format of the spectra is the same as those in Figure 7.1 (b) except that the span in frequency is narrower. The L values in the graphs denote the probe distance from the delay line input transducer along the central axis of the film. The sequence of traces shows half of the 0.42 mm spatial recurrence period with the recurrent soliton train waveform given in (a) and (e). The full period waveform progression is obtained from the sequence (a) to (e) and from (e) back up to (a). Traces (b), (c), and (d) show the progression from "overmodulated" to period doubled to "undermodulated". Note that the modulation depth of these pulses is small compared to unity. It is of interest to note that the carrier wavelength of the signal was approximately 0.48 mm. This wavelength corresponds approximately to the full recurrence period. It is of further interest to note that the frequency spectrum of the pulse train in (a) was not significantly altered as a function of distance. This fact will be useful in the model to be presented later.

Figure 7.4 shows the results of a time and space resolved measurement performed on

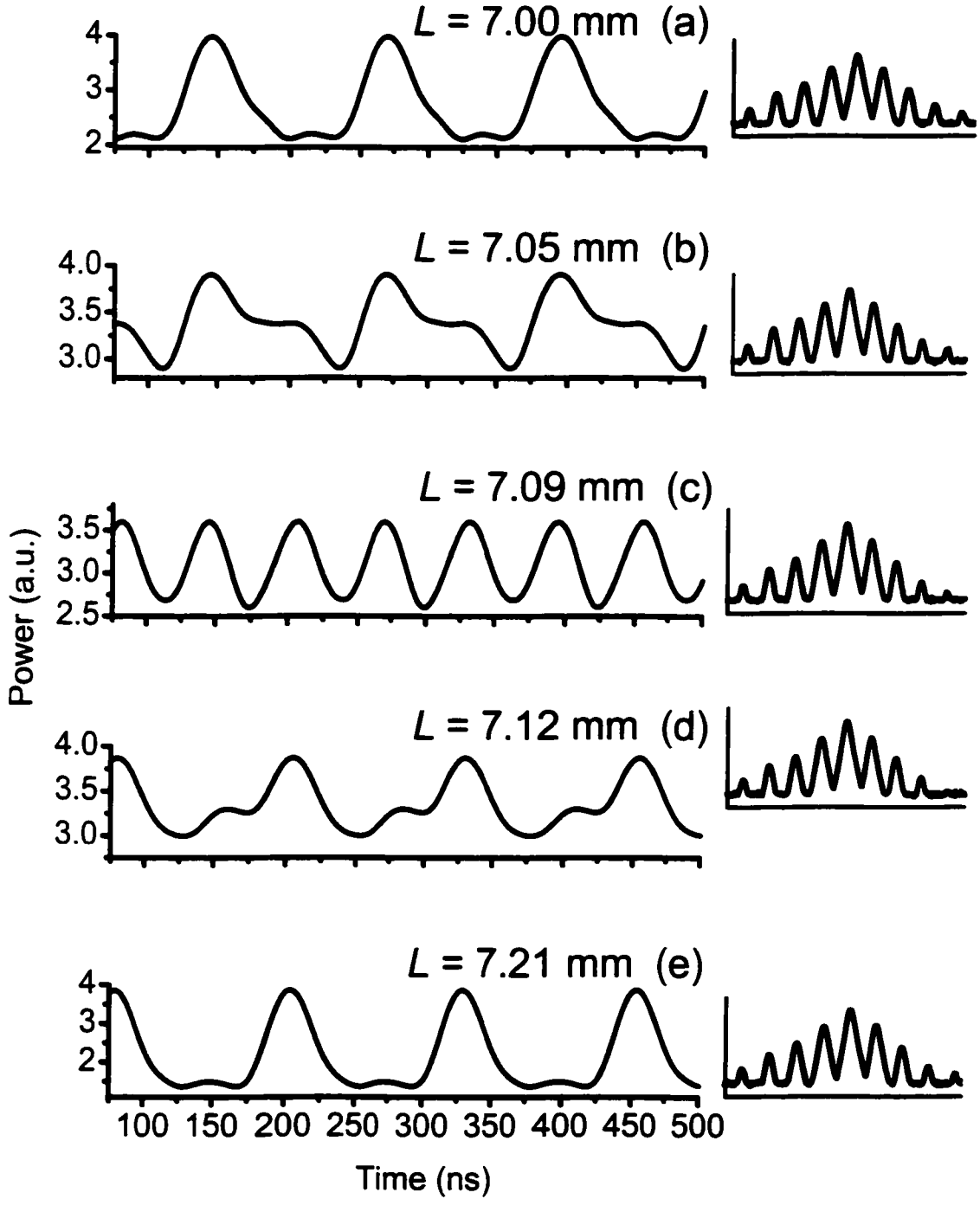

Figure 7.3. Pulse train power vs. time. The pulse trains in graphs (a) – (e) show a recurrent progression in the shape of the envelope profiles. The L values in the graphs denote the probe distance from the delay line input.

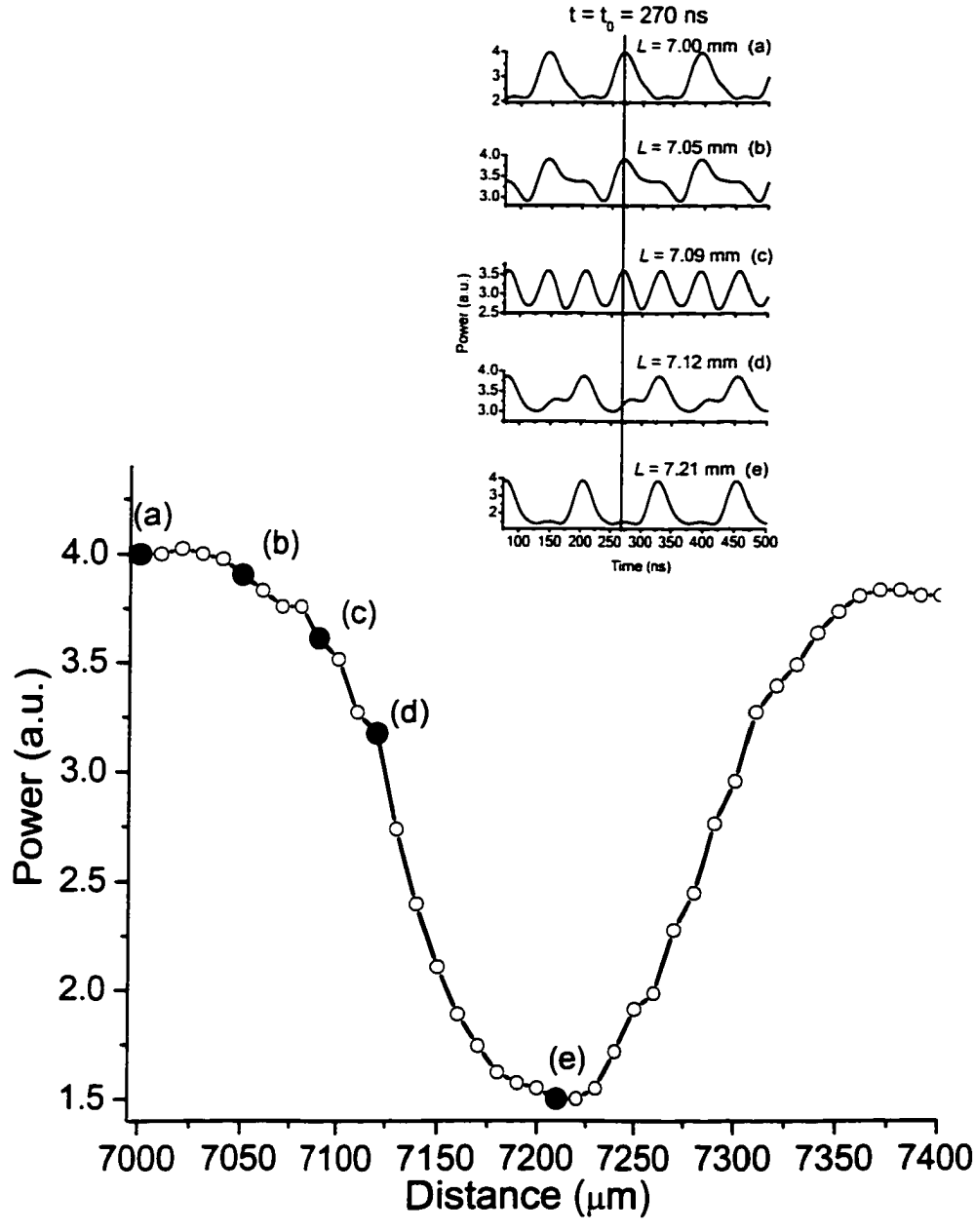

Figure 7.4. Time resolved scan of the recurrent waveforms of Figure 7.3. The vertical axis shows power in arbitrary units and the horizontal axis shows distance in microns. The solid black circles labeled (a) – (e) show the positions of the pulse trains of Figure 7.3. The inset shows the recurrent waveforms of Figure 7.3 with the constant time for the scan of 270 ns indicated by the solid vertical line.

a pulse train progression similar to those shown in Figure 7.3. The pulse train progression shown in Figure 7.3 was reproduced as nearly as possible for the measurements shown in Figure 7.4. For the one dimensional data in the graph, the probe moved along the central axis of the film a distance of 400 μm starting from a distance of 7 mm from the input transducer in 10 μm steps. The power level of the signal received by the probe was recorded for a constant time at each point on the scan. In the case of the data in Figure 7.4 that time was chosen as 270 ns. The inset shows the waveforms of Figure 7.3 with the constant time for the scan indicated by the solid vertical line.

The result of this scan is shown as open circles in Figure 7.4. The black circles labeled (a) - (e) in the graph correspond to the position of the (a) – (e) waveforms in Figure 7.3. One might expect to receive a spatial profile which reproduced the time profile due to the relation between space and time $L = |v_g| t$. However, since the pulse shape changes as a function of distance such a reproduction is not observed. The periodic data in the figure essentially map the background power level of the individual pulse trains. Similar periodic data were obtained for different constant times.

In order to model the results in Figures 7.3 and 7.4, the frequency spectrum of the soliton train in Figure 7.3 (a) was used. This spectrum was converted to linear amplitude and normalized to unity. The largest carrier frequency power level was set to unity. From this spectrum, the relative amplitude of each of the signals was determined. In addition, the phase of each of the signals was determined using a relation based on the NLS Equation (3.7) given here as

$$\Phi_n = \omega_n t + \left[k_0 + \frac{(\omega_n - \omega_0)}{v_g} - \frac{D}{2}\frac{(\omega_n - \omega_0)^2}{v_g^3} + \frac{N}{v_g} A_n^2 |u|^2 \right] L . \qquad (7.1)$$

In Equation (7.1), ω_n is the angular frequency of the given excitation determined from the frequency spectrum and $\omega_0 = 2\pi f_0 \approx 3.5\times10^{10}$ rad/s and $k_0 = 130$ rad/cm are the angular frequency and wavenumber of the central carrier determined from the frequency spectrum and dispersion characteristic in Figure 5.6. The parameters v_g, D, and N were determined from the relations given at the end of Chapter 3 for MSBVW excitations. The propagation distance is given by L. The power level of the excitation is given by A_n^2. The A_n values were obtained from the frequency spectrum and, as mentioned above, all of the values were normalized to $A_0 = 1$. The value of $|u|^2$ was estimated from the theory [8]. The result yielded $|u|^2 = 0.027$. For the modeling the other parameters in Equation (7.1) are given here. The values of the saturation magnetization and film thickness were taken from Chapter 5 on the sample characteristics as 1900 G and 6.9 μm, respectively. The value of the external field was taken as 1261 Oe. The parameters v_g, D, and N were calculated from these parameters using Equations (3.17), (3.19), and (3.21). The results yielded $v_g = -3.64\times10^6$ cm/s, $D = 1298\,\text{cm}^2/\text{rad}\cdot\text{s}$, and $N = -1.1\times10^{10}$ rad/s.

With the above parameters a series of cosines

$$A_\Sigma = \sum_{n=-4}^{4} A_n \cos(\Phi_n), \tag{7.2}$$

with Φ_n given by Equation (7.1) and amplitudes A_n obtained from the frequency spectrum, were summed. A total of nine harmonics were used. The frequencies and amplitudes of these harmonics are shown in Table 7.1. The result, A_Σ, was squared and plotted in Figure 7.5 (a) – (e) for the set of distances L determined approximately from

Table 7.1. Parameters used in the modeling of the recurrence effect based on Equations 7.1 and 7.2.

Harmonic number, n	**Harmonic frequency, f_n (MHz)**	**Harmonic amplitude, A_n**
-4	5725	0.0040
-3	5733	0.0088
-2	5741	0.0369
-1	5749	0.2603
0 (carrier number)	**5757 (carrier frequency)**	**1.0000 (normalized carrier amplitude)**
1	5765	0.2761
2	5773	0.0610
3	5781	0.0253
4	5789	0.0052

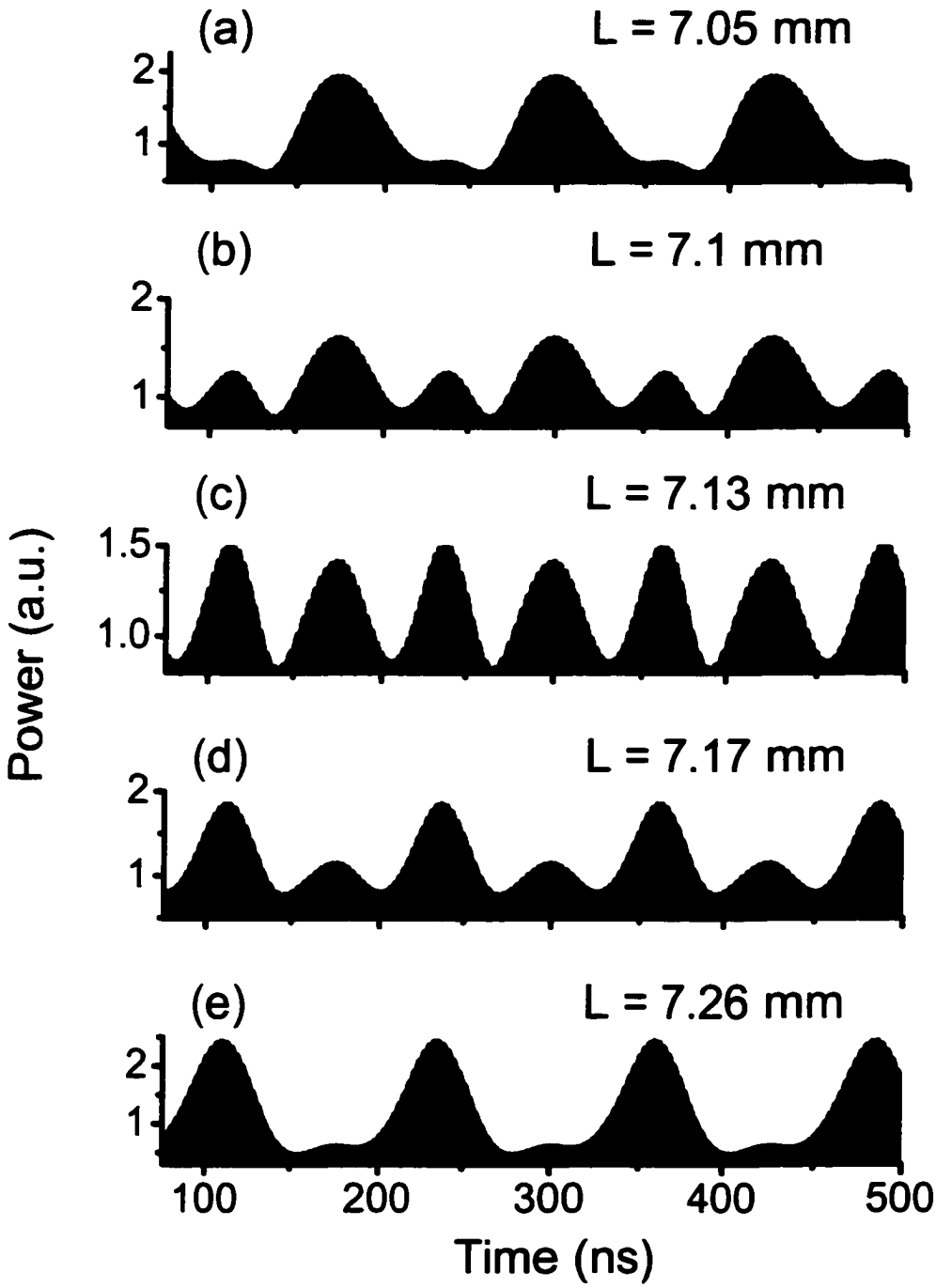

Figure 7.5. Results of modeling for the waveforms in Figure 7.4 through the use of Equation (7.2). The model is based on the single NLS equation model. Parameters were calculated from Equations (3.17), (3.19), and (3.21). The L values in the graphs denote propagation distances.

the experiment. The L values in the graphs denote the wave propagation distances used in the calculations. The same progression shown in Figure 7.3 is observed with the help of this simple model. Graphs (a) and (e) show the recurrent soliton like pulse train. Graphs (b) and (d) show "overmodulated" and "undermodulated" pulse trains, respectively. Graph (c) shows the period doubling. In addition to the qualitative agreement with the experimental pulse shapes, the half period of 0.21 mm for the spatial recurrence phenomena is approximately reproduced by the model. Though more sophisticated modeling is required, this simple model gives a good physical understanding of the mechanisms at work and a reasonable agreement with the data. It is important to note that without the power dependent phase term in Equation (7.1) no recurrence of any kind was observed in the model. This is an indication of the nonlinear nature of the spatial recurrence effect. Note further that all of the parameters used in Equations (7.1) and (7.2) were calculated from theory and were not adjusted to fit the data.

Figure 7.6 shows the results of modeling the effect observed in Figure 7.4. As in Figure 7.4, the power values at the constant time of 300 ns were calculated for a variety of distances from 7 mm to 7.7 mm. The open circles show the power levels obtained at these distances. The agreement with the shape of the experimentally observed curve is good. Although the theoretical curve observed here has a larger period when compared to the experiment. The black dots labeled (a) – (e) indicate the approximate positions of the waveforms (a) – (e) of Figure 7.5. The inset shows the waveforms of Figure 7.5 with the constant time for the scan indicated by the solid vertical line. The agreement with the waveform shape positions observed in the experiment is excellent. The data in 7.6 show

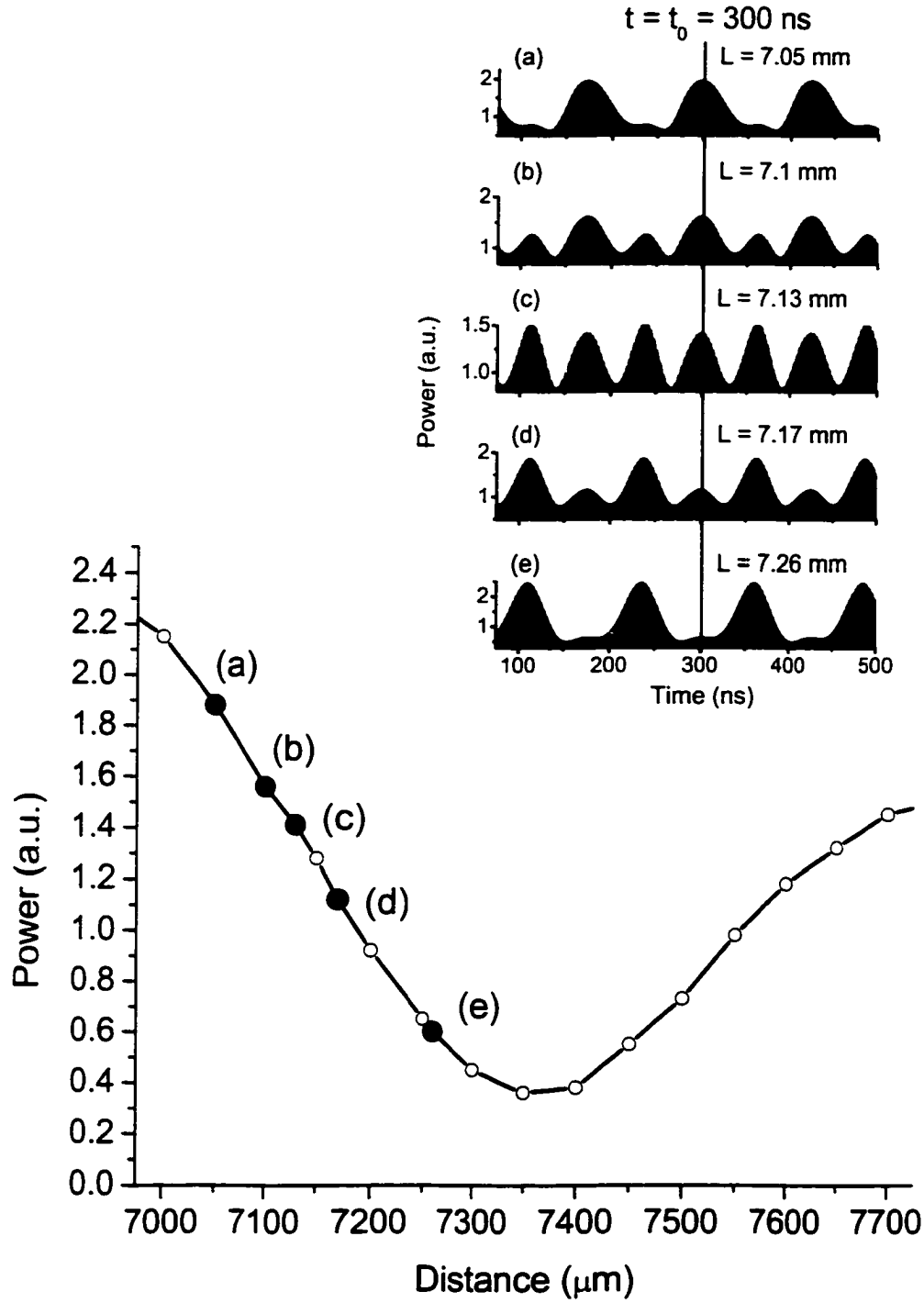

Figure 7.6. Time resolved scan of the modeled recurrent waveforms of Figure 7.5. The vertical axis shows power in arbitrary units and the horizontal axis shows distance in microns. The solid black circles labeled (a) – (e) show the positions of the pulse trains of Figure 7.5. The inset shows the recurrent waveforms of Figure 7.5 with the constant time for the scan of 300 ns indicated by the solid vertical line.

a qualitative agreement with the experiment shown in Figure 7.4. Furthermore, as in experiment, modeling done at different constant times reproduced qualitatively the same curve shapes offset by phase shifts.

Consider now the excitation of *dark* nonlinear pulse trains for MSBVW excitations with *attractive* nonlinearity. As explained in Chapter 3, such formation is forbidden by the single NLS equation. Figure 7.7 shows representative time and frequency domain characteristics of such a black nonlinear pulse train. The format of the dark pulse graphs in 7.7 (a), (b), and (c) are the same as the format of bright pulse graphs 7.1 (b), (c), and (d). The data presented in Figure 7.7 were received by the probe at a distance of 7 mm from the input transducer along the central axis of the film.

The graph in 7.7 (a) shows the frequency spectrum of the nonlinear pulse train. This spectrum is the result of the two high power microwave signals applied to the input of the delay line. In this case, the applied signal frequencies were 5483 and 5479 MHz. These signals are labeled f_1 and f_2 in the figure and each had an input power level of 25 dBm: well into the induced modulational instability regime. These equal power harmonics provide the seed response for black pulse formation. It is of interest to note that the total power here is *larger* than in the bright soliton case observed above. The satellite harmonics are visible in the figure. The separation between the applied signals and adjacent satellite harmonics was 4 MHz.

Consider now the time domain characteristics. Figure 7.7 (b) shows a representative power vs. time profile which corresponds to the frequency spectrum shown in (a). This signal was received by the probe simultaneous to the spectrum in (a). Note the narrow black soliton like shape of the profiles in (b). Note further that the dip in the profile goes

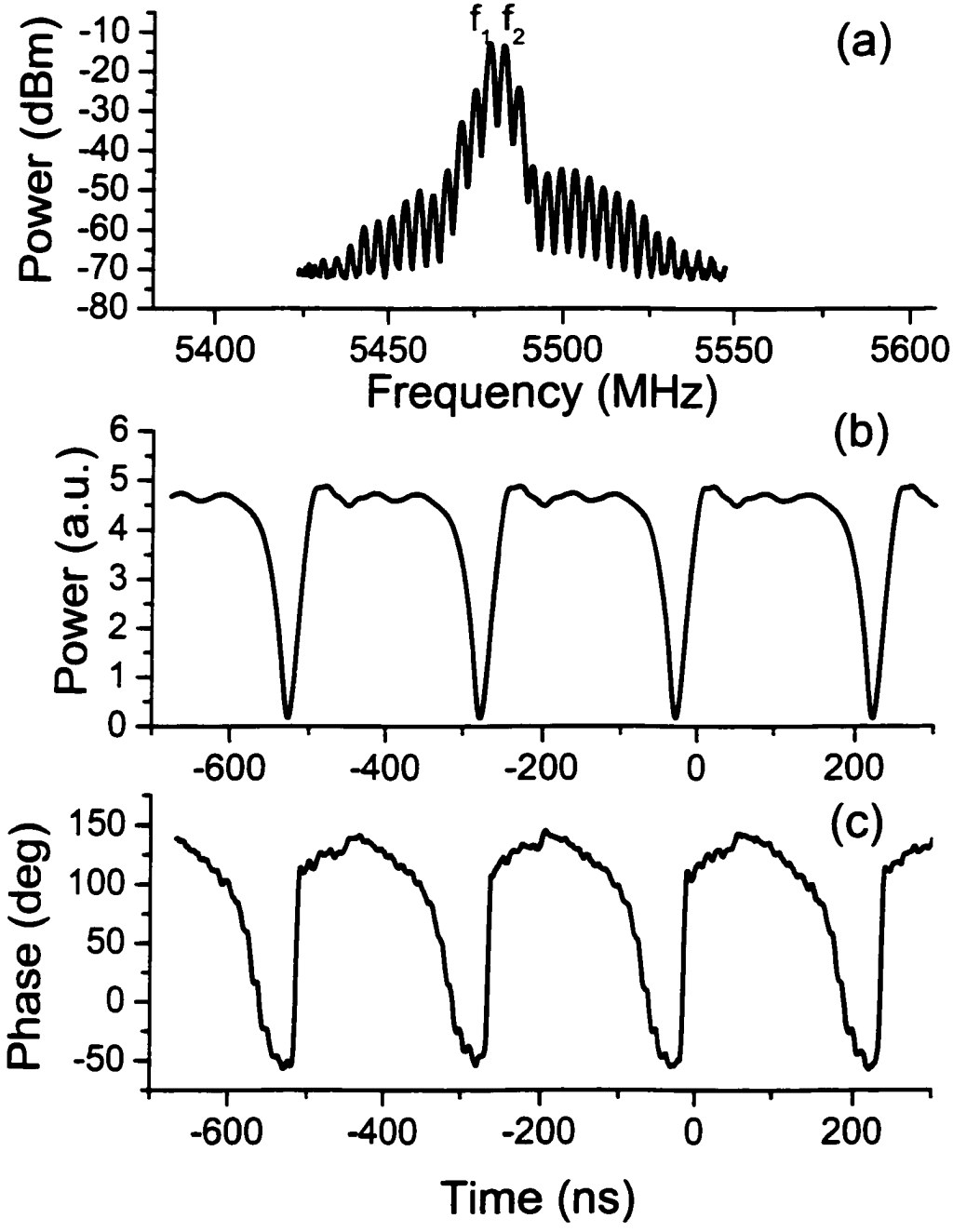

Figure 7.7. Black soliton like pulse train characteristics for MSBVW excitations. Graph (a) shows the power vs. frequency spectrum which results from the application of two high power microwave signals to the input of the delay line. Graphs (b) and (c) show the power and phase vs. time characteristics of the black soliton like train, respectively.

nearly to zero, this is indicative of a black soliton pulse. Unlike the bright soliton case, the modulation depth here is nearly unity. The half power width of the pulses in (b) was approximately 30 ns. Notice further that the pulse repetition period of 250 ns is equal to the inverse of the 4 MHz frequency separation of the applied signals. The formation of these dark soliton like pulses through the model of Equation 7.2 was not observed regardless of the choice of frequency spectrum. Only bright pulses were observed: consistent with the single NLS equation model predictions. However, preliminary theoretical investigations based on a system of coupled NLS equations with power and wave number dependent damping have shown dark nonlinear pulse formation.

Figure 7.7 (c) shows a phase vs. time characteristic of the pulse train in (b). These profiles were measured at the same time as the profiles in 7.7 (a) and (b). Notice that at the position in time of the dips shown in (b), the phase characteristic in (c) shows a 180° phase jump. This jump is indicative of the black soliton like character of the pulse train.

The investigation of the spatial formation process of these dark nonlinear pulses revealed no significant spatial recurrence phenomena. Only very slight changes in the waveform could be observed over some period but nothing as dramatic as for the bright solitons above. This may be due to the large modulation depth of black solitons, which masks the recurrence effect.

A brief summary of the above investigation is given here. First, the power and phase vs. time profile and power vs. frequency spectrum of a bright soliton train were measured together for the first time. In addition, measurements of the bright soliton pulse width as a function of input signal frequency separation were made. Second, a spatial recurrence of the waveform shape for a train of bright soliton pulses was observed. This is the first

observation of such a spatial recurrence for envelope pulse trains in magnetic films. It was shown that a simple model based on the single NLS equation model, which utilized the frequency spectrum of a bright soliton train and nonlinear phase shifts, gave an excellent agreement with the recurrence phenomena. Further theoretical investigation is required. Third, the formation of dark soliton like pulse trains was observed for MSBVW excitations. This result is striking in light of the fact that such formation is forbidden by the single NLS equation model for waves with attractive nonlinearity. Preliminary investigations base on a set of coupled NLS equations with nonlinear damping show the excitation of dark soliton like pulses for MSBVW excitations. No recurrence was observed for these pulses. It is likely that the modulation depth of these dark pulses is too large to observe recurrence. Further theoretical investigation of this dark nonlinear pulse formation is necessary.

7.2 Magnetostatic Surface Spin Wave Solitons Formed due to Nonlinear Mode Beating

The formation of trains of SWE dark solitons through the induced modulational instability of two co-propagating waves has been previously observed [10]. In Reference 10, the time and frequency characteristics of black soliton trains as a function of input power level and frequency separation of the input signals were reported. However, the spatial formation process and the phase response of these trains of dark solitons have not been observed. Neither has the possibility of bright nonlinear pulse excitation been explored for MSSW excitations. This investigation has interesting ramifications from the

point of view of the fundamental physics of two coupled waves. In addition, this work relates to and illuminates the process of the self generation of dark soliton trains in frequency filtered active resonant rings [29].

The experimental procedure used here is virtually identical to that of Section 7.1. In such a case, only the differences will be illuminated when they arise. Here, the delay line was oriented in the MSSW configuration with the applied field perpendicular to the in-plane wave propagation direction at a nominal value of 1261 Oe. The power levels of the applied signals were equal.

Figure 7.8 shows four important graphs obtained at a nominal magnetic field of H = 1261 Oe. Graphs (a) and (b) show data in the frequency domain. Graphs (c) and (d) show data in the time domain. These data are key in understanding the experimental process used to generate solitons by nonlinear mode beating. A simple schematic of the experimental setup based on the IMP measurement system appears at the bottom of Figure 7.8.

Graph (a) shows a transmitted power vs. frequency characteristic of the single element transducer YIG film delay line. This characteristic was measured by the probe at a distance of 7 mm from the input transducer along the central axis of the film. For the data in (a) a low power microwave signal from source A was applied to the input of the delay line. This characteristic shows a narrow 270 MHz span of the MSSW excitations starting from approximately 5590 MHz. This span of frequencies is approximately two times wider than the frequency spectrum of the soliton trains observed in the experiments. This demonstrates that the losses are nearly constant across the width of the soliton frequency spectrum. This minimizes possible filtering effects.

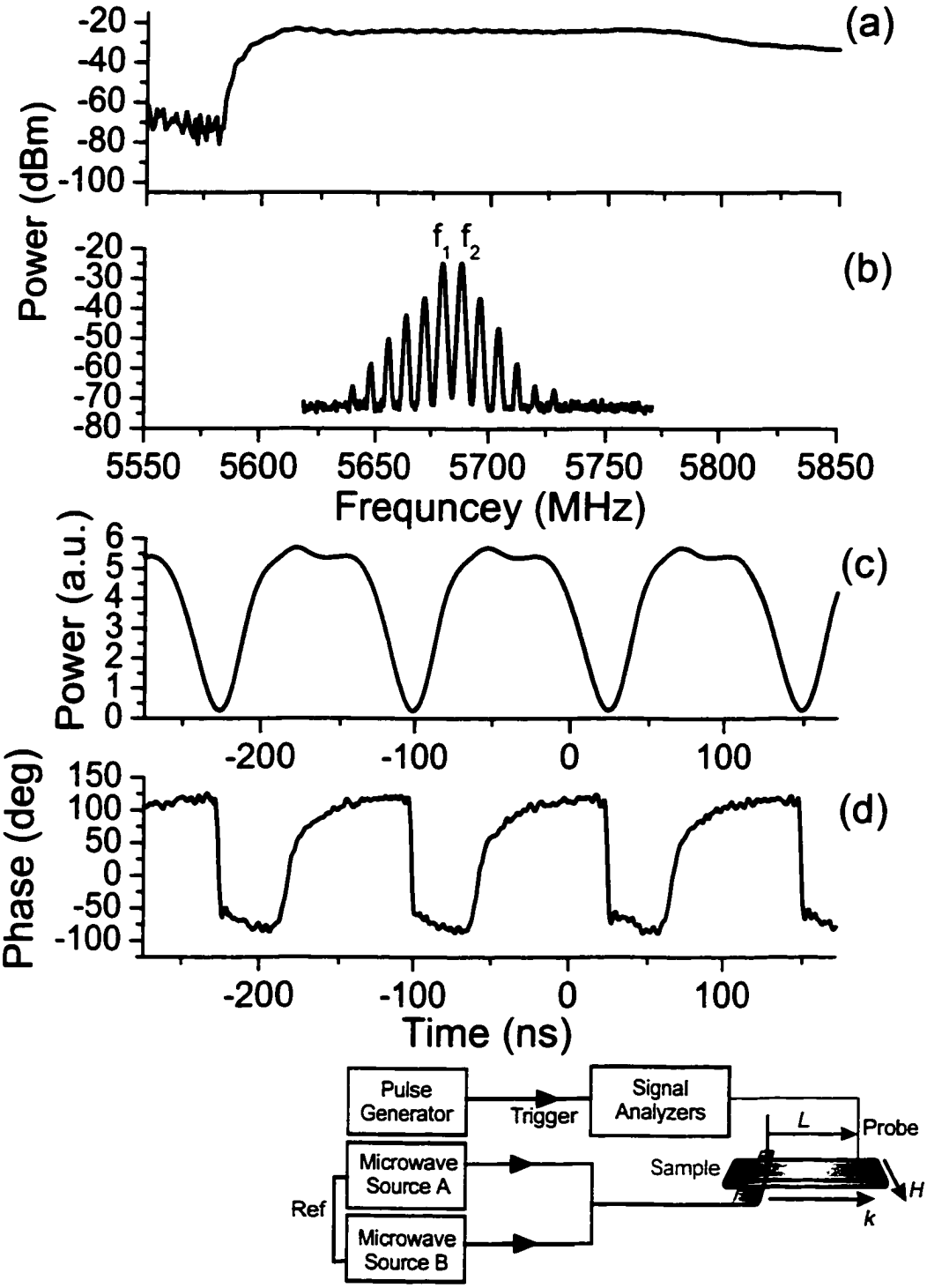

Figure 7.8. Transmitted power vs. frequency characteristic of the YIG film delay line and black soliton pulse train characteristics. Graph (a) shows the characteristic of the MSSW delay line. Graph (b) shows the power vs. frequency spectrum which results from the application of two high power microwave signals to the input of the delay line. Graphs (c) and (d) show the power and phase vs. time characteristics of the black soliton train, respectively.

Graph 7.8 (b) shows a representative power vs. frequency spectrum which results from the application of two high power microwave signals of different frequencies. The spectrum in (b) was received by the probe of the IMP system at the same position as for graph (a). For the spectrum in (b), the applied signal frequencies from sources A and B were 5688 and 5680 MHz, respectively. These signals are labeled f_1 and f_2 in (b) and each had a high input power level of 22 dBm. These power levels were in the induced modulational instability regime. The satellite harmonics formed due to the induced modulational instability are visible in (b). The 8 MHz frequency separation between the applied signals and the adjacent satellite harmonics is visible in graph (b). These data are similar to those found in Reference 10.

Turn now to the characteristics in the time domain. Figure 7.8 (c) shows a representative power vs. time profile which corresponds to the frequency spectrum shown in (b). This signal was received by the probe simultaneous to the spectrum in (b). Notice that the narrow black soliton like dips of the profiles in (c) drop essentially to zero. This near unity modulation depth, combined with pulse shape, is representative of a black soliton. The half power width of the pulses in (c) was approximately 30 ns. Notice further that the pulse repetition period of 125 ns is equal to the inverse of the 8 MHz frequency separation of the applied signals. The data in (c) are similar to the data in Reference 10.

Figure 7.8 (d) shows the phase vs. time characteristic of the soliton pulse train. This characteristic was also measured by the probe simultaneous to the characteristics in (b) and (c). The vertical axis in (d) shows phase difference, relative to a reference signal at the frequency f_1, measured in degrees. The phase profile is used to help confirm the

black soliton nature of the pulses in (c). Notice that, at the position in time of the pulses in (c), the phase characteristic shows a 180° phase jump indicative of a black soliton. These phase data were not reported in Reference 10.

In order to further confirm the nonlinear nature of the pulses under investigation, the half power width of the pulses was recorded as a function of the input signal frequency separation $\Delta f = |f_1 - f_2|$ for constant input power levels of the signals. The power level of each of the applied signals was 22 dBm, as above. The position in frequency of the signal f_1 was held constant at 5688 MHz and the position of f_2 was varied. The results of these measurements are shown in Figure 7.9. The vertical axis shows the half power output pulse width in ns. The horizontal axis shows the frequency detuning of the input signals in MHz. The solid squares in the figure are the measured points. The line shows the half power pulse width in the linear regime given by $\Delta t = 1/(2\Delta f)$.

In the region of frequency detuning between 1 MHz and 25 MHz the induced modulational instability exists and the solid squares fall below the line in the graph. Below 1 MHz, the time profiles became distorted due to losses. This is in accordance with the prediction of Equation (3.15). Equation (3.14) predicts a maximum frequency on the order of tens of MHz for self modulational instability. The larger instability region, observed here up to 25 MHz, is in accordance with the predictions that the coupled wave modulational instability is richer than that of a single wave [21]. In fact, self modulational instability is not even predicted for a *single* wave with repulsive nonlinearity. In this region, black soliton like profiles were observed. This frequency detuning width is on the same order as that observed for bright solitons in Section 7.1. The deviation of the data points from the line indicates that the soliton pulse width is

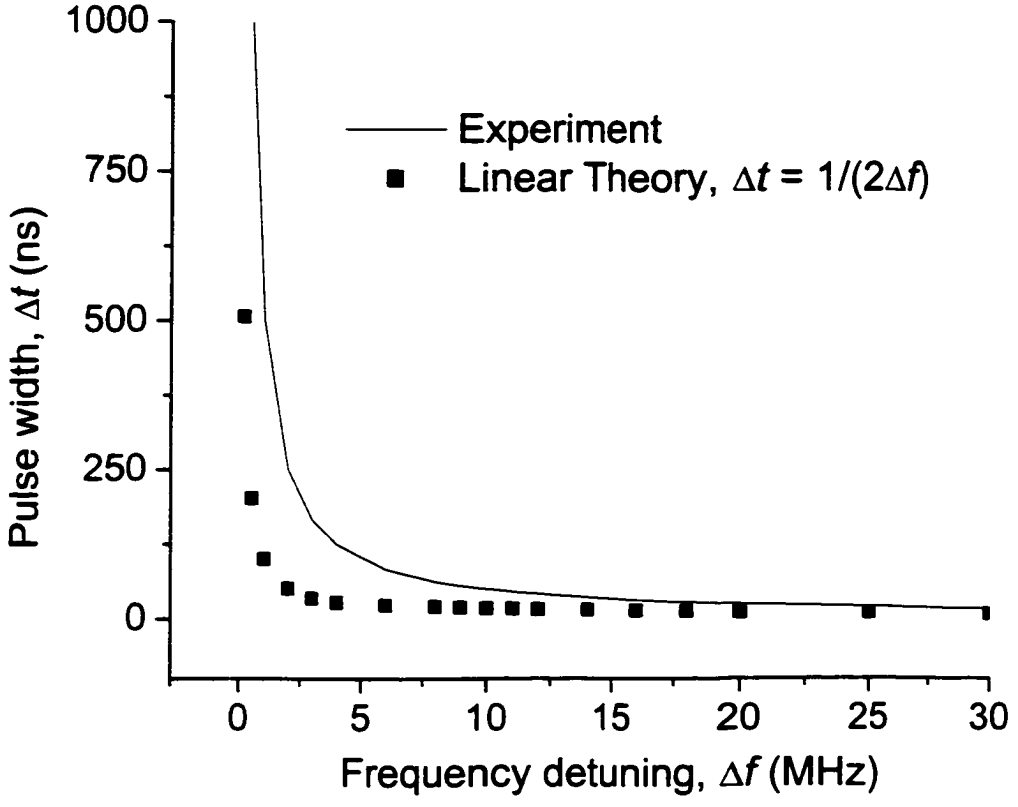

Figure 7.9. The bright soliton half power pulse width vs. frequency separation of the input signals. The solid squares show the results of the measurements. The solid line shows the linear relation $\Delta t = 1/(2\Delta f)$. The region where the measured points deviate from the linear relation coincides with the region of induced modulational instability.

narrower than the linear pulse width in this region. For larger values of frequency detuning, the solid squares lie on the line. Note that for detunings in this range, the filtering introduced by the delay line pass band is more significant. This is an indication that, even at high power, the induced modulational instability does not lead to a narrower pulse width for frequency detunings above approximately 25 MHz. For frequency detunings above 25 MHz, linear power vs. time profiles were observed. It should be noted that the 14.6 MHz frequency detuning used in Section 6.2 also lies in this instability region.

With the exception of the phase data shown in Figure 7.8 (d), the results in Figures 7.8 and 7.9 are qualitatively similar to the data presented in Reference 10. These data were used to establish the black soliton nature of the pulses and the region of instability for the parameters of the experiment. With this established, the formation processes of these black solitons were investigated. For this investigation of these nonlinear pulses the frequency separation was chosen as 8 MHz and the input power levels were 22 dBm. This value of detuning lies within the range of induced modulational instability shown in Figure 7.8.

The observation of black soliton pulse trains as a function of distance revealed no spatial recurrence. Only small periodic fluctuations in the waveform and an attenuation due to damping were observed. As was suggested in section 7.1, the absence of an observed spatial recurrence is probably due to the large modulation depth of the black solitons. However, in this *single* black soliton train regime, a measurement of the black soliton pulse width as a function of power was possible. For a variety of distances between 2 and 9 mm from the input transducer, the power level of the black soliton and

the corresponding pulse width were measured through the use of the IMP system. These measurements had not previously been made, due in part to the fact that single black soliton pulses cannot be excited with conventional microwave input pulses [8].

Figure 7.10 shows the black soliton half power pulse width as a function of power. The lower horizontal axis shows power in mW. The upper horizontal axis shows $|u|^2$ as obtained from Equation (3.13). The vertical axis shows the half power pulse widths in ns. The solid squares show the measured points while the solid line shows the values predicted from Equation (3.13). For the solid line, Equation (3.13) was used to find the theoretical half power width of the black soliton. The parameters used in Equation (3.13) were calculated from Equations (3.16), (3.18), and (3.21) and were $v_g = 5.49\times10^6$ cm/s, $D = -8430\,\mathrm{cm^2/rad\cdot s}$, and $N = -1.1\times10^{10}$ rad/s. In addition, $u_{max} = 0.035$ was used as a fitting parameter. Figure 7.8 shows that the single NLS equation model agrees well with the data.

Consider now the excitation of *bright* nonlinear pulse trains for MSSW excitations with *repulsive* nonlinearity. As explained in Chapter 3, such formation is forbidden by the single NLS equation. Figure 7.11 shows representative time and frequency domain characteristics of a bright nonlinear pulse train formed from MSSW excitations. The format of the bright pulse graphs in 7.11 (a), (b), and (c) are the same as the format of dark soliton graphs 7.8 (b), (c), and (d).

The graph 7.11 (a) shows the frequency spectrum of the bright soliton train measured at a distance of 7 mm from the input transducer of the delay line along the central axis of the film. This spectrum is the result of two high power microwave signals applied to the input of the delay line. In this case the applied signal frequencies from

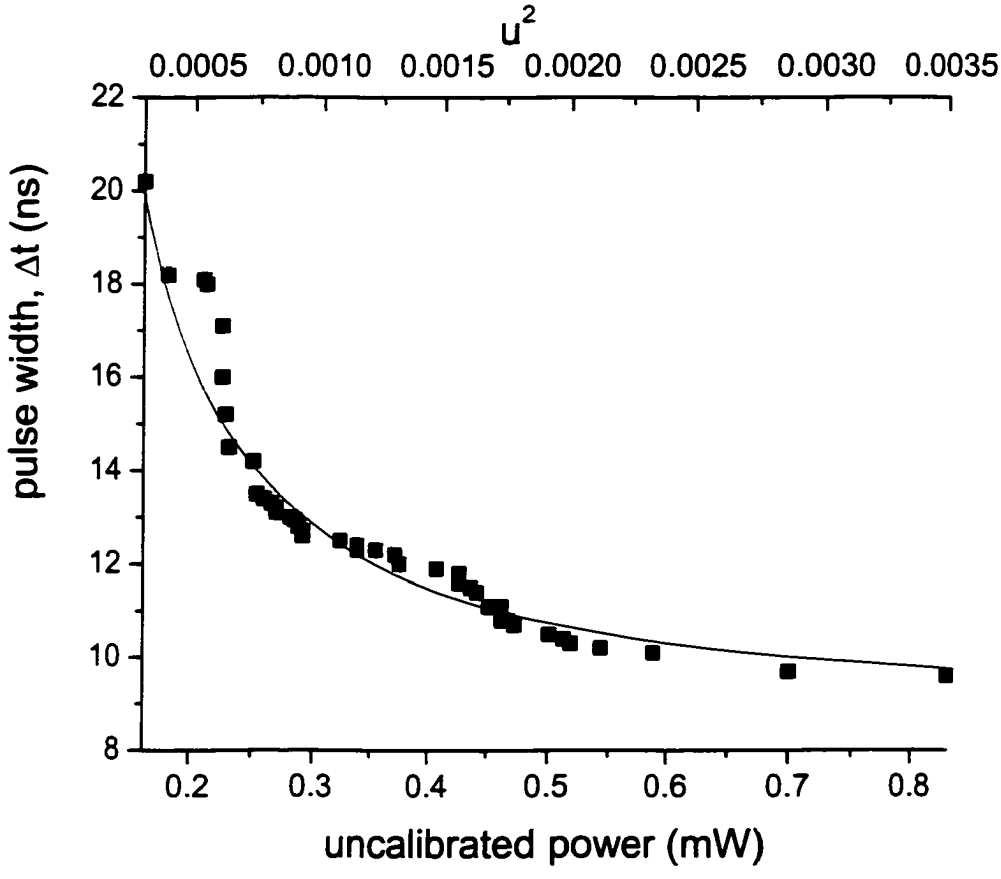

Figure 7.10. Black soliton half power pulse width vs. power. The solid squares show the result of the measurements and correspond to the lower horizontal axis which shows power in mW. The solid line shows the results of calculation using Equation (3.12) with parameters calculated from Equations (3.16), (3.18), and (3.21). The solid line corresponds to the upper horizontal axis.

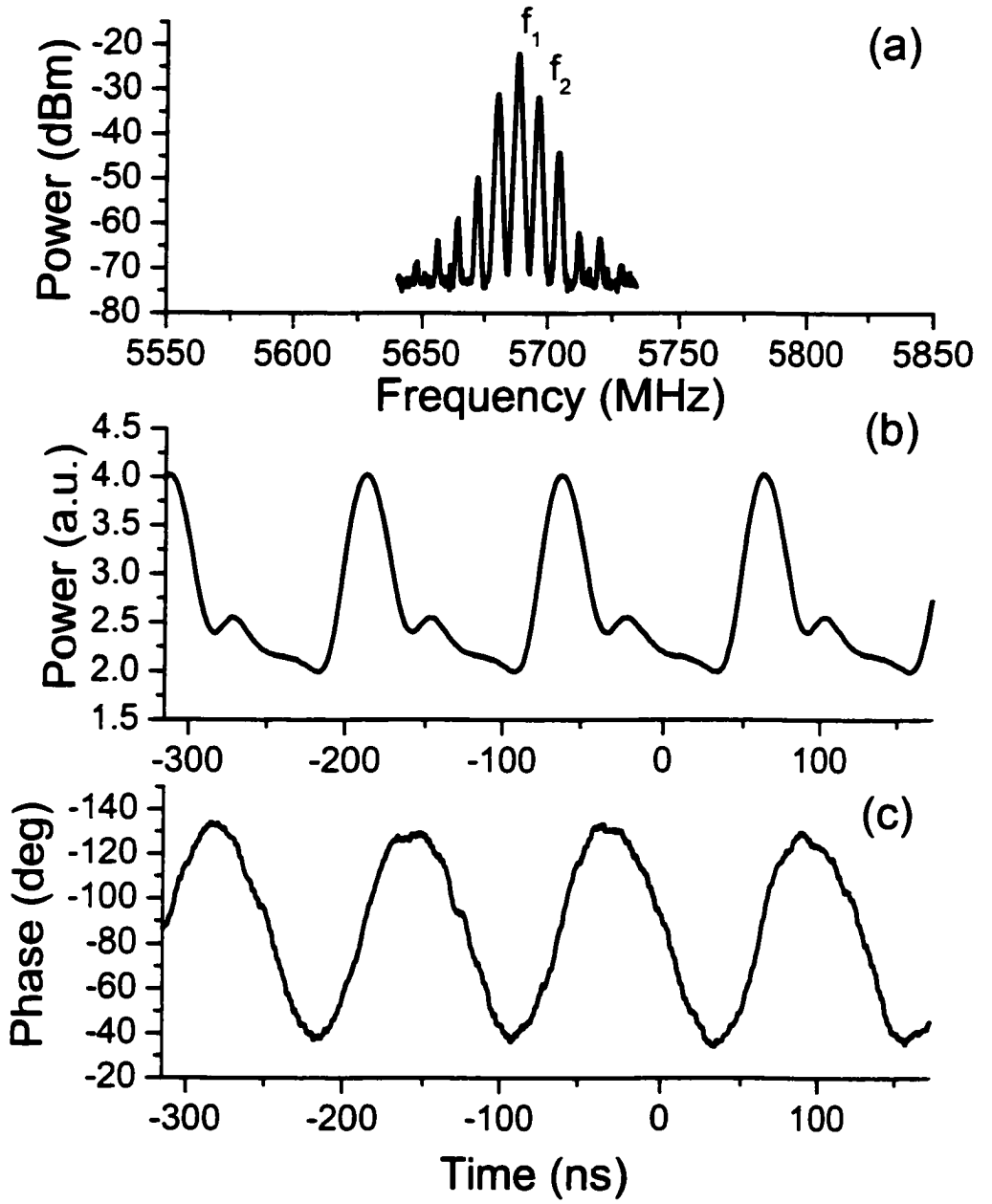

Figure 7.11. Bright soliton like pulse train characteristics for MSSW excitations. Graph (a) shows the power vs. frequency spectrum which results from the application of two high power microwave signals to the input of the delay line. Graphs (c) and (d) show the power and phase vs. time characteristics of the bright soliton like train, respectively.

sources A and B were 5688 and 5680 MHz. These signals are labeled f_1 and f_2 in the figure and had input power levels of 16 and 25 dBm, respectively: well into the induced modulational instability regime. It is of interest to note that the total power here is *smaller* than in the dark soliton case observed above. The satellite harmonics are visible in the figure. The separation between the applied signals and adjacent satellite harmonics was 8 MHz as shown in (a).

Consider now the time domain characteristics. Figure 7.11 (b) shows a representative power vs. time profile which corresponds to the frequency spectrum shown in (a). This signal was received by the probe simultaneous to the spectrum in (a). Notice the narrow bright soliton like shape of the profiles in (b). Note further the relatively small modulation depth. The half power width of the pulses in (b) was approximately 25 ns. Notice further that the pulse repetition period of 125 ns is equal to the inverse of the 8 MHz frequency separation of the applied signals. The formation of these bright nonlinear pulses through the model of Equation 7.2, based on the single NLS equation model, was not observed.

Figure 7.11 (c) shows the phase vs. time characteristic of the pulse train in (b). This profile was measured at the same time as the profiles in (a) and (b). Notice that, at the position in time of the dips shown in (b), the phase characteristic in (c) shows no plateau which is indicative of a bright soliton. This is further indication that the single NLS equation model is insufficient to describe the formation of bright MSSW solitons. Theoretical investigation of the results shown in (b) and (c) based on a system of coupled NLS equations is necessary.

The investigation of the spatial formation process of these bright MSSW nonlinear

pulses revealed no spatial recurrence phenomenon. Though the pulse waveform was changed somewhat as function of distance, no stable repetition was observed.

A brief summary of the above investigation is given here. First, the power and phase vs. time profile and power vs. frequency spectrum of a black soliton train were measured together for the first time. In addition, measurements of the black soliton pulse width as a function of input signal frequency separation were made. Second, no spatial recurrence was observed for these pulses. It is likely that the modulation depth of these dark pulses is too large to observe the small effects responsible for recurrence. Third, the *single* black solitons half power pulse width vs. power was measured and modeled with the single NLS equation model. Fourth, the formation of bright soliton like pulse trains was observed for MSSW excitations. This result is striking in light of the fact that such formation is forbidden by the single NLS equation model for waves with repulsive nonlinearity. No recurrence was observed for these pulses. Further theoretical investigation of this bright MSSW nonlinear pulse formation is necessary.

CHAPTER 8

CONCLUSION

8.1 Summary of Results

An investigation of nonlinear MSW excitations has been performed. In particular, spin wave envelope (SWE) solitons and the induced modulational instability of magnetostatic spin wave (MSW) excitations in ferrite films have been investigated. Two sets of experiments on these topics were performed. First, the self generation of SWE bright and dark solitons due to the induced modulational instability of self generated modes in specially designed frequency filtered ARR structures was realized. Second, an investigation of similar SWE bright and dark solitons, formed due to the induced modulational instability of co-propagating MSW excitations, was performed.

A new technique based on a frequency filtered ARR was utilized in the self generation experiments. This technique has advantages over previous SWE soliton self generation experiments which utilized a technique know as synchronized time gating. The frequency filtered ARR was able to self generate time stable SWE solitons without the use of any of the modulation elements required by the synchronized time gating technique. This filtering technique represents a completely new approach to soliton production and is applicable to any nonlinear dispersive waveguiding media.

The self generation of *single* black and gray SWE solitons was realized for the first time [29]. Due to phase constraints introduced by switching elements [see, e.g., 4 – 7, 20], the excitation of SWE black solitons was, prior to these experiments, not observed [8]. The self generation of narrow bright microwave pulses may be useful as a replacement for existing microwave pulse generators [28].

The investigation of SWE bright and dark solitons formed due to the nonlinear mode beating of MSW excitations was performed. The phase and power vs. time, as well as the power vs. frequency spectra, were observed together for these pulses for the first time. In addition, the pulse width as a function of input signal frequency separation was measured.

For nonlinear MSBVW excitations, a spatial recurrence of the waveform shape for a train of bright soliton pulses was observed [30]. This is the first observation of such a spatial recurrence for envelope pulse trains in magnetic media. A simple model based on the single NLS equation model gave exceptional agreement with the recurrence phenomenon data. In addition, the formation of *dark* nonlinear pulse trains was observed for MSBVW excitations with *attractive* nonlinearity. Such formation is forbidden by the single NLS equation model. Preliminary modeling based on a set of coupled NLS equations, with *nonlinear* damping [31], show the formation of dark nonlinear pulses. Despite the spatial recurrence observed for bright MSBVW pulse trains, no spatial recurrence of the waveform shape for a train of dark soliton like pulses was observed. This may be due to the relatively large modulation depth of black pulses.

For nonlinear MSSW excitations, a spatial recurrence of the waveform shape for a train of black soliton pulses was *not* observed. As for the above black pulses, this is most

likely due to the large modulation depth which may mask the recurrence phenomenon. The black MSSW soliton pulse width as a function of power was observed for the first time. The results agreed well with the prediction of the single NLS equation model. In addition, *bright* nonlinear pulse train formation was observed for MSSW excitations with *repulsive* nonlinearity. Such formation is also forbidden by the single NLS equation model. Despite the spatial recurrence observed for bright MSBVW pulse trains, no spatial recurrence of the waveform shape for a train of bright MSSW soliton like pulses was observed.

8.2 Future Work

The future work related to this thesis can be considered in two categories. The first category is future work which is a consequence of the experiments reported on in this thesis. The second category is future work related to the inductive magnetodynamic probe (IMP) system.

The future work related to the self generation of SWE solitons [28, 29] will be given here. As mentioned in the in Chapter 6, the microwave signal behavior in an active resonant ring at very high gains was chaotic. An investigation of the behavior of these frequency filtered ARR structures at very high gains is necessary. The modeling of the self generation of SWE solitons in ARR structures remains unrealized. Furthermore, through the use of different transducer designs, the self generation of a wide variety of pulse trains is possible. The self generation of a train of double pulses may be of particular interest. Moreover, the self generation of nonlinear pulse trains in wide films,

as well as thicker films, may be of interest.

The future work related to the results in Chapter 7 will be given here. The investigation related to the excitation SWE bright and dark nonlinear pulses in regimes forbidden by the single NLS model requires further theoretical as well as experimental investigation. In addition, collision experiments with soliton trains, particularly with single black soliton trains, may be of interest. The formation of nonlinear pulse trains due to mode beating in thicker or wider ferrite films may also be of interest.

The future work related to the IMP system will be given here. The IMP system, developed in this thesis, provides the ability to perform both time and space resolved measurements on MSW excitations in ferrite films. A wide variety of such measurements would be of interest. One such measurement is related to single soliton pulse collisions. Measurement of the collision of SWE bright and dark solitons with the phase information, accessible to the time and space resolved IMP system, has yet to be done. Furthermore the IMP system should be improved to allow for the investigation of magnetostatic forward volume spin waves. In general, the high resolution capabilities of the IMP system provide the possibility for a nearly endless and illuminating investigation of the linear and nonlinear properties of MSW, as well as other, excitations.

REFERENCES

[1] W. S. Ishak, *Proc. IEEE* **76**, 171 (1988)

[2] M. Remoissenet, *Waves Called Solitons: Concepts and Experiments* (Springer-Verlag, Berlin, 1996).

[3] *Optical Solitons - Theory and Experiment*, Edited by J. R. Taylor (Cambridge University Press, Cambridge, 1992).

[4] C. E. Patton, P. Kabos, H. Xia, P. A. Kolodin, R. Staudinger, B. A. Kalinikos, and N. G. Kovshikov, J. Magn. Soc. Japan **23**, 605 (1999).

[5] B. A. Kalinikos, N. G. Kovshikov, and A. N. Slavin, Zh. Eksp. Teor. Fiz. **94**, 159 (1988) [Sov. Phys. JETP **67**, 303 (1988)].

[6] B. A. Kalinikos, N.G. Kovshikov, and C. E. Patton, Phys. Rev. Lett. **80**, 4301 (1998).

[7] B. A. Kalinikos, N.G. Kovshikov, and C. E. Patton, Pis'ma Zh. Eksp. Teor. Fiz. **68**, 229 (1998) [JETP Lett. **68**, 243 (1998)].

[8] A. N. Slavin, Y. S. Kivshar, E. A. Ostrovskaya, and H. Benner, Phys. Rev. Lett. **82**, 2583 (1999).

[9] V. E. Demidov, Pis'ma Zh. Eksp. Teor. Fiz. **68**, 828 (1998) [JETP Lett. **68**, 869 (1998)].

[10] H. Benner, B. A. Kalinikos, N. G. Kovshikov, and M. P. Kostylev, Pis'ma Zh. Eksp.

Teor. Fiz. **72**, 306 (2000) [JETP Lett. **72**, 213 (2000)].

[11] D. Stancil, *Theory of Magnetostatic Waves* (Springer-Verlag, New York, 1993).

[12] C. E. Patton, Phys. Rep. **103**, 253 (1984).

[13] A. G. Gurevich and G. A. Melkov, *Magnetization Oscillations and Waves* (CRC Press, New York, 1996).

[14] R. W. Damon and J. R. Eshbach, J. Phys. Chem. Solids **19**, 308 (1961).

[15] M. J. Hurben and C. E. Patton, J. Magn. Magn. Mat. **139**, 263 (1995).

[16] V. S. L'vov, *Wave Turbulence Under Parametric Excitation: Applications to Magnets*, (Springer-Verlag, Berlin, 1994).

[17] V.E. Zakharov and A. B. Shabat, Zh. Eksp. Teor. Fiz. **61**, 118 (1972) [Sov. Phys. JETP **34**, 62 (1972)].

[18] J. M. Nash, P. Kabos, R. Staudinger, and C. E. Patton, J. Appl. Phys. **83**, 2689 (1998).

[19] V.E. Zakharov and A. B. Shabat, Zh. Eksp. Teor. Fiz. **64**, 1627 (1973) [Sov. Phys. JETP **37**, 823 (1973)].

[20] M. M. Scott, Y. K. Fetisov, V. T Synogach, and C. E. Patton, J. Appl. Phys. **88**, 4232 (2000).

[21] C. J. Mckinstrie, and G. G. Luther, Phys. Scr. **30**, 31 (1990).

[22] A. K. Zvezdin, and A. F. Popkov, Sov. Phys. JETP **57**, 350 (1983) [Zh. Eksp. Teor. Fiz. **84**, 606 (1983)].

[23] J. D. Adam, M. R. Daniel, P. R. Emtage, and S. H. Talisa, in *Thin Films for Advanced Electronic Devices*, edited by M. H. Francombe and J. L. Vassen (Academic, Boston, 1991), Vol. 15, p. 1.

[24] D. M. Pozar, *Microwave Engineering*, (Addison-Wesley Publishing Company, New York, 1990).

[25] N. P. Vlannes, J. Appl. Phys. **61**, 416 (1987).

[26] J. J. Lynch and R. A. York, *IEEE Microwave and Guided Wave Lett.* **5**, 213 (1995).

[27] P. J. Rezin, Microwaves and RF Journal, **39**, 63 (2000).

[28] M. M. Scott, B. A. Kalinikos, and C. E. Patton, Appl. Phys. Lett. **78**, 970 (2001).

[29] B. A. Kalinikos, M. M. Scott, and C. E. Patton, Phys. Rev. Lett. **84**, 4697 (2000).

[30] M. M. Scott, B. A. Kalinikos, and C. E. Patton, unpublished results

[31] M. M. Scott, B. A. Kalinikos, and C. E. Patton, unpublished results